Dissertation

submitted to the

Combined Faculty of Mathematics, Engineering and Natural

Sciences

of Heidelberg University, Germany

for the degree of Doctor of Natural Sciences

Put forward by

Christian Warnecke born in: Rendsburg

Oral examination: 2025/04/24

A cryogenic microscope for state detection of Be^+ ions confined in an ultralow-noise environment

Referees: apl. Prof. Dr. José Ramón Crespo López-Urrutia

Dr. Wolfgang Quint

ABSTRACT Optical frequency standards are some of the best characterized systems in physics these days. While optical transitions highly charged ions are excellent candidates for pushing the limits of laser spectroscopy at highest precision further, they require sophisticated quantum logic schemes to be cooled and interrogated. A novel superconducting quadrupole resonator is characterized to confine both, HCI and logic beryllium ion in an environment free of external electromagnetic noise. By utilizing atomic transitions sensitive to magnetic field fluctuations, the Meissner state of the resonator was investigated.

Furthermore a cryogenic microscope lens with a numerical aperture of 0.4 was developed for improved state-readout of the Be^+ logic ions at a transition wavelength of 313 nm.

ZUSAMMENFASSUNG Optische Frequenzstandards gehören heutzutage zu den am besten charakterisierten Systemen in der Physik. Während optische Übergänge in hochgeladenen Ionen ausgezeichnete Kandidaten sind, um die Grenzen der Laserspektroskopie mit höchster Präzision weiter zu verschieben, erfordern sie ausgeklügelte Quantenschemata, um gekühlt und untersucht zu werden. Ein neuartiger supraleitender Quadrupolresonator wurde charakterisiert, um sowohl HCI als auch logische Beryllium-Ionen in einer Umgebung frei von externem elektromagnetischem Rauschen einzuschließen. Durch die Nutzung von atomaren Übergängen, die empfindlich auf magnetische Feldschwankungen reagieren, wurde der Meissner-Zustand des Resonators untersucht.

Zudem wurde eine kryogene Mikroskoplinse mit einer numerischen Apertur von 0,4 entwickelt, um das Auslesen des Zustands der Be^+-Logik-Ionen bei einer Übergangswellenlänge von 313 nm zu verbessern.

CONTENTS

ACRONYMS

BSM beyond the standard model

CaF2 calcium fluoride

CCD charged coupled device

CMOS complementary metal-oxide-semiconductor

CryPTEx cryogenic paul trap experiment

EBIS electron beam ion source

EBIT electron beam ion trap

EDM Electrical discharge machining

EMCCD electron multiplying charged coupled device

HCI highly-charged ion

MPIK Max-Planck-Institut für Kernphysik Heidelberg

MTF modulation transfer function

OTF optical transfer function

PMT photo multiplier tube

PSF point spread function

PTB Physikalisch Technische Bundesanstalt Braunschweig

QED quantum electrodynamics

RF radio frequency

RFQ radio-frequency quadrupole

SM standard model of particle physics

UVFS UV fused silica

1 INTRODUCTION

> Reality is what kicks back when you kick it.
>
> Victor J. Stenger

The term "Optics", derived from the ancient Greek word ὀπτικός (optikós), meaning 'pertaining to seeing, concerning vision,' is deeply rooted in the exploration of vision-related phenomena. This discipline, known as ὀπτική [τέχνη] (optikḗ [téchnē]), represents the 'science of vision.'

Your ability to read this text indicates the optimal functioning of your optical system. The electromagnetic waves, whether reflected from a piece of paper or emitted by the screen in front of you, undergo meticulous modulation through two lenses and an iris, ultimately projecting onto the retina.

Over the past centuries, extensions have been developed to increase the observed details and constrast. In addition electrical detectors were developed to quantify the incoming photons on a focusing plane. The principle of visual detection stands as one of the most crucial tools in contemporary science and various industries. From observing celestial bodies in space to examining cells on a microscope slide, detecting obstacles in front of a moving vehicle, etching structures on silicon wavers with nanometer precision or identifying defects in manufactured products, these processes rely on the availability of a sophisticated optical system capable of manipulating photons effectively.

1.1 OPTICS

The first optical elements, such as plano-convex and concave lenses made of quartz, as well as compound mirrors, date back to antiquity when the laws of reflection were already well known [1,2]. Working early primitive microscopes and telescopes, however, could only be described appropriately with small angle relations for a long time and consisted of a single collection lens and a second concave projection element, following the early description of refraction by Ibn Sahl in the 10th century [3]. Notably,

in 1609, Galileo improved the telescope design of Hans Lipperhey by reducing the aperture to just 15 mm, decreasing the aberrations of this device [4],. During this period, microscopes with simple focusing mechanisms and magnifications of about 100x also evolved [1]. A formal description of refraction behavior in different media was experimentally rediscovered in 1621 by Willebrord Snell. Meanwhile, Pierre de Fermat introduced the principles of least time in 1662, leading to the following relation :

$$\frac{\sin\theta_1}{\sin\theta_2} = \frac{n_1}{n_2} \tag{1}$$

where θ_1 is the angle of incidence of light on a surface, θ_2 is the angle of refraction, and n_1 and n_2 are the indices of refraction for the respective media. This foundational work paved the way for the construction of lens systems comprising both low and high dispersion materials that focus light independently of color. Christian Huygen's published work on a wave theory of light in 1690 gave the first mathematical description of phenomena which were could not be explained by the at that time widely accepted ray theory. His work was later expanded by Fresnel around 1800 and today the generalized Huygens-Fresnel principle is of the form

$$\Psi'(x',t') = i\int d^3x\, G(x',t';x,t)\,\Psi(x,t) \tag{2}$$

and renders the propagation of light, including diffraction and interference. More importantly it is compatible with modern concepts, such as quantum field theory. Here, the wave function Ψ is modified by the Green's function G, acting in an optical system as the impulse response or pupil function for the wave.

Alongside the study of light propagation, investigations into electricity and magnetism were undertaken, culminating in the formulation of Maxwell's equations around the 1860s. In their modern form, these equations are expressed as follows [5]:

$$\begin{aligned} \nabla\times\boldsymbol{E} + \frac{\partial\boldsymbol{B}}{\partial t} &= 0 & \nabla\cdot\boldsymbol{D} &= \rho \\ \nabla\times\boldsymbol{H} + \frac{\partial\boldsymbol{D}}{\partial t} &= \boldsymbol{j} & \nabla\cdot\boldsymbol{B} &= 0 \end{aligned} \tag{3}$$

These equations describe the interrelationship between the electric field $\boldsymbol{E}$ and a magnetic induction $\boldsymbol{B}$ by electric displacement $\boldsymbol{D}$, a magnetic vector $\boldsymbol{H}$ and charge densities ρ and $\boldsymbol{j}$.

Depending on the application, modern optical systems are evaluated using all three frameworks: starting with simple geometric thought experiments to minimize induced aberration errors, evolving into the influence of apertures by propagating waves through the system, and considering the impact of coatings or surface textures by numerical simulations involving Maxwell's equations. Within the scope of

this thesis, in particular the first two disciplines are used to refine and develop a microscope system, which collects light, emitted by beryllium ions at an ultraviolet wavelength of 313 nm in a cryogenic experiment. This experiment will be used to probe for fundamental properties of physics as shown in the next section.

1.2 FREQUENCY STANDARDS BASED ON HIGHLY CHARGED IONS

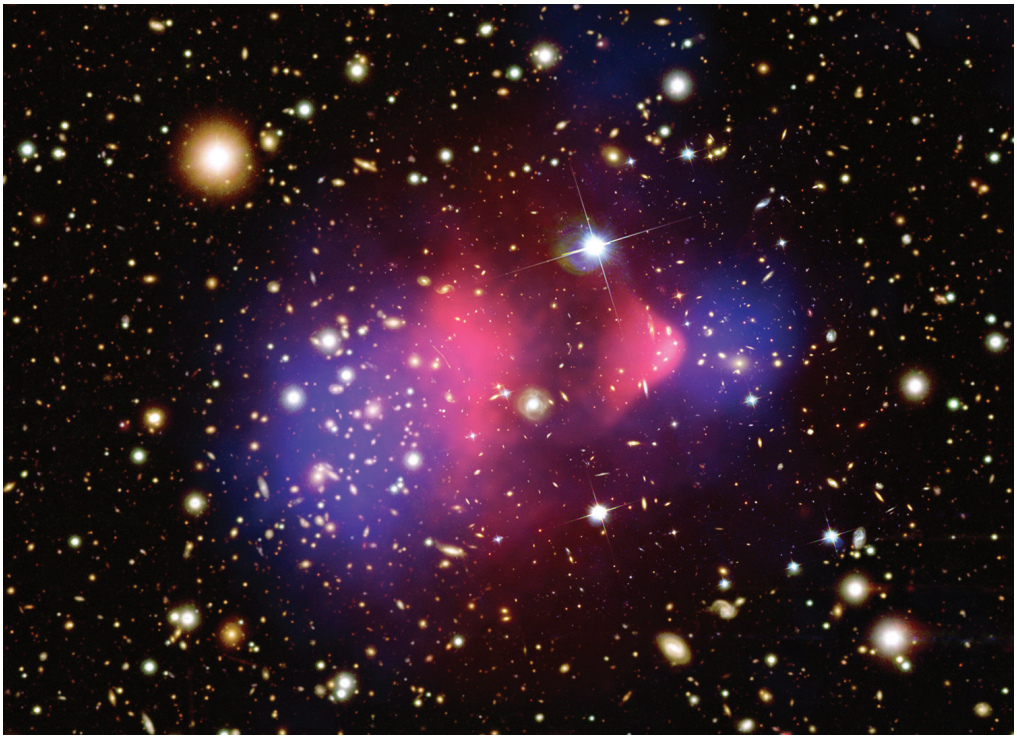

Figure 1: Composite image of the Bullet Cluster 1E 0657-56. The optical data was taken by the Magellan telescope and overlaid by the total mass, calculated through weak gravitational lensing projections [6]. In pink, X-ray emissions observed by Chandra are drawn. Credit: X-ray: NASA/CXC/CfA/M.Markevitch et al.; Optical: NASA/STScI; Magellan/U.Arizona/D.Clowe et al.; Lensing Map: NASA/STScI; ESO WFI; Magellan/U.Arizona/D.Clowe et al.

One of the most benchmarked observations today involves two merging galaxies known as the Bullet Cluster (1E 0657-56), which serves as a unique playground for physics. The object exhibits emission features from hot baryonic matter both in front and behind shock waves, weak and strong gravitational lensing effects, and the dynamics of matter in a comparably dense space [7–9]. By estimating the mass required to account for such characteristics, it becomes clear that the observable baryonic matter, combined with standard gravitational models, is insufficient. This discrepancy

has led to the exploration of various hypotheses, including modified laws of gravity [10] or additional particles that primarily interact with baryonic matter through gravity [11]. These hypothetical dark matter particles are not described by the well-established standard model of particles SM, which consists of quarks, leptons and bosons interacting with each other in three ways; weak, strong and electromagnetic.

1.2.1 Searches for new physics

For a long time, probing the fundamental nature of the universe was limited to experiments involving high energies, like accelerators, or astrophysical observations such as the cosmic microwave background. Just over the last decades, precision experiments in atomic physics have emerged as a powerful tool for exploring the underlying principles of matter and forces [12–15]. To date, some of the best-characterized physical properties are optical transitions in atoms, driven by extremely stable lasers, achieving fractional uncertainties as low as 8×10^{-19} [16].

TIME VARIATION OF FUNDAMENTAL CONSTANTS At such high precision, theories exploring extension fields of the standard model predict phenomena such as oscillations or drifts in transition energies that cannot be explained by the SM [13,17]. The transition frequency ν for electronic transitions can be broadly expressed as [18]:

$$\nu \propto c\, R_\infty\, A(Z)\, F(\alpha) \tag{4}$$

where c is the speed of light, R_∞ the Rydberg constant, $A(Z)$ a factor dependent on the nuclear charge Z, and $F(\alpha)$ depends on the dimensionless, fine-structure constant $\alpha = e^2/\hbar c$, which governs the interaction strength between electrons and photons within the standard model [19]. One direct implication of this relationship is the necessity of an extremely stable reference that is insensitive to α - or a probe that scales differently with the fine structure constant. This stability is typically achieved by comparing the transition to another transition in the same or a different atomic system [20]. The ratio of two reference standards ν_1, ν_2 with a combined sensitivity coefficient $k_\alpha = k_2 - k_1$ is directly linked to [21]:

$$\frac{\Delta(\nu_1/\nu_2)}{\nu_1/\nu_2} = -k_\alpha \frac{\Delta\alpha}{\alpha} \tag{5}$$

Depending on the theoretical framework, variations of α exhibit certain properties. One widely studied extension of the standard model involves coupling to a scalar dark matter field, which induces oscillations in the fine-structure constant [11,22]:

$$\begin{aligned} \alpha(t) &\approx \alpha\,(1 + d_e \phi_0 \cos(\omega t + \delta)) \\ \phi_0 &\propto \frac{\sqrt{2\,\rho_{\mathrm{dm}}}}{m_\phi} \end{aligned} \tag{6}$$

where ρ_{dm} and m_ϕ represent the dark matter energy density and mass, respectively, and $d_e \propto \omega/k_\alpha$ is the coupling parameter.

Precision clock transition measurements enable exclusion of certain dark matter candidates and comparison to previous observations from equivalence principle tests [23] or clock networks [24]. Atomic systems with optical transition pairs that are robust against external noise and possess exceptionally long lifetimes are particularly promising for these studies. Such systems enable low instabilities $\sigma_S \propto \zeta/\sqrt{N\tau}$ and high accuracies $\Delta\nu/\nu$, where ζ is a scaling factor related to clock transition properties such as the transition frequency ν_0, linewidth $\delta\nu_0$ and measurement methods, and τ is the integrated interrogation time multiplied by N, the number of atoms observed.

These characteristics are essential for detecting weak couplings at higher oscillation frequencies. Additionally, transitions with high sensitivity coefficients k_α of opposite signs are required to increase the likelihood of finding evidence on new physics. These requirements are well met by transitions in multiply ionized matter, known

Bohr radius	Z^{-1}
Polarizability	Z^{-4}
Electronic gross structure	Z^{2}
Fine structure	Z^{4}
Hyperfine splitting	Z^{3}
QED effects	Z^{4}
2nd order Stark effects	Z^{-4}

Table 1: Scaling laws for atomic properties of hydrogen-like ions [19].

as highly charged ions (HCI) [19]. Table 1 summarizes the scaling laws for the isoelectronic sequence of hydrogen and shall serve as an orientation for these systems. While the Bohr radius of the electron is shrinking due to the increased nuclear charge, the electron density function overlaps more and more with the core, such

that it dominates the influence on a driven transition. Thus energy shifts due to electric or magnetic fields are suppressed, scaling with high exponents, Z^{-3} to Z^{-4}. Detailed discussions for non-hydrogen-like systems are presented in [19,25,26]. Due to the long lived hyperfine transitions of high-Z hydrogen-like HCI, while by acknowledging the implied challenges in their preparation and recombination likelihood, they were first considered as potential candidates for quantum computing applications by coherent state manipulation. The well separated energy levels allow for long coherence times due to suppressed off-resonant spontaneous scattering [27,28]. Since hyperfine transition frequencies are proportional to

$$\eta_{\mathrm{hfs}} \propto c\, R_\infty\, A(Z)\, \frac{g_i}{\mu} \alpha^2 F(\alpha) \tag{7}$$

where $g_i = \mu_i/\mu_\mathrm{N}$ is the gyromagnetic ratio, μ_N the nuclear magneton, μ_i the nuclear magnetic moment and $\mu = m_\mathrm{p}/\mu_\mathrm{e}$ is the proton-to-electron mass ratio [18], which is considered as a probe of strong and weak interaction coupling and thus can be utilized as further test of new physics [17], HCI were initially proposed to push the upper limit of a variation obtained by cesium microwave transitions further to higher accuracies [29]. To overcome the requirement for high energies driving the electronic transitions in highly charged ions, the field of research got more and more focused on intermediate ionization levels involving a change in the electron orbital order system from Madelung- to Coulomb ordering, inducing a level crossing [26, 30–32]. In recent years, one species has gained significant attention for measuring variations in the fine structure constant: the proposed clock transitions in Cf^{15+} and Cf^{17+}, which obtain opposite sign sensitivities $|\Delta k_\alpha| \approx 100$, significantly higher than those of singly charged ions, which typically range within $k_i \approx \pm(1-2)$ [33,34]. Furthermore, developments in new light sources enable research on metastable transitions in the extreme ultraviolet regime and access to frequency standards at even lower uncertainties [19,35–37].

ISOTOPE SHIFTS AND SEARCHES FOR FIFTH FORCES Another approach to probing beyond-standard model physics is the analysis of isotope shifts in atomic systems, which can test hypothetical fifth-force couplings to the nucleus [38]. Transition lines within a single isotope form a vector space that can be analyzed to identify nonlinear contributions in isotope shifts [39]. Recent work has constrained the parameter space for light boson couplings by combining transitions in highly charged and singly ionized calcium isotopes [40]. High-precision spectroscopy of HCI extends this parameter space, leveraging their sensitivity to ionization grade. Since current evidence points to nonlinear effects induced by deformed nuclei [40, 41], systems with symmetries at magic Z numbers are now being investigated [42].

1.3 COLD HIGHLY CHARGED IONS

HCI naturally occur only in extreme environments such stellar interiors, because their existence requires ionization energies of several hundred to thousand electron volts. As a consequence, the production of HCI at highest charge states in Earth-bound experiments often employed particle accelerators [43, 44] or tokamaks [45], enabling quantum electrodynamics tests on bound state electrons in hydrogen-like ions. More compact devices, such as electron beam ion sources (EBIS) [46, 47] or traps (EBIT) [48, 49], achieve high charge states by using a compressed electron beam to ionize atoms through electron impact until the binding energy of the remaining electrons exceeds the electron beam kinetic energy. While these instruments perform exceptionally, the hot plasma produced inside an EBIT is limiting the directly achievable resolution dramatically to $\Delta\nu/\nu \approx 10^{-7}$ [50–52] due to Doppler shifts. Although successful approaches for extracting HCI have been developed over the last decades in Penning traps, which involve storing and thermalizing the ions to cryogenic temperatures for mass measurements at highest precisions [53–56] even allowing for laser spectroscopy in the order of $\Delta\nu/\nu \approx 10^{-9}$, the first Paul trap experiment which stored a HCI was reported in 2015 [57–59]. This breakthrough has laid the fundamental groundwork for high-precision spectroscopy of HCI, making it competitive with modern frequency standard experiments. In contrast to a Penning trap holding a strong magnetic field [60], confinement of charged particles in three dimension can be achieved by superimposing an oscillating quadrupole radiofrequency and a static electric field in a Paul trap [61–63]. By driving a fast, closed cycle transition of a stored ion with a laser field, it can be cooled down to a temperature that is only limited by the recoil momentum of the scattered photons [64, 65], thus first- as well as second-order Doppler shifts are highly suppressed [66]. These cold ions, trapped in a harmonic potential, can be dressed by a different light field and further cooled to the ground state of motion $|0\rangle_m$ by removing discrete quanta from the system while applying anti-Stokes Raman schemes [67, 68]. For a two ion crystal with ions marked as 1 and 2, that state $|\Psi\rangle$ can be described by

$$|\Psi\rangle = |\downarrow\rangle_1|0\rangle_m|\downarrow\rangle_2$$

By a sequence of pulses the internal state $|\downarrow\rangle_1$ is coupled to the motional state inside the shared quantum harmonic oscillator. This allows for a transfer of the first ion state to the second logic ion. Such a scheme is called quantum logic spectroscopy [69] and allows a direct readout of atomic species, such as HCI which do not feature a fast closed cycle transition to be utilized as frequency standards, by coupling them to well suited alkali-like ions. Furthermore, this scheme is independent of the spectroscopy ion and considered versatile [70]. Quantum logic spectroscopy based

measurements recently improved the hyperfine M1 transition accuracy in boron-like argon with an absolute frequency of

$$\nu(^{40}\mathrm{Ar}^{13+}) = 679\,216\,462\,397\,957.43(11)\mathrm{Hz}$$

which was a remarkable seven orders of magnitude improvement [71].

1.4 THESIS OUTLINE

To enable quantum logic spectroscopy on highly charged ions in a environment with strongly suppressed noise and probe fundamental physics in the low energy, high precision regime, recently a new type of ion trap with superconducting quadrupole resonator was commissioned [72, 73]. As so called logic ion, singly charged beryllium is utilized, allowing for co-trapping of a wide range of HCI species. After an introduction chapter on the relevant theory (Chapter 2), this experiment is reviewed (Chapter 3) and the properties of the resonator discussed (Chapter 4).

Quantum logic spectroscopy requires the discrimination of a qubit state, which, during the probe time, only scatters a few dozens photons on a detector. To maximize the number of detections, an optics system with a large collecting solid angle is required. The second part will therefore focus on methods of photon collection in this cryogenic environment. Firstly, concepts for observation of multi-ion species are presented, then the discussion is shifted onto the development of a monochromatic imaging system working at cryogenic temperatures. For this an opto-mechanical solution is presented.

2 | THEORY

2.1 LEVEL STRUCTURE OF $^9BE^+$

Beryllium ions feature a simple level scheme with two closed shell and a single valence electron. For production of singly charged beryllium, the photo-ionization energy is 9.32 eV [74], corresponding to a single photon with a wavelength of 133 nm. Since this wavelength is in the deep ultra violet regime and hard to generate, more suitable techniques have been developed, involving two-photon ionization processes with continuous wave lasers producing light at 235 nm.

The $S_{1/2}$ ground state is subdivided into the hyperfine levels with $|S_{1/2}, F, m_F\rangle$, where the $F = 1$ to $F = 2$ transition is about 1.25 GHz allowing for driving it with microwaves. The first excited electronic state $|P_{1/2}, F, m_F\rangle$ is accessible by ultraviolet light at a wavelength of 313.197 nm followed by the $|P_{3/2}, F, m_F\rangle$ at 313.13 nm. Thus, both levels are separated by 197 GHz. Since the transition from $|S_{1/2}, 2, \pm 2\rangle$ to $|P_{3/2}, 3, \pm 3\rangle$ is a closed cycle transition under circularly polarized light (σ^+ or σ^-), it is suitable for Doppler cooling the ions. However, due to imperfections in the polarization preparation of the light source and magnetic field inhomogeneities, linear polarization of the light is always present at a small fraction. Therefore, a repumper laser is employed to populate the cooling transition again. To align the ion quantization axis, a Helmholtz-like static magnetic field is applied along the laser axis. In a weak magnetic field, the Zeeman components are no longer degenerate, and the energy levels split according to

$$\Delta E_Z = g_F \mu_B B m_F \tag{8}$$

with the Landé factor given by the quantum numbers

$$g_F = g_J \frac{F(F+1) + J(J+1) - I(I+1)}{2F(F+1)} + g_I \frac{F(F+1) - J(J+1) + I(I+1)}{2F(F+1)} \tag{9}$$

The fine structure levels are illustrated in Figure 2. For a static magnetic field of 100 μT, the ground state frequency splitting is presented in Table 2 with corrected factors [75]. Thus, at a center frequency of 1247.916 MHz, the transition from $|S_{1/2}, 1, +1\rangle$ to $|S_{1/2}, 2, +2\rangle$ for the qubit is expected in such a field. Furthermore, a shift of $\delta\nu(B) \approx |B| \times (-20\,\text{Hz/nT})$ is anticipated for this transition. Consequently, the qubit can be utilized as a quantum sensor to probe the characteristic magnetic field environment in the trap.

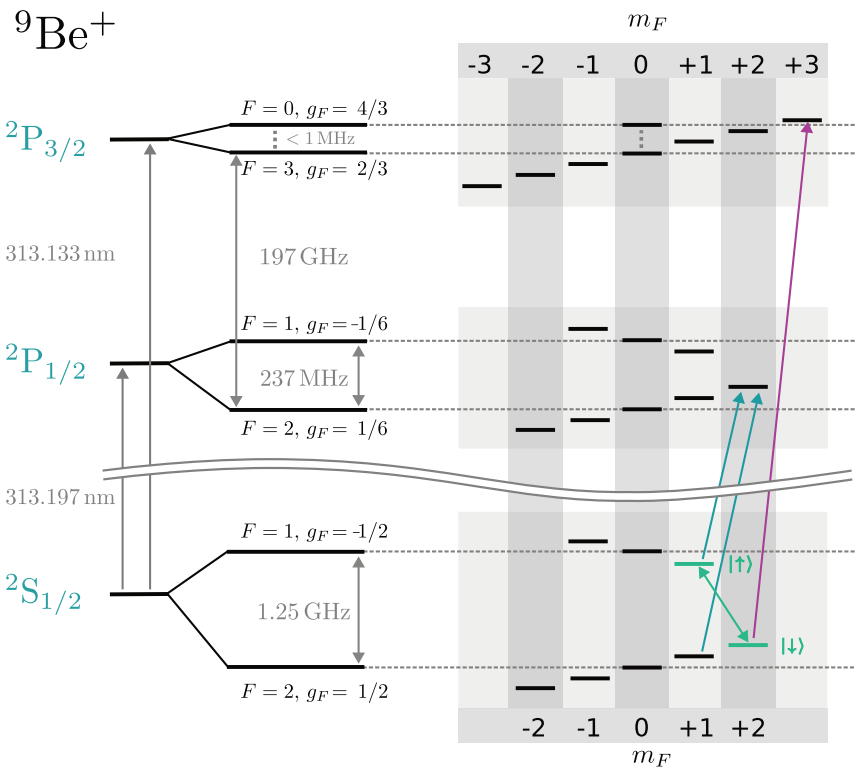

Figure 2: (Frequency splittings are not to scale) Relevant level schemes of Be^+ for Doppler cooling and microwave excitation. In green the repumping levels, purple cooling and state readout and green the microwave qubit transitions of the $^2S_{1/2}$ are highlighted.

Table 2: Calculated Zeeman shifts of the Be^+ $S_{1/2}$ ground state hyperfine splitting at a static magnetic field of 100 µT in MHz. The center frequency is 1250.0176(7) MHz [75].

m_F	−2	−1	0	1	2
F= 1		0.7010	0.0016	-0.6987	
F= 2	-1.4021	-0.7023	-0.0016	0.6998	1.4021

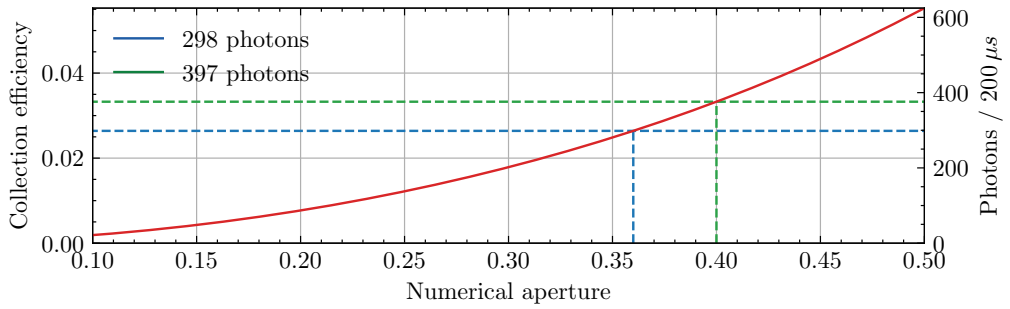

Figure 3: Collection efficiency of a dipole transition in dependence of the numerical aperture $NA = n\sin(\theta')$. A lens with $NA = 0.36$ obtains a collection efficiency of 2.6%, while for $NA = 0.4$ the efficiency is 3.3%. On average, this corresponds to 298 ph/200μs and 397 Ph/200 μs for a transition rate of $\Gamma/2 = 56 \times 10^6$ Ph/s, respectively.

2.1.1 Dipole emission of Be^+

For the driven $|S_{1/2}, 2, \pm 2\rangle$ to $|P_{3/2}, 3, \pm 3\rangle$ dipole transition, the emission characteristics defined by the normalized probability amplitude [76]

$$\frac{dP(\vec{r})}{d\Omega} = \frac{3}{8\pi}\frac{1+\cos^2(\theta)}{2} \tag{10}$$

With the differential solid angle $d\Omega$ and angle θ between the quantization axis and the emission direction. For application purposes, the quantity is integrated over the numerical aperture $NA = n\sin(\theta')$ with n defined as the refraction index of a medium. For a circular aperture orthogonal to the quantization axis one finds $\tan(\Phi) = \sqrt{\tan^2(\theta') - \tan^2(\theta - \pi/2)}$ such that

$$P = \int_{\pi/2-NA}^{\pi/2+NA}\int_{-\Phi}^{\Phi}\frac{3}{8\pi}\frac{1+\cos^2(\theta)}{2}\sin(\theta)d\theta d\Phi \tag{11}$$

The integrated values are shown in Figure 3.

2.2 QUADRUPOLE ION TRAPS

Linear quadrupole traps, commonly referred as Paul traps [61], are one of the cornerstones in the study of cold charged particles, since they allow a stable confinement in a well controlled environment. In modern experiments, the storage time is only limited by the vacuum quality, realizing measurement times of weeks to months. Such exceptional timescales enable interrogation times of atomic transitions with lasers resulting in the most precise frequency measurements achieved to date.

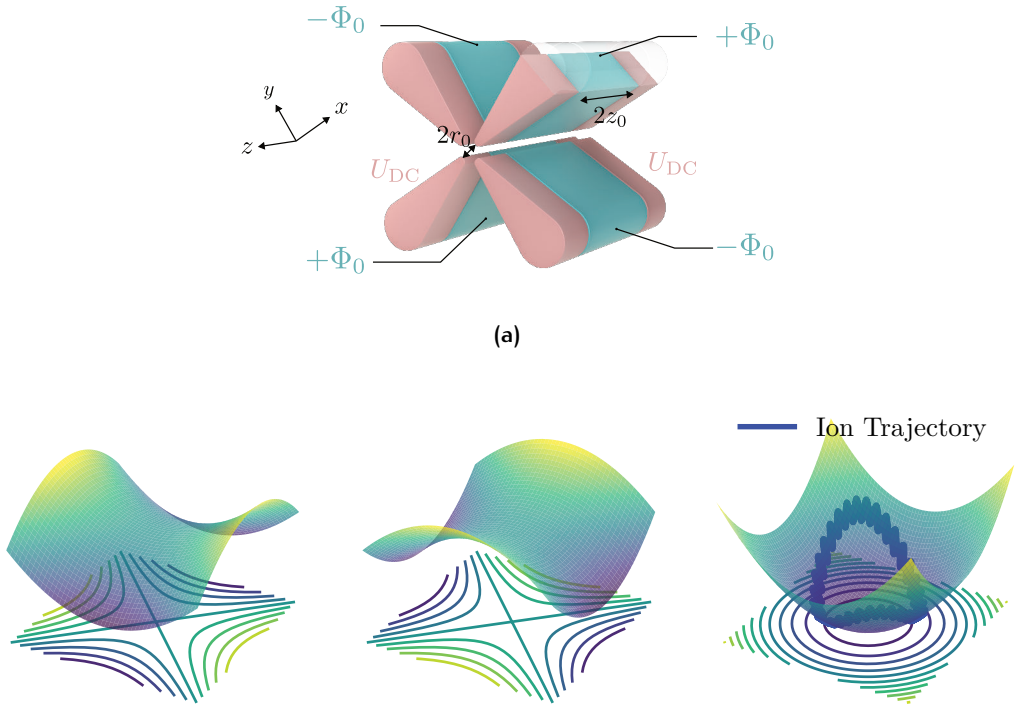

Figure 4: a) Hyperbolic electrode configuration with electrodes at the end of each RF blade. On the electrodes a DC potential U_{DC} is applied. r_0 describes the distance between trap center and electrodes and $2z_0$ the separation of the DC. b)-d) Qualitative plot of the radial, RF-driven potential described in Equation 14. b) saddle potential at a given time $t = 0$; c) saddle potential at $t = \pi/\Omega_{\mathrm{RF}}$; d) time averaged effective pseudo-potential. In addition, the equipotential lines $x^2 - y^2 = const$ are projected onto the x-y plane. An exemplary ion trajectory in the potential is shown including a low frequent secular and a high frequency micromotion.

2.2.1 The linear radio-frequency ion trap

Long, non-destructive confinement can be achieved by either utilizing static electric- in combination with a strong magnetic field, or dynamic electric fields. The potential Φ for latter can in general be written as

$$\Phi\left(x, y, z\right) = \alpha\, x^2 + \beta\, y^2 + \gamma\, z^2 \tag{12}$$

where α, β, γ are coefficients describing the field curvature along the respective axes [77]. To obey the Laplace equation $\Delta\Phi = 0$, the linear combination of the coefficients needs to be of the form $\alpha + \beta + \gamma = 0$. This condition is unattainable with purely static electric fields. Wolfgang Paul utilized an alternating, quadrupole field in 1958 [63]. Following his approach, a solution in for the radial component is given by

$$\alpha_{\mathrm{RF}} = -\beta_{\mathrm{RF}} = \frac{\Phi_0(t)}{r_0^2}$$

Here, $\Phi_0(t) = V_{\mathrm{RF}} \cos(\Omega_{\mathrm{RF}} t) + U_{\mathrm{DC}}$ represents the time-dependent potential, including both radio-frequency (RF), and static (DC) contributions, which prevent degeneracies of the trapped charged particle eigenmotions. In addition, a static potential is added along the axial (z) direction following

$$\alpha_{\mathrm{DC}} = \beta_{\mathrm{DC}} = -\frac{\gamma_{\mathrm{DC}}}{2} = -\frac{\kappa U^z_{\mathrm{DC}}}{2z_0^2} \tag{13}$$

Both potentials superimposed produce a dynamic confinement region as shown in Figure 4. The total field is then given by

$$\Phi(x, y, z, t) = V_{RF} \cos(\Omega_{\mathrm{RF}} t) \frac{x^2 - y^2}{r_0^2} + \frac{\kappa U^z_{\mathrm{DC}}}{z_0^2} \left(-\frac{1}{2}(x^2 + y^2) + z^2 \right) \tag{14}$$

Remarkably, in the trapping center, the potential vanishes completely. Furthermore ,along the z-axis, the radio-frequency contribution becomes zero. The ion motion in this potential is then described by the Mathieu equation, yielding three independent eigenfrequencies.

2.2.2 Equations of motion in an ideal, linear Paul trap

The resulting motion of a trapped charged particle with mass m and charge Q can be derived from Equation 14 and by substitution of

$$\begin{aligned} a_x = a_y = -\frac{1}{2} a_z &= -\frac{4Q\kappa U_{\mathrm{DC}}}{m z_0^2 \Omega_{\mathrm{RF}}^2} \\ q_x = -q_y &= \frac{4Q V_{\mathrm{RF}}}{m r_0^2 \Omega_{\mathrm{RF}}^2} \\ q_z &= 0 \\ \zeta &= \Omega_{\mathrm{RF}}\, t/2 \end{aligned} \tag{15}$$

the differential equations reduce to Mathieu's equation

$$\frac{d^2}{d\zeta^2} u + (a_u - 2q_u \cos(2\zeta)) \cdot u = 0 \quad , \; u = x, y \quad . \tag{16}$$

with ζ representing a dimensionless timescale depending on the trap drive frequency, a_u corresponding to the static DC component strength of the superimposed potential in absence of the quadrupole field and q_u, quantifying the oscillating potential amplitude. All six parameters do depend on the charge-to-mass ratio Q/m and characteristic length scales of the trap geometry r_0, κ, z_0. The exact solution for the Mathieu equation is given by

$$u(t) = A \sum_{n=-\infty}^{\infty} C_{2n} \cos(\beta_u + 2n)\zeta + B \sum_{n=-\infty}^{\infty} C_{2n} \sin(\beta_u + 2n)\zeta \tag{17}$$

Here, C_{2n} describe the Fourier components of the particle motion and β can be interpreted as a modulation parameter. In Equation 16 one can find different regions of

stable confinement. A trivial solution is the harmonic trapping potential, in which the ion exhibits a periodic motion at a well defined frequency. This solution is considered as adiabatic approximation, if the trapping potential is deep enough to allow a stable confinement, but as low as the ion motion and drive frequency Ω_{RF} are not degenerate. As shown in Figure 5, this parameter space is given by $|a_u| << |q_z| << 1.0$.

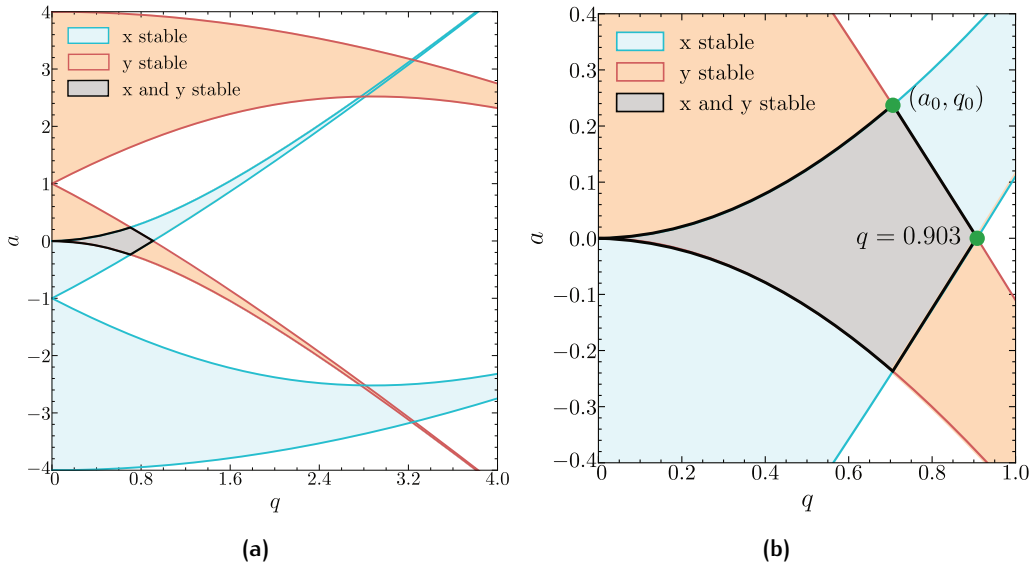

Figure 5: Stability diagram for a two-dimensional quadrupole mass spectrometer. The red and blue areas are showing the stable solutions of the Mathieu Equation 16 in x- and y-direction. In the gray area both solutions overlap and stable trapping in both directions is possible.

The solution then reduces to

$$u(t) \cong u_1 \cos(\omega_u t)\left(1 + \frac{q_u}{2}\cos(\Omega_{RF} t)\right) \tag{18}$$

where $\omega_u = \beta_u \Omega_{RF}/2$ is the eigenfrequency of the trapped ion, and $\beta_u \approx \sqrt{\frac{q_u^2}{2} + a_u}$ the approximated modulation, depending on the RF and DC potentials. Thus, the motion of a trapped particle is separated into the fast oscillating drive frequency Ω_{RF}, which vanishes along the trap axis due to its q_u dependence. On the other side of the term, a slower frequency ω_u with amplitude β_u is induced. For a particle with mass of $m = 9$u and charge $Q = 1e$, the eigenfrequencies inside a quadrupole potential is usually in the order of a few 100 kHz to 1 MHz with $\omega_z < \omega_x \cong \omega_y$ as a consequence of the stability condition. With that, the motion of a particle trapped in a harmonic oscillator can be described as

$$\Psi(x, y, z) = \frac{m}{2q}(\omega_x^2 x^2 + \omega_y^2 y^2 + \omega_z^2 z^2) \tag{19}$$

On the trap axis, the secular motion amplitude dominates. Further, it can be minimized through cooling the of trapped particle.

2.2.3 Mixed Coulomb Crystals

Highly charged ions do not feature a fast closed cycle transition in the optical regime [19]. Thus, Be^+ is co-trapped with a HCI in a harmonic potential. Since both ions are coupled, the kinetic energy of the highly charged ion is transferred to the continuously cooled Be^+ , allowing to reach equilibrium temperatures close to the Doppler temperature if their charge-to-mass ratio is similar [78]. For increasing mismatch of q/m particularly the radial modes uncouple, causing the cooling efficiency to decrease [79]. The equilibrium positions can be determined by describing the potential energy inside the potential by the secular frequencies [80]

$$V(\vec{r}_1, ..., \vec{r}_N) = \sum_i \frac{m_i}{2}\left(\omega_{x,i}^2 x_i^2 + \omega_{y,i}^2 y_i^2 + \omega_{z,i}^2 z_i^2\right) + \frac{1}{4\pi\epsilon_0}\sum_{i\neq j}\frac{q_i q_j}{|\vec{r}_i - \vec{r}_j|} \tag{20}$$

where (m_i is the mass of the i-th ion, $\omega_{x,i}$, $\omega_{y,i}$, and $\omega_{z,i}$ are the secular frequencies in the x, y, and z directions, respectively, q_i and q_j are the charges of the ions, and ϵ_0 is the vacuum permittivity. In equilibrium, the distance between two ions is determined by solving $\partial V/\partial z_i = 0$. Neglecting all other forces, the distance between two identical ions in the trap axis is then found as

$$z_i = \pm\sqrt[3]{\frac{Q^2}{16\pi\epsilon_0 m\omega_z^2}} \tag{21}$$

where Q is the charge of the ion, m is its mass, and ω_z is the secular frequency in the z direction. This relation is widely used to determine trap characteristics or charge states of the cotrapped HCI and only requires measurement of the eigenmotion.

2.3 LIGHT–MATTER INTERACTION

2.3.1 Doppler cooling

Inside the quadrupole potential, a stored ion obtains kinetic energy composed of micromotion and secular motion. For spectroscopy applications, the ions are located along the trap axis ($x = y \approx 0$). Additionally, an ideal trap potential ($q_z = 0$) is assumed, such that only the slower secular frequency contributes to the energy. By interacting with a directed light field, the motion amplitude can be reduced by inducing an average drag force. For a transition energy $\Delta E = \hbar\omega_e$, the light wave detuning from the resonance is given by $\Delta = \omega_l - \omega_e$, resulting in $\delta_{eff} = \Delta - \vec{k}\cdot\vec{v}$ in the rest frame of the ion. Here, $\vec{k}$ is defined as the wave vector of the incoming light field, $\vec{v}$ is the ion velocity vector, $\hbar$ is the reduced Planck's constant, and ω_e is the angular frequency corresponding to the energy separation between the two levels.

In addition to the detuning, a saturation parameter is introduced as follows:

$$s = 2\frac{\Omega_0^2}{\Gamma^2} = \frac{I}{I_S}, \tag{22}$$

where I is the intensity of the light field and I_S is the saturation intensity. If the ion is now continuously exposed to a field, driving a closed cycle transition such as the $|S_{1/2}, 2, \pm 2\rangle$ to $|P_{3/2}, 3, \pm 3\rangle$, the minimal achievable temperature is limited by the recoil momentum of the scattered photon and reads [77]

$$T_D = \frac{\hbar\Gamma\sqrt{1+s}}{4k_B}(1+\zeta) \tag{23}$$

where the transition frequency $\Gamma = 2\pi \cdot 17.97\text{MHz}$ [74] and correction parameter for electronic transitions $\zeta = 2/5$ [81] lead to a Doppler limited temperature of $T_D = 302\,\mu\text{K}$.

2.3.2 Rabi oscillations

The excited state probability density ρ_{ee}, which represent the population dynamics of a two-level system, can be described by the following equation:

$$\rho_{ee}(t) = -i\frac{\Omega_0}{\sqrt{|\Omega_0|^2 + \Delta^2}} e^{-i\Delta t/2} \sin\left(\frac{t}{2}\sqrt{|\Omega_0|^2 + \Delta^2}\right). \tag{24}$$

Here, Ω_0 is the Rabi frequency, which characterizes the coupling strength of the ion to the light field. With the squared complex amplitude returning the probability to reach the excited state, and by substituting $\Omega_R = \sqrt{|\Omega_0|^2 + \Delta^2}$, one finds

$$|\rho_{ee}(t)|^2 = \left(\frac{\Omega_0}{\Omega_R}\right)^2 \sin^2\left(\frac{\Omega_R t}{2}\right) \tag{25}$$

This equation shows several characteristics: First, the population transfer in a two-level system exhibits sinusoidal oscillation in time. Second, for complete transfer of the population, the field must be on resonance with the transition. Third, by modifying the excitation time, a population can be transferred to any required state.

Such an interaction is qualitatively shown in 6a, where multiple Be^+ ions were probed on the $|S_{1/2}, 2, 2\rangle$ to $|S_{1/2}, 1, 1\rangle$ hyperfine qubit transition. In Equation 22, the Rabi frequency depends on the incoupled intensity I and the natural linewidth Γ. Consequently, it decreases quadratically with a reduction in the light field intensity. Such a scaling is shown in Figure 6b, where the hyperfine transitions of multiple Be^+ ions were driven by a microwave field at different intensities. To probe the transi-

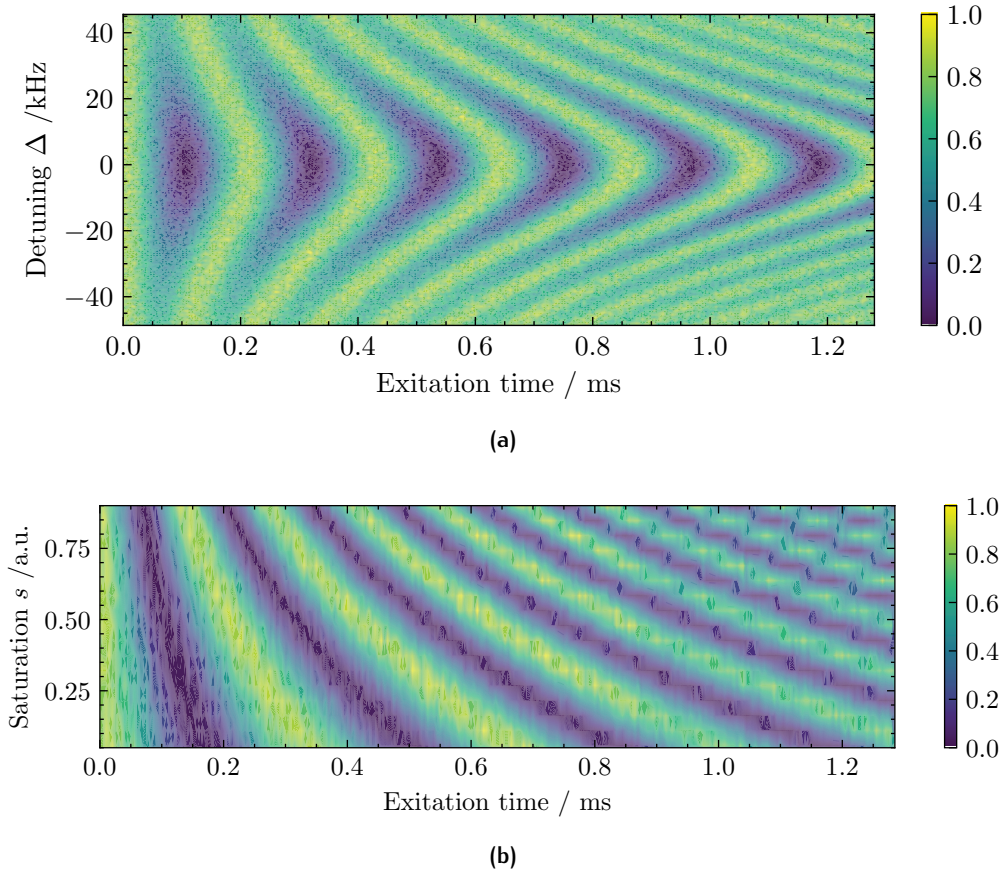

Figure 6: Rabi oscillations and excitation dynamics of a two-level transition are described by Equation 25. The colorbar scale shows the ground state population. These experiment results illustrate the relationship between excitation time t and (a) detuning Δ from-, (b) saturation intensity s on resonance for the $|S_{1/2}, 2, 2\rangle$ to $|S_{1/2}, 1, 1\rangle$ hyperfine qubit transition at about 1.25 GHz of multiple Be^+ ions. At resonance, the coupling is maximized, facilitating complete population transfer to the excited state. As the system is detuned off-resonance, the Rabi frequency increases, leading to a reduction in population transfer efficiency and a decrease in contrast. (b) For weaker intensities the Rabi-time increases quadratically. State detection was performed via electron shelving of the $|S_{1/2}, 2, \pm 2\rangle$ to $|P_{3/2}, 3, \pm 3\rangle$ cooling transition.

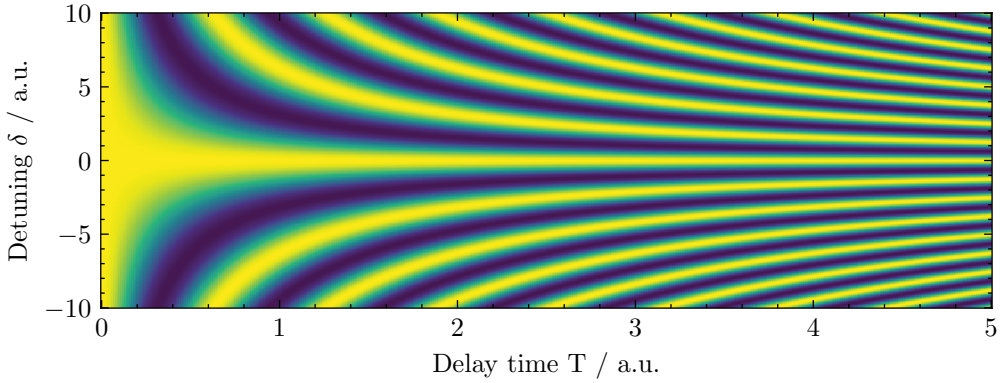

Figure 7: Qualitative illustration of Equation 27 with plotted delay time T versus detuning δ. $\tau = \pi/(\Omega_0 2)$ such that the equation reduces to the $\approx \cos^2(\delta T/2)$ term.

tion linewidth, rectangular pulses at varying detuning are applied, modifying the excitation probability to

$$|\rho_{ee}(\omega)|^2 = \left(\frac{\Omega_0 t}{2}\right) \mathrm{sinc}^2\left(\frac{\Omega_R t}{2}\right) \tag{26}$$

As a consequence, a maximum is achieved at $\Phi_R = \Omega_R t_\pi = \pi$ at a full width half maximum linewidth $\delta\nu \cong 1.6/(2t_\pi)$.

2.3.3 Ramsey Spectroscopy

On resonance, Equation 25 states, that the ground state population can be fully transferred into the excited state by applying a pulse at $\Phi_R = \Omega_R t = \pi$. Thus, at $\Phi_R = \pi/2$, the population exists in a coherent superposition of both states and evolves freely in phase space. By waiting a time T after the initial pulse, a second pulse Φ_R can be applied. In general, the excitation probability for such a scheme is given by [82]:

$$|\rho_{ee}(\delta)|^2 = (\Omega_0\tau)^2 \,\mathrm{sinc}^2\left(\frac{\Omega_R\tau}{2}\right)\left(\cos\left(\frac{\Omega_R\tau}{2}\right)\cos\left(\frac{\delta T}{2}\right) - \frac{\delta}{\Omega_R}\sin\left(\frac{\Omega_R\tau}{2}\right)\sin\left(\frac{\delta T}{2}\right)\right)^2 \tag{27}$$

Here $\delta = \omega - \omega_0$ represents the detuning from the resonance frequency, and τ is the duration of the initial pulse that initiates Φ_R. In Figure 7 such a Ramsey scheme excitation probability in dependence of the delay time T and detuning δ is plotted. It shows a $1/T$ dependence on the fringe spacing. During the waiting time T the quantum state phase is modulated by external noise and experiences decoherence effects. As a result, after application of the second pulse, the population is not completely transferred into the excited state. Since the decoherence effects tend to average out over the time scale T, a π pulse can be utilized to reverse the accumulated dephasing. Thus, after an additional time $T_2 = T$ the frequency noise components accumulated during that time period effectively cancel out, enabling much longer

precession times and improving the overall excitation probability. This, Hahn Spin-Echo method, is widely used for characterization of frequency shifts induced by the environment around the ion [83].

3 EXPERIMENTAL SETUP

In this Chapter, a brief overview on the Cryogenic Paul Trap Experiment with Superconducting resonator is given. Detailed descriptions to this setup can be found in [72]. To fulfill the main goal of this setup, providing a noise free environment for laser spectroscopy of HCI at highest precision, a superconducting quadrupole resonator acting as radio-frequency trap was implemented in a cryogenic, vibration uncoupled environment [72,84]. A Heidelberg compact electron beam ion trap [85] produces an ensemble of charge states by subsequently ionizing neutral or already ionized atoms interacting with a strongly compressed electron beam. This plasma is extracted from the EBIT with an energy of about 1000 keV/q and guided through a beam-line [86]. The charge state and ion species is identified by time-of-flight spectroscopy and selected with a fast switching kicker electrode. A set of ramp-able electrodes is finally slowing and bunching the ions of choice down to about 100 eV/q before they enter the floating trap region with a residual energy below 1 eV/q [58]. A pre-loaded and Doppler-cooled Coulomb crystal consisting of a few hundred Be^+ ions is interacts with the cycling HCI and removes subsequently kinetic energy until it crystallizes.

VAUQSI: A SISTER EXPERIMENT OF CRYPTEX-SC In addition to the existing cryogenic trap, a sister experiment is being developed investigating quantum computing applications of highly charged ions based on quantum logic spectroscopy. In the following substections, differences to the existing system will be highlighted.

3.1 HIGHLY CHARGED ION GENERATION

By compressing an accelerated electron beam emitted from a hot cathode in a strong magnetic field, current densities of a few 1 kA/cm can be reached [47, 85] corresponding to radii below 100 µm. Such high density boosts the probability of interaction with bound electrons in an atom and subsequently ionizes latter to the desired charge state within 100 ms – 1 s. In the Heidelberg compact electron beam ion traps, the 0.86 T superimposed magnetic field of the 72 attached NdFeB permanent magnets around the trap center is guided through a high purity soft iron yoke, which obtains a saturation induction of 2.15 T. An electron gun, consisting of two elec-

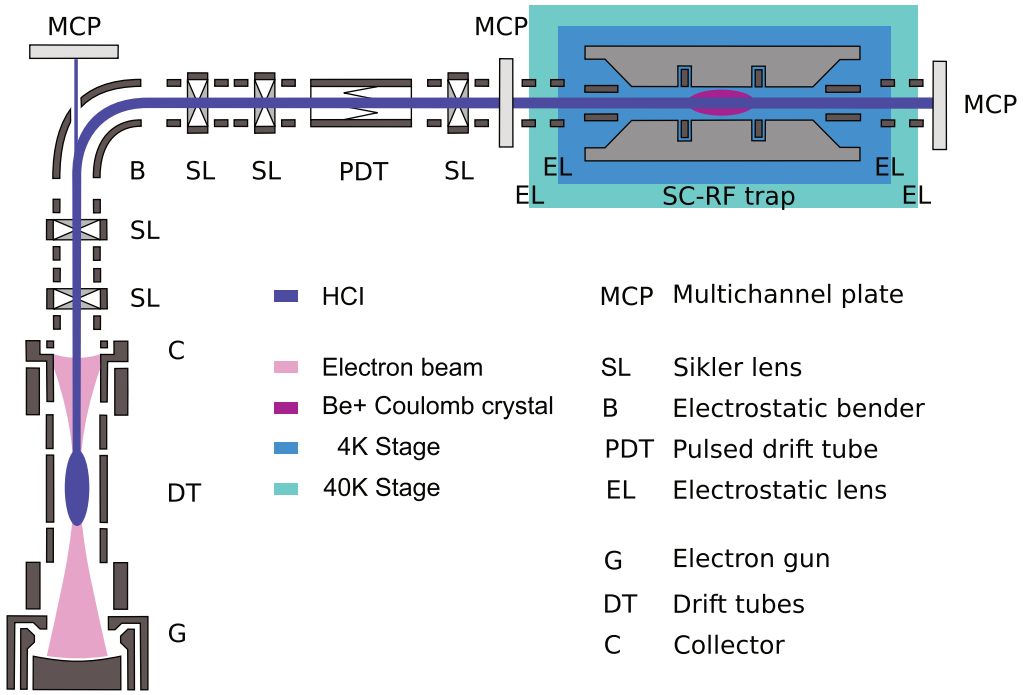

Figure 8: Schematic overview of the CryPTEx-SC experimental setup. The ions are produced in the electron beam ion trap and then periodically extracted. Through the beam-line, in total five Sikler lenses are installed to guide the HCI bunches to the trap. For optimization of the lenses, charge-state identification and -selection through time-of-flight spectroscopy, in total three multichannel plates were installed. A pulsed drift tube is used to decrease the HCI kinetic energy and compress the pulse. Inside the cryogenic trap environment, in total four einzel lenses were installed to shape and time the pulse entering the floating ground. For this purpose, they were utilized as retarding field analyzer. Around the RF blade electrodes two electrodes were installed for trapping the HCI inside the RF potential, thus allowing them to oscillate through a laser cooled Be^+ Coulomb crystal. Modified from [72].

trodes and a hot dispenser cathode is closely aligned to seven electrodes forming the trapping potential and accelerating the emitted electron beam, which is strongly compressed entering the magnetic field. The power supply limited emitted electron beam current is 10 mA at a maximum kinetic energy of 6 keV. Depending on the species, atoms are injected as gas though a leak valve and formed into a ballistic atomic beam which is overlapped with the electron beam in the center of a set of electrodes or ablated by a laser from a surface closeby [40, 42, 87]. At CryPTEx-SC, both methods can be applied, such that a large variety of ion species can be produced. The HCI are then ejected through a negatively biased collector, which stops and extracts the electron beam, and focused by a set of superimposed, slit einzel (Sikler) lenses [88]. Typical kinetic energies after ejection are in the order of $\approx 1\,\mathrm{keV}/q$.

3.2 HIGHLY CHARGED ION TRANSPORT

Due to the natural plasma characteristics inside an EBIT, the ejected bunches consist of multiple charge states and atomic species. To analyze the composition, several multi-channel plate detectors are installed at different sections of the beamline, allowing for characterization and optimization through time-of-flight spectroscopy methods [72, 73]. The separation of different charge states in time scales with $L \times \sqrt{m/q}$, where L is the beamline length. After identification, the charge state of interest is guided to the trapping region, while parasitic ions are removed by a fast-switching electrode [73, 86].

Including the aforementioned electrodes, as shown in Figure 8, the beamline, which directs the ions to the Paul trap, consists of five sets of Sikler lenses and a 90° electrostatic bender. Additionally, a set of crowned electrodes is used to decelerate and bunch the residual ions to kinetic energies of approximately $100\,\mathrm{eV}/q$ before they enter the floating ground trapping region at 100 V [58].

3.3 CRYOGENIC PAUL TRAP EXPERIMENT

While in an electron beam ion trap highly charged ions are continuously interacting with residual gas like hydrogen molecules, recombine and being ionized again by the electron beam, inside the Paul trap, this re-ionization process is not realizable anymore. Thus, the residual gas density needs to be decreased by orders of magnitude allowing for storage times in the order of minutes, hours or even days [89]. A suitable method to achieve such an environment is cryogenic pumping. For that,

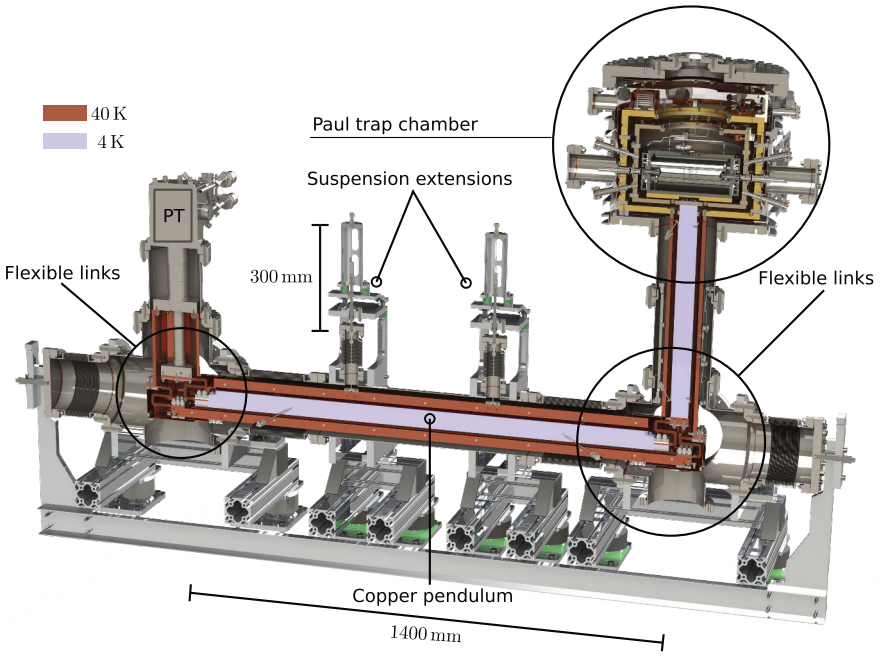

Figure 9: VAUQSI cryogenic supply system similar to [72,90]. The unit consists of three sub elements. On the left the pulse tube (PT) is shown, which is directly connected to an approximately 1400 mm long copper pendulum. On the right, the trap chamber including a superconducting resonator is shown. The pendulum suspensions were lengthened by 300 mm to reduce the pendulum eigenfrequency.

the surfaces facing the trapping region are cooled down to 4 K with a cryogen free cryostat.

3.3.1 Cryogenic Supply

The CryPTEx-SC experiment uses a closed-cycle pulse-tube cryocooler[1] containing two temperature stages, 4 K and 40 K. They obtain a cooling power of 1 W at 4.2 K and 40 W at 45 K, respectively [72]. To minimize thermal black-body radiation reaching the 4 K stage, it is fully shielded by the 40 K stage. Since the cold head mechanics inherently induce vibration nodes, ranging from 1 Hz – 1000 Hz, a three-segment thermal transfer unit was designed, uncoupling the trap surroundings from the environment [90].This unit consists of an approximately 1400 mm long, 130 mm diameter, 120 kg heavy copper pendulum, which is mounted to two 150 mm long, 2 mm diameter, stainless steel spokes. This pendulum acts as low-pass vibration filter and is connected through in total twelve flexible copper springs to pulse-tube and trap chamber, respectively. Each spring has a width of 25.4 mm and ten elements of 0.4 mm thickness produced by electrical discharge machining EDM processes resulting in a cross section of 101.6 mm^2 per link.

1 Sumitomo Heavy Industries RP-082

(a) (b)

Figure 10: (a) Flexible copper links connecting the 4 K cold head with the pendulum, before annealing and polishing of the end pieces. (b) Example of a polished surface.

Since for cryogenic temperatures below 40 K, the thermal conductivity of copper depends strongly on the purity, for the 4 K stage 99.999% pure copper (5N) was used, while 4N material covered the 40 K shields.

3.3.2 Trap chamber

At the end of the cryogenic supply system, a cylindrical OFHC copper heat shield with a diameter of 364 mm, 260 mm height and a wall thickness of 17 mm (at 40 K) cover the smaller 293 mm diameter, 200 mm high and 12 mm strong stage surrounding the ion trap at 4 K. To minimize heat input without losing mechanical stability, each shield is mounted by twelve radially symmetric stainless steel spokes to the next outer stage. Both temperature stages are connected to the pendulum via a vertical supply, which ends at the respective flexible copper links. To enable a floating ground potential in the trap, it is mounted on a 5N copper platform and connected through four sapphire blocks to the cold supply. Under ideal conditions, their combined sapphire thermal conductance is 6.4W/K at a thermal conductivity of 230 W/K/m [91]. A drawing of the floating platform is shown in Figure 12a.

To minimize inflows of background gas and improve vacuum quality, most of the twelve radial viewports are closed off by fused silica substrates. The ports on the trap axis and one thirty-degree port are left open to allow highly charged ions (HCI) and beryllium to enter the trap region. Consequently, mechanical gates have been designed to enable efficient pumping of the inner stages before and during the cooldown cycle. A PEEK finger, mounted on a linear manipulator, touches and lifts the first cop-

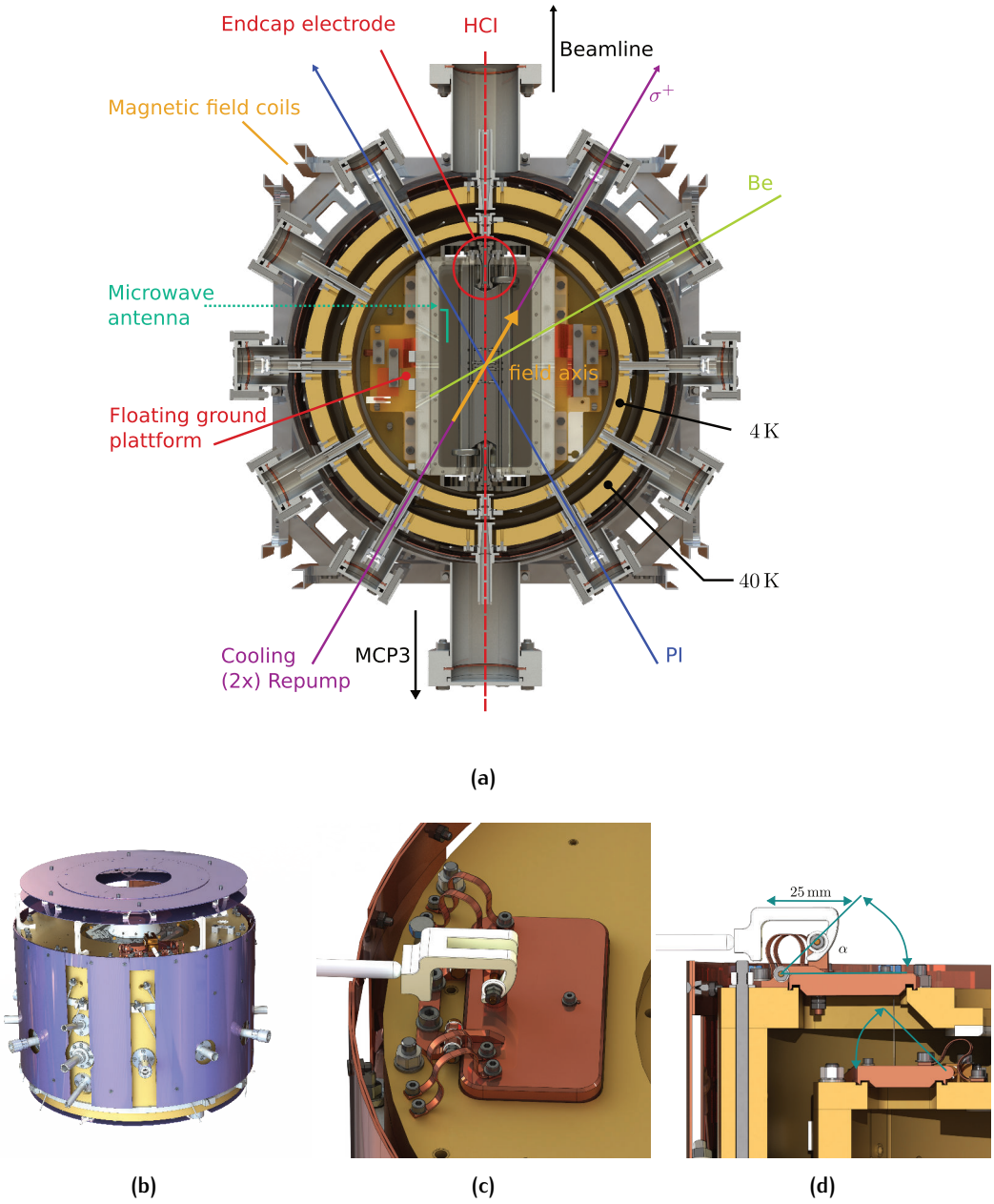

Figure 11: (a) Top view into the redesigned trap chamber of the VAUQSI experiment including a superconducting resonator. Twelve radially equal spaced viewports ensure sufficient optical access to the ions. (b) Side view on the heat shields. For the VAUQSI experiment a third layer copper sheet (blue) surrounds the 40 K heat shield. (c) Top view on the 40 K mechanical gate. (d) Side view of (c) with schematic of the mechanics.

per plate, measuring $87 \times 47 \times 8\text{mm}^3$, by retracting an arm. The plate, thermalized to 40 K, covers a $40 \times 80\text{mm}^2$ opening. A Kevlar wire, screwed to it, mechanically connects to a second plate at the 4 K stage and pulls it up to an angle of about 40°. Both assemblies are fastened with greased[2] hinges to the respective shields and open outwards. Additionally, for increased cooling efficiency, four flexible braids are connect each plate to its shield. In the open state, the pumping cross-section increases before cooldown, reducing the partial pressure inside the 4 K shields. In closed state, it enhances the HCI lifetime by suppressing the reionization probability at cold temperatures.

THERMAL RESISTANCES OF THE CRYOGENIC SUPPLY SYSTEM During the commissioning phase, a 1 K Ω heating resistor was attached to the trap chamber to stabilize the superconducting resonator temperature or to increase it beyond the phase transition without turning off the cryogenic supply. By increasing the heat load on the trap side, the thermal resistivity of the flexible copper links was determined. For the 40 K stage, the total thermal resistance was extracted from the cryogenic heat capacity map and estimated to be ≈ 1.5 K/W, with contributions of $R_{PT} = 0.64$ K/W for the pulse-tube connector and $R_T = 0.65$ K/W for the trap-chamber link. In the 4 K stage, a total resistance of 8.7 K/W was directly measured.

This value was about one order of magnitude higher than expected, indicating either a bad connection of one or more thermal links or an issue at one of the connections in the trap chamber. To address this, the flexible links were first polished to remove gaps caused by roughness induced by the EDM process, as indicated in Fig. 10. They were then annealed under vacuum at 300 °C overnight. As a result, for the 40 K stage, the resistances decreased to $R'_{PT} = 0.40$ K/W and $R'_T = 0.30$ K/W, while the resistance for the 4 K stage remained at the value measured before treatment, indicating a persistent bad connection closely related to the trap chamber.

Two sections were specifically examined: the eight stainless steel bolts pressing the vertical 4 K stage against the heat shield, which were mounted with helicoils, were investigated and retightened. Additionally, eight bolts that mount the resonator on the floating platform and apply pressure on the sapphires, which connect last with the heat shield, were fixed again with more caution. Despite these measures, there was no improvement in thermal resistance.

Since both the temperature sensor and the thermal heat resistor are mounted on top of the resonator, two scenarios remain: either the thermal resistance of the high-

2 Apiezon N

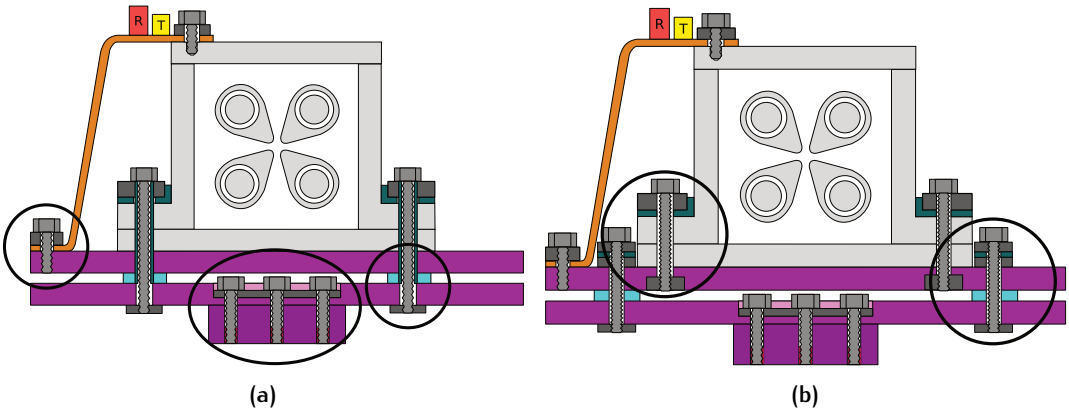

Figure 12: (a) Schematic representation of the floating ground platform of CryPTEx-SC. The copper elements, depicted in purple and orange, illustrate the connection between the resonator and the bottom vertical thermal conduction line. Insulators are highlighted in magenta. The positions of the heat resistor (R) and temperature sensor (T) are also indicated. The black circles mark the discussed locations in Paragraph 3.3.2. (b) Illustration of the redesigned platform featuring separated screws that securely mount the resonator to the platform, as well as the platform to the 4 K heat shield. Adapted and modified from [72].

purity copper plate connecting the sensor and resistor degraded during cold processing, or the thermal connection to the floating ground is insufficient. The cross-section of the plate is $A = 50\,\text{mm} \times 4\,\text{mm} = 200\,\text{mm}^2$ over a total length of $L = 164\,\text{mm}$. With the estimated thermal resistance, this leads to a conductivity of $k = L/(R \cdot A) = 94\,\text{W/K/m}$, which is approximately one order of magnitude below typical values for low-purity copper, indicating a poor thermal connection between the floating ground platform and the plate.

In the extreme case where no connection exists between the copper pieces, the heat would flow through the resonator via a cross-section of $5900\,\text{mm}^2$ over a length of 94 mm. This scenario would imply a lower bound for conductivity of 1.8 W/m/K, which is too low. For superconducting niobium, the thermal conductivity has been determined to be $\approx 10\,\text{W/m/K}$ [92].

VAUQSI FLOATING GROUND While it is unclear what causes the thermal resistance in the trap chamber area, measures have been taken to avoid similar issues in future experimental setups. We have redesigned the floating ground, as illustrated in 12b. In the new design, the superconducting resonator is securely attached to the floating ground platform using eight screws. Additionally, the sapphires have been repositioned further outward to ensure direct access to another eight screws. Moreover, the 4 K shield, which supports the floating platform, is now constructed from high-

purity 5N copper instead of the oxygen-free high conductivity (OFHC) copper used in the CryPTEx-SC setup. This change is intended to enhance thermal conductivity between the vertical connection stage and the 4 K heat shield.

VAUQSI THIRD COPPER SHIELD LAYER For the 40 K cryogenic stage, the thermal radiation power input is estimated to be 15.67 W [72] by using the Stefan-Boltzmann Law [91]:

$$\dot{Q}_{\mathrm{R}} = \frac{A_1 \sigma_{\mathrm{B}} (T_2^4 - T_1^4)}{\frac{1}{\epsilon_{s,1}} + \frac{A_1}{A_2}(\frac{1}{\epsilon_{s,2}} - 1)} \tag{28}$$

This equation is applicable for long concentric cylinders, where σ_{B} is the Stefan-Boltzmann constant, and A_i, T_i, and $\epsilon_{s,i}$ represent the surface area, temperature, and emissivity of each surface, respectively. By recapitulating the dimensions given for the cryogenic supply line, it is found that about 40 % the 40 K heat input is induced on the vertical copper pendulum, and 30 % on the trap chamber side, including the top and bottom covers, which are modeled by:

$$\dot{Q}_{\mathrm{P}} = \frac{A_1 \sigma_{\mathrm{B}} (T_2^4 - T_1^4)}{\frac{1}{\epsilon_{s,1}} + \frac{1}{\epsilon_{s,2}} - 1} \tag{29}$$

In order to reduce the heat load, sheets of copper were loosely positioned on the 40 K shield to prevent thermal coupling. For the radiative power input equilibrium, $\dot{Q}_1 = \dot{Q}_2$, a thermalization temperature of $T\mathrm{sheet} \approx 250\,\mathrm{K}$ is estimated, which reduces the effective load on the 40 K horizontal pendulum and trap region by a factor of two.

3.4 PRODUCTION OF BERYLLIUM IONS

Connected to the chamber at a 30° angle to the trap, a 1250 K hot oven, heated by a filament, continuously emits beryllium atoms. These atoms pass through two apertures and a skimmer over a 872 mm distance before entering the trap region. This process reduces the beam diameter to 960 µm, ensuring a low Doppler shift and minimizing depletion on the trap electrodes, which are separated by 2 mm. Perpendicular to the atomic beam axis, a 235 nm continuous wave laser[3] is overlapped at the trap center. This laser ionizes the atoms via two-photon ionization, accessing the $2p^1P_1$ level of the atoms. Doppler cooling is achieved using two frequency-quadrupled diode lasers[4]. These lasers are detuned to the transitions $|S_{1/2}, F = 2, m_F = +2\rangle$ to $|P_{3/2}, F = 3, m_F = +3\rangle$ (cooling) and $|S_{1/2}, F = 2, m_F = +1\rangle$ to $|P_{1/2}, F = 2, m_F = +2\rangle$ (repump), respectively. To access the second transition $|S_{1/2}, F = 1, m_F = +1\rangle$ to

3 Toptica DLC TA-FHG PRO
4 Toptica DLC BE+ COOLING

$|P_{1/2}, F = 2, m_F = +2\rangle$, the repump laser is split in two. One path is double-passed through two acousto-optical modulators with 425 MHz and 200 MHz modulation frequencies [93]. All three beams are coupled into a fiber and transferred to an optical table near the trap vacuum chamber. Due to the mode clean up in the fiber, they can considered as Gaussian beams. Before entering the trap, they undergo polarization clean-up by passing through a Glan-laser, followed by a set of $\lambda/4$ and $\lambda/2$ waveplates to achieve an enhanced σ^- purity [93].

3.5 EXPERIMENTAL CONTROL SYSTEM

For control of the voltage supplies of the trap, generating the RF-signal for the AOM and Microwave antenna, as well as timing pulse sequences on them and read out the PMT, an open source FPGA driven hardware [94] was used. The programs written for the FPGA are implemented by the ARTIQ framework [95]. For driving the 1.25 GHz hyperfine transition, the third Nyquist region of the synthesizer was used [96]. All frequency generators and timing critical instruments were referenced to a frequency clock signal providing a stability of $10^{-10}\sqrt{s}/\sqrt{\tau}$.

3.5.1 Optical system

A cost-efficient collection microscope consisting of six commercially available lenses is mounted directly on the resonator, forming an intermediate focus of the light emitted by the beryllium ions in between the heat shield temperature stages at a distance of 157 mm from the trap axis [73]. A single bi-aspheric lens [97] projects the intermediate focus either through a 50/50 beamsplitter plate onto an electron-multiplying charged-coupled device (EMCCD)[5] and a photo-multiplier tube (PMT)[6], or, by remotely flipping a motorized mirror, directly onto a second PMT to maximize the detected photons [93]. On the camera plane, the magnification is 8x to 20x, depending on the distance of the aspheric lens to the intermediate focus. The collecting lens features a nominal numerical aperture $NA = 0.36$, of which 90% are transmitted due to obscuration of a grating on top of the ion trap. In front of each PMT, two knife-edge apertures with an rectangular shaped opening of up to 5 mm filter out stray light from the trap. While the EMCCD/PMT combination can be moved into focus, the light on the second PMT is unfocused, such that only for the first can the filter be utilized to focus on a single ion. From Section 2.1.1, the integrated photon count rate in the timeframe of 200 µs, is about 300 Ph/200 µs . This is the integration time,

5 Andor iXon Ultra 888
6 Hamamatsu H10682-210

where off-resonant scattering is still suppressed at low saturation parameters $s \approx 0.2$. With a quantum efficiency of 30%, the average number of photons per readout of the $|\downarrow\rangle$ state by probing the Doppler cooling transition at $s = 2$, under perfect conditions, is 16.2 Ph/200 µs, neglecting absorptions and reflections from the substrates and surfaces. This is in good agreement with the results of [93] showing on average 14.47 Ph/200 µs for state readout. Due to the large photo-sensitive surface are of $\pi(4\,\mathrm{mm})^2$, most of the collected photons reach the PMT. Considering the strong aberrations of the system shown in Figure 19, discrimination of the individual signals in a multi-ion crystal is, however, currently not possible.

4 EXPERIMENTS ON A SUPERCONDUCTING ION TRAP

While many experiments regarding charged ions stored in an radio-frequency quadrupole field are performed by applying an amplified radio frequency to normal conducting, mostly gold plated blade electrodes [57,98], the trap in this thesis utilizes the properties of superconductivity. Within the last decades, many concepts were investigated, involving high temperature superconducting material coated on the electrodes [99] and micro-fabricated traps [100,101] driven by external electronics or micro-lumped circuits. Furthermore, macroscopic designs have been presented earlier for retrapping of anti-protons [102]. This project based on an integrated, macroscopic LC-circuit for amplification of the radio-frequency field utilizing the low surface resistance of superconducting niobium analogue to linear accelerator cavities. Based on the same principle, independently a superconducting trap was developed at the Max-Planck-Institute for Nuclear Physics in Heidelberg [72], commissioned [84] and successfully tested [73].

Within the accelerator community, most resonators reaching for resonances between 300 MHz to 3GHz resulting in cavity dimensions of about 1000 mm at extremely high quality factors $\Omega_{\mathrm{RF}}/\Delta\Omega \geq 10^8$.

Niobium is a type II superconductor and by passing the phase transition temperature of $T_{\mathrm{C}} = 9.3,\mathrm{K}$ a substantial reduction in electrical surface resistance is achieved. Consequently, the dissipated energy is decreased, while the resonance linewidth narrows due to the increased quality factor. The feedback to the electric field from a temporal change in current density stored in the superconductor is described by the London theory [103] and is given by

$$\frac{d\boldsymbol{j}}{dt} = \frac{c^2}{4\pi\lambda_L^2}\boldsymbol{E} \tag{30}$$

where λ_{L} is a temperature-dependent material characteristic that includes a charge density n_{s} corresponding to superconducting electrons. It is formally known as the London penetration depth and is defined by

$$\lambda_{\mathrm{L}} = \sqrt{\frac{mc^2}{4\pi n_{\mathrm{s}} e^2}} \tag{31}$$

This quantity is similar to the skin penetration depth

$$\delta_0 = \sqrt{\frac{c}{2\pi\omega\sigma}} \tag{32}$$

of normal metals. However it is independent of the frequency. Within the second London equation, the internal magnetic field intensity $\boldsymbol{H}$ acts on the superconducting charges as follows:

$$\nabla \times \boldsymbol{j} = -\frac{c}{4\pi\lambda_L^2}\boldsymbol{H}. \tag{33}$$

This equation marks a fundamental difference between normal conductors and superconductors, as it replaces the classical law of Ohm and requires the presence of a magnetic field in the presence of current densities. For the stationary state, following Equation 3, one finds:

$$\nabla^2 \boldsymbol{H} = \frac{\boldsymbol{H}^2}{\lambda_L^2} \tag{34}$$

Thus, in the weak limit, if an external magnetic field $\boldsymbol{H}_{\text{ext}}$ is applied, it will not penetrate the superconducting material but will be compensated by charges on the surface that flow parallel to the surface and perpendicular to $\boldsymbol{H}$:

$$j(x) = -\frac{c}{4\pi\lambda_L}\boldsymbol{H}_{\text{ext}} z e^{-x/\lambda L} \tag{35}$$

This relation is well known as the Meissner-Ochsenfeld effect. Consequently, a superconductor in a Meissner state is close to being a perfect diamagnet, and fields inside the material are expelled.

4.1 THE SUPERCONDUCTING QUADRUPOLE RESONATOR

The MPIK trap is a quasi-monolithic superconducting niobium radio-frequency resonator, generating a high fidelity quadrupole field obtaining a resonance frequency of about $\Omega_{\text{RF}} = 2\pi \cdot 34.4\,\text{MHz}$ at a quality factor of $Q \approx 3 \times 10^4$ in earth magnetic field. To achieve this frequency, the frame fills only a $220 \times 140 \times 114\text{mm}^3$ volume. It consists of two lids and a robust EDM machined central body. The two lids are pressed onto the central enclosure using several screws. Between the parts, there is a lead wire seal, which establishes a superconducting contact. Within, four, quasi hyperbolic electrodes form a quadrupole field. The resonance frequency is defined by

$$\Omega_{\text{RF}} = \frac{1}{\sqrt{LC}} = \frac{QP_{\text{D}}}{U} \tag{36}$$

where L and C are the resonator inductance and capacitance, Q the inverse bandwidth or quality factor of the resonance, P_{D} the dissipated power and U the stored energy inside the resonator. In first order, the inductance of $L \approx 20\text{nH}$ is given by the

surface area inside the housing resulting in a quadrupole resonance of about 1GHz. To achieve the small form factor, the capacitance was increased from about 1pF to $C = 928\text{pF}$ by folding one cylindrical rod into each blade electrode with a separation of 300 µm [84].

Radial secular frequencies up to $\approx 700\,\text{MHz}$ can be achieved, with an operating temperature close to the critical temperature of lead around 7.2 K.

At both RF-blade ends, in total two fast ramping end-cap electrodes, separated by about 156 mm are confining the injected HCI in axial direction. Recrystallization in a preloaded Be^+ Coulomb crystal is usually achieved at residual kinetic energies of about 1 eV/q inside a shallower harmonic trap. Here, two electrodes per blade apply a potential difference of just a few volt, allowing for ionization and laser cooling of Be^+ in a well defined due to their 8.2 mm axial spacing.

The end-cap electrodes

During commissioning, the endcap electrodes coupled to the radio-frequency field due to the asymmetric shape of the RF-blades, which reduced the achievable stored RF power by a factor of two [72]. To overcome this, 66 MΩ resistors were utilized as RF block. Consequently, the achievable electrode ramping time decreased due to parasitic capacitance induced by the resistor, requiring higher ramping voltages. This resulted in a coupling to the preloaded laser cooled Be^+ Coulomb crystal, which lead to heating and losses of the ions. To overcome this, a new set of niobium end cap electrodes were developed, consisting of an outer tube, which was coupled to the resonator by lead wire, and an inner electrode, connected directly to the ramping dc power supply. Even at smaller coupling strengths, the ion experience strong AC-fields emitted by the electrodes. This feature is generally used to identify the ion secular frequency for calibration of experiments by resonantly exciting the ion motional amplitude by coupling in AC-voltages through the electrodes.

4.1.1 Design of the VAUQSI resonator

To increase the number of available degrees of freedom for optimizing the DC potential for longer, the number of electrodes was doubled to sixteen. Of particular interest is the minimization of the micromotion amplitude, which is induced by off-axis ion storage. To allow for individual biasing, each electrode is coupled to a rod with a diameter of 1.8 mm, mounted parallel to the RF blade electrodes. Similar to

the CryPTEx-SC resonator [72], each electrode, in combination with its rod, exhibits a capacitance on the order of 10 pF relative to the RF blade. However, in contrast to the existing resonator, the electrodes in this design are not connected to the rods via screw connections but are instead electron-beam welded. This ensures a superconducting contact and reduces losses. To facilitate assembly, the RF blade was also modified so that the rods are now directly exposed to the RF field rather than being passed through a cut tunnel. The top flange was slightly modified to accommodate a new optics system by closing the iris grid surface to align with the rest of the lid. Additionally, the inner part of the grid was adjusted to be flush with the inner surface of the lid. These changes ensure an enhanced symmetric distribution of the RF fields within the inner part of the trap, potentially reducing contributions to the AC-Zeeman shift, which have been recently measured [93, 104]. The current resonator revision is shown in Figure 13.

4.2 THE MEISSNER EFFECT

Equation 35 holds even for non-perfect superconductors with a modified penetration depth $\lambda_D = \lambda_L\sqrt{\xi_0/\beta l}$, accounting for material impurities [105]. Here, l is the mean free path, β is a numerical constant, and ξ_0 is the characteristic coherence length. Furthermore, the Meissner effect ensures that the magnetic field is expelled from the interior of the superconductor at the phase transition. The internal magnetic field remains effectively zero due to the supercurrent, even if the external magnetic field changes.

This property was evaluated by inducing a magnetic field through the coils attached to the trap chamber while cycling the resonator temperature once between 4 – 12K by applying a voltage of 40 V to the resistor flanged on top of the niobium frame. The material is eventually penetrated by the magnetic field in the normal conducting state. After thermalization multiple ions were prepared in the trap. Since the field was initially not optimized to align with the axis of the incoming cooling laser field, the ions experienced partially π-polarized laser light and scattered into the dark state by blocking the repumper. Continuous microwaves radiation was induced by the antenna, scanning around 1.25 GHz for the hyperfine levels. On resonance, the microwaves pumped the population back into the $|S_{1/2}, 2, +2\rangle$ state, allowing for photon scattering of the cooling laser. This process was repeated by inverting the light polarization to σ^-, in order to access the negative m_F states at higher transition probabilities. After identifying the corresponding $|S_{1/2}, F = 1, m_F\rangle$ to $|S_{1/2}, F = 2, m_F\rangle$ frequencies, the magnetic field coils were turned off and the experiment was repeated

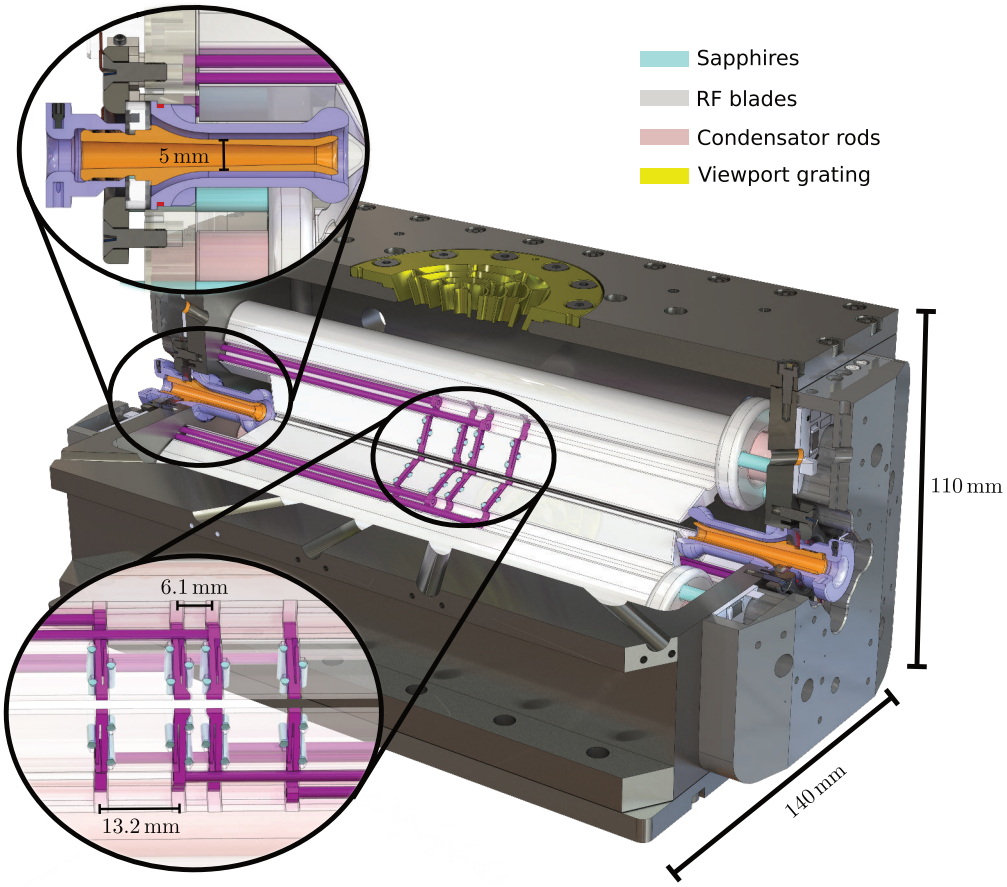

Figure 13: False color, sliced rendering of the VAUQSI superconducting quadrupole resonator. On the top left, the improved endcap electrodes are shown. Compared to the design of [72], in the region, where the RF potential is acting (orange), a second, grounded electrode (blue) is wrapped around it. In red, the lead wire is indicated. The whole assembly is mounted onto the resonator housing by a ring held by four screws. For electrical insulation of the inner part from ground, a sapphire ring separates it. Surrounding the endcap electrodes, a niobium inhousing shielding a set of filters for the DC block is shown. Note that the final DC electrode design as shown in purple is currently under revision, such that the characteristic scale $\kappa = 0.39$ (compared to $\kappa_{\mathrm{CSC}} = 0.35$) is given as a preliminary value in this thesis.

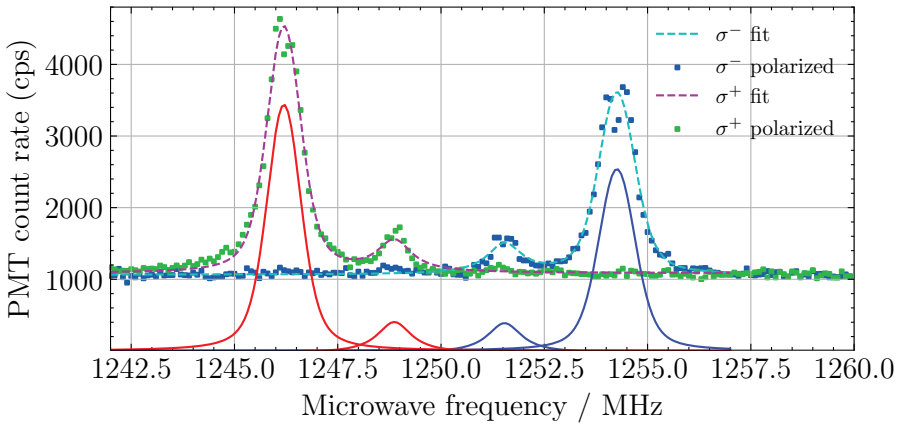

Figure 14: Electron shelving of Be^+ outer hyperfine transitions by incoupling of microwave power. The polarization was switched from σ^+ to σ^- to increase the contrast on both sides. For the scan the magnetic field coils were turned off, after phase transition. The hyperfine spacing indicates a field of about

for a second time. The result is presented in Figure 14 and shows the a stored magnetic field amplitude of about $B_0 = 190(1)\,\mu\text{T}$.

For a more exact measurement of the hyperfine splitting, a Ramsey scheme was performed, driving the qubit transition at a Rabi time of 33 µs at a waiting time up to 1 ms yielding a field strength of 190.5026(3)µT [73]. The magnetic field was stored for a total time of 150 days. Due to natural impurities inside the niobium, the induced magnetic field experiences a finite resistivity $R_S = L/\tau_S$ leading to a exponential decay with a time constant τ_S [106].

$$B(t) = B_0 \exp(-t/\tau_S) \tag{37}$$

The results shown in Figure 15 and resulted in a time constant of $\tau_S = 300\,\text{yr}$ which

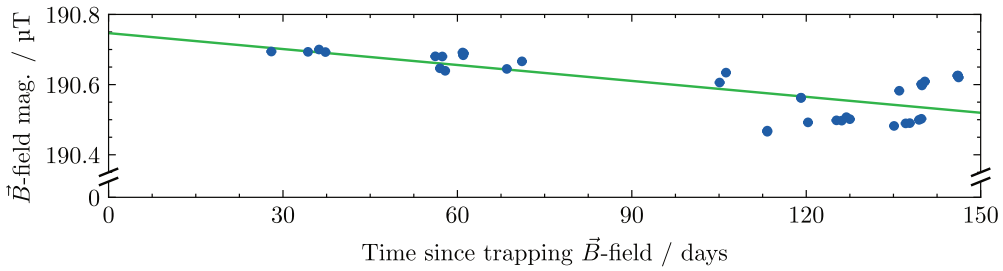

Figure 15: Magnetic field decay observed by measuring the magnetic field sensitive field Zeeman splitting in Be^+ . The decay constant is $\tau_S = 300\,\text{yr}$. Taken from [73].

corresponds to a magnetic field drift of

$$\frac{1}{|\boldsymbol{B}|}\frac{d|\boldsymbol{B}|}{dt} \approx 1 \times 10^{-10}/\text{s} \tag{38}$$

[73] For the determined inductance, the resulting resistivity then becomes $R_S = 0.9{\times}10^{-16}\,\Omega$, which is consistent with estimations of superconducting magnets [107].

With these results the DC component of the stored magnetic field was determined and the static part of the Meissner-Ochsenfeld effect confirmed. By increasing the Ramsey waiting time, the accumulated phase noise in the superposition state leads to a reduced population transfer by the final pulse to the readout state. After infinitely long waiting time, the probability to reach the qubit $|\uparrow\rangle$ or $|\downarrow\rangle$ states is equally 50 %. If a Gaussian noise is assumed to accumulate on the phase, the population dynamics are modified to $|\rho_{ee}|^2 = |\rho_{ee}|^2 \exp(-t^2/2\tau_1^2)$ [108,109]. A measurement sequence was performed for phase accumulation times up to $T = 500\,\text{ms}$, quantifying the Gaussian noise. The plot is shown in Figure 16. For a single stored Be^+ , the noise-correlation time was determined to be $\tau_1 = 414(22)\text{ms}$.

Last, the Hahn-Spin-Echo [83] scheme was applied to refocus the phase. Here, the ions are insensitive to linear drifts and Gaussian noise at a frequency $1/T$, where T is the waiting time after the initial $\pi/2$ pulse transferring the qubit state into a superposition. After applying the π pulse, for refocusing, a second waiting time T was initiated before transferring the population into the final excited state. As a result, within that $2T$ timeframe, the noise contribution of the magnetic field fluctuations are given by

$$\sqrt{|\Delta B^2|} = \frac{\hbar}{\mu_B \Delta(g_F m_F)\tau_1} \tag{39}$$

was determined to be 3.5(2)pT, corresponding to the measured Gaussian coherence time of 2.2(1)s [73]. Such a value is similar to previously measured fluctuations in ion traps utilizing permanent magnets [109]. For the CryPTEx-SC setup however, no magnetic field stabilization was applied. Only the superconducting niobium resonator in combination with the copper shields surrounding it attenuated magnetic noise contributions. Copper features a low resistivity at cryogenic temperatures inducing a skin effect (Equation 32) and attenuates noise depending on their frequency passing the material by inducing eddy currents [98]. For a similar trap with equal shield thicknesses fabricated from the same ingot[1], the redidual field noise was in the order of 200pT [98]. Thus, the two residual orders of magnitude correspond to the field expelling properties of the superconducting resonator.

1 Montanwerke Brixlegg

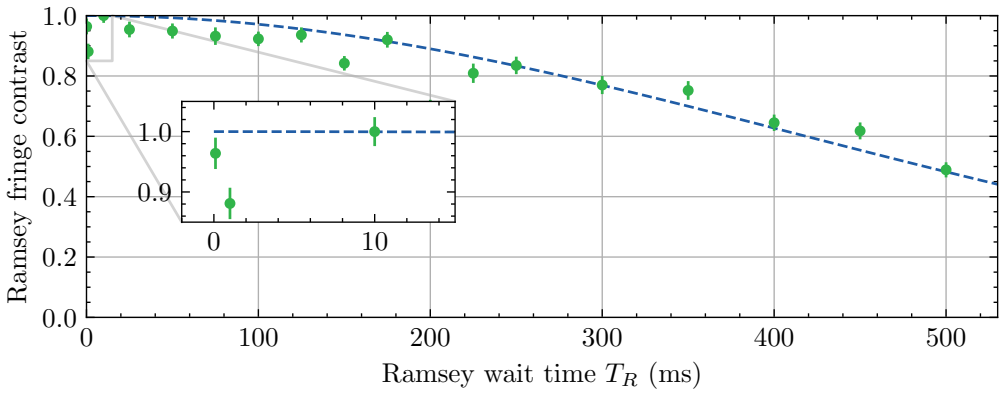

Figure 16: Decoherence measurements by applying a Ramsey scheme to a single ion resulting in a coherence time of $\tau_1 = 414(22)$ms. Taken from [73].

4.3 RABI SPECTROSCOPY

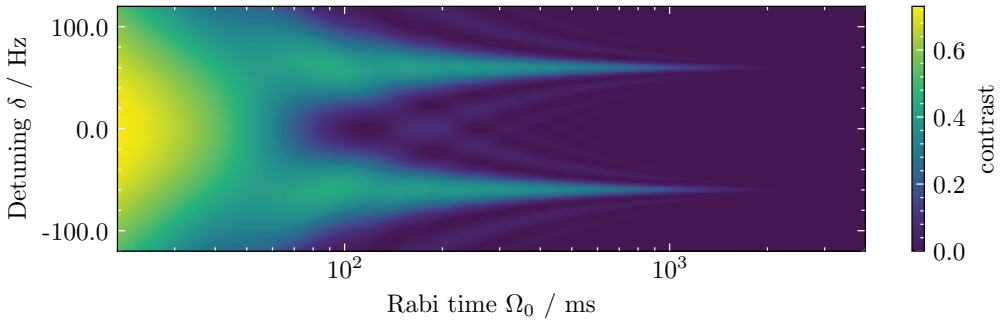

Figure 17: Plot of Equation 25 showing increasing Rabi times, corresponding to decreasing Fourier linewidths and contrast simulations of two ions separated by about 60 Hz including the measured decoherence parameter $\tau = 500$ ms.

The coherence times shown in the last section allow for investigation of a potential magnetic field gradient induced by the coils and stored in the trap. By decreasing the incoupled microwave power, the Rabi time is increased up to 150 ms. Thus the Fourier limited linewidth decreased therefore down to $\Delta\nu \approx 5$ Hz . Two ions were stored in the trap and prepared into the dark $|\uparrow\rangle$ qubit state inaccessible by the cooling laser followed by a π pulse, for a population transfer into the $|\downarrow\rangle$ state. This measurement was repeated for about 1000 times and the microwave frequency scanned. After each scan the microwave power was reduced by 10 dB and the scan range was diminished around the center frequency. At visible line separation as shown in Figure 17 the Rabi frequency for the next iteration was cross calibrated on one of the centers with existing data for a single ion. For a Rabi time of 150 ms the Zeeman sublevels of both ions were clearly separated with a peak-to-peak distance of down to 70Hz, depending on the trap depth and the first minimum of the sinc^2 function overlapping. By calibration of the ion spacing on the EMCCD and known secular

frequency ω_z, a field gradient of 1 nT/(10 µm) was found along the trap axis for the stored magnetic field at that time [73]. Some examples are shown in Figure 18.

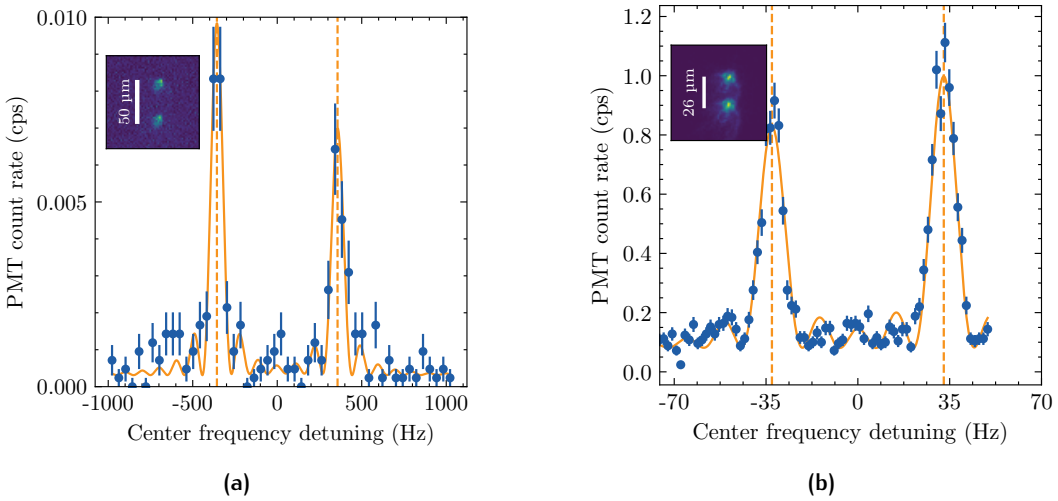

Figure 18: Rabi spectroscopy of two simultaneously stored ions with separations estimated from ion positions on the camera (a) 50 µm and (b) 26 µm. The corresponding Rabi times were (a) 1.5 ms and (b) 150 ms.

4.4 CONCLUSION

In this chapter, the magnetic field properties of the CryPTEx-SC superconducting ion trap were extracted by applying Rabi and Ramsey schemes. As expected from the diamagnetic behavior of superconductors, the magnetic field induced at the phase transition was stored and exhibits a lifetime of about 300 years [73]. Similar features were estimated for nearly perfect superconducting coils [107]. Since the decay is assumed to be dominated by surface resistance, this mean lifetime could be increased if the resonator is operated at lower temperatures. A lower operating temperature would also be beneficial for RF operation of the superconducting quadrupole, as the radial secular frequency is currently limited to about 700 kHz for beryllium ions. While it is still possible to apply anti-Stokes Raman schemes for cooling the ions close to their motional ground state [93], which is a crucial condition for quantum logic spectroscopy, higher secular frequencies are generally more advantageous. Higher frequencies result in stronger confinement, and thus increasing the spacing of the quantum harmonic oscillator states [77].

For this, the resonator's loaded quality factor needs to increase. It was shown that the unloaded quality factor of the resonator depends on the surrounding magnetic field during transiting through the phase transition at cooldown [73]. This effect was

relatively small, on the order of a few percent. Since the magnetic field coils around the trap chamber are comparatively close to the resonator the produced magnetic field is not homogeneous over the entire volume of the resonator and a substantial residual field could have remained, such that the maximum unloaded quality factor might increase with optimized field compensation. A residual magnetic field induces fluxes in volumes containing impurities. Due to the induced RF field, the pinned fluxes experience a Lorentz force and dissipate localized heat, thus decreasing Q_0 [110]. Shielding could be achieved by using high permeability materials, such as permalloy. However, since a null field leads to the quantization axis degeneration of the ions, that option must be rejected.

The redesign of the floating ground in Section 3.3.2 could substantially decrease the thermal resistance and further reduce the operating temperature at similar trap parameters. In combination with an decreased radiative heat load due to the additional copper shields, this solution might become suitable for reaching higher secular frequencies.

Furthermore, the resonator might have formed niobium-hydrides over time due to exposure to air during maintenance works or by chemically reacting with the hydrides inside the bulk materials during slow cooldowns. These impurities cause flux pinning as discussed in the paragraph before. The contamination is reversible, by baking the resonator under vacuum at 900°C for several hours [111]. In the same step, after gas out, the resonator can be doped with nitrogen at low, such that a reformation of hydrides is prevented [112].

By applying Hahn-Spin-Echo schemes a RMS magnetic field noise of 3.5(2)pT was determined [73]. This value was achieved with passive shielding only and was about a factor hundred better than a comparable trap environment [97] with active field noise suppression, and similar to an experiment with static permanent magnets and active residual field noise compensation [109].

Lastly a technique was presented to access single ion qubits by applying weak, 150 ms long π-pulses of microwave radiation, decreasing the Fourier limited linewidth to about 5 Hz. With this technique the magnetic field gradient at that time was determined to be 1 nT/(10 μm). Each of the three coil pairs were connected in series to one power supply, such that this was expected. By using six independent power supplies, the magnetic field can be optimized for a maximum homogeneity in the trap center. For that, the presented technique is suitable, since it allows not only to increase the

Rabi-time by another factor of three, but also to decrease the DC harmonic potential and separate the ions further if required.

5 A CRYOGENIC LENS SYSTEM FOR IMAGING OF BERYLLIUM IONS

State detection of stored ions or atoms is usually achieved by the collection and refocusing of their emitted photons with an optical system onto a charged coupled device or a photo-multiplier tube. In order to maximize photon count rates and reduce aberration contributions, high numerical apertures at short working distances are preferred in most applications [113,114]. With the latest surface electrode-based systems, even integrated fiber optics or electrodes embedded in the optical surface have been used with only a few millimeter distance to the ions [115] to reduce the trap footprint. Even more advanced are on chip superconducting circuits, acting as photon detector [116–118]. Here, biased nano-wires are locally heated by absorbed photons inducing an increased resistance in the material. The number of counted photons is then a function of the bias current leading to quantum efficiencies close to unity [119,120].

If the ion or atom trap is in operation at room temperature, a view port can be positioned right next to it. This increases the alignment flexibility of the optics [121–123] and keeps the working distance small in a range of (20 – 40) mm. For the latest generation of RF ion traps operating in a cryogenic environment, such a view port is not suitable as it increases the black body radiation to which the cryostat is exposed. To overcome this limit, either aspheric [78,124–127], bi-aspheric lenses [97] or reflective objectives [57,128] have been designed to be mounted on up to three-axis piezo stages in vacuum at room temperature or inside a cryostat. With the newest techniques in the ion quantum computing community involving multiple ion species, even multi chromatic refractive systems have entered the stage [123,129].

In particular for cryogenic lenses, thermal effects are not only influencing the design choices of the optical systems, but also their surroundings. Differential thermal expansion coefficients can lead to fatal impacts on a lens. While in the best case, only aberrations occur in the image plane, optical elements tend to break under high, Hertzian contact stresses. Thus, for the optical element mounts, the same diligence needs to be taken as for the optical design. Not only, but mostly in the astronomy community, many approaches have been discussed involving materials with matching or compensating thermal expansion coefficients [130], optimized support surfaces [131], feathered- [132,133], flexure- [132], adhesive mounts [134] or combina-

tions of them [135–139].

In the following chapter, a cryogenic lens system is designed for the new VAUQSI experiment and focuses on maximizing the solid angle to the geometrically limited parameters. In contrast to the CryPTEx-SC experiment, all lenses in vacuum are custom made to increase the optical performance. Furthermore a system in the laboratory environment is presented, which allows for different detectors in individual extensions to meet their resolution limit.

5.0.1 Requirements on the VAUQSI optical system

In the cryogenic Paul trap experiment with a superconducting resonator, the limitations of the lens system are primarily determined by the experimental geometry and the choice of ion species. Due to the shape of the trap electrodes, a maximum numerical aperture of NA = 0.4 can be achieved [72]. Furthermore, the dimensions of the resonator housing result in a minimum working distance of 60 mm to avoid compromising the superconducting environment. As the working distance increases, the dimensions of the lens and cell also rise to diameters larger than 60 mm for the first elements. To maintain space for thermal connections, diagnostics, and wires around the resonator, the maximum diameter of the setup is limited to 100 mm. The design wavelength, $\lambda = 313\,\mathrm{nm}$, corresponds to the ${}^1S_{1/2} \leftrightarrow {}^2P_{3/2}$ transition of beryllium ions. This species is well suited for use as a logic ion in quantum computing experiments, as it allows for easily accessible qubits [140–142] and enables high-precision spectroscopy of highly charged ions [70,71]. This naturally limits the number of available substrate materials, as the cutoff wavelength of most commercially available glasses is between 420 nm and 370 nm. These absorption bands are directly linked to the dispersion of a material, which is particularly related to the bandgap transitions and ionization energies within a lattice.

For a lens in a vacuum, the depth of field is solely related to the wavelength and numerical aperture [143] and is given by:

$$\mathrm{DOF} = \pm\frac{\lambda \cdot \sqrt{1 - \mathrm{NA}^2}}{2\mathrm{NA}^2} \tag{40}$$

resulting in $\mathrm{DOF} \approx 1.8\,\mu\mathrm{m}$. Thus, for optimal performance, the system must be aligned with the ions. The largest objects to be observed with the system are Coulomb crystals measuring 500 µm, which are prepared to re-trap injected highly charged ions [58].

One of the stringent requirements for implementing the optical system was to mini-

mize the increase in thermal input at the 4 K stage due to 300 K blackbody radiation. For the cryogenic system of CryPTEx-SC, radiative heat loads on the order of 2.7 mW have been estimated for the 4 K heat shields [90]. On the other hand, the lid mounted on top of the 40 K stage absorbs about 1 W. By adding a thin circular pinhole on the 40 K stage, surface reflections from an otherwise mounted tube can be neglected, which may otherwise significantly increase the transmitted radiative power in long pipes with the room temperature in the line of sight [144].

In the existing CryPTEx-SC experiment, the realization of the system was achieved by separating both temperature stages of the lens system: The 4 K and 40 K lenses are not mechanically coupled, increasing the degrees of freedom during maintenance. Both temperature stages must be carefully aligned each time the 40 K stage is disassembled and the resonator is moved. While the 4 K and 40 K stages can be referenced to each other, for example with an autocollimator, there is no reference to the trap center. Only after cooldown does the ion point spread function provide direct feedback on whether the blind alignment was successful. Examples of ion images after two maintenance sessions are shown in Figure 19.

Therefore, in the new system, both stages will be mechanically connected to maintain the adjusted positions. This requires a wise choice of materials to minimize heat transfer and maximize the precision of alignment. As a solution, a PEEK holder, presented in Section 5.4.3, was developed. Since the VAUQSI experiment and CryPTEx-SC have identical trap chambers, it is advantageous to retain the dimensions of the intermediate focus and the radii of the top parts of the shields. Consequently, a manipulator for the entire lens stack has been designed, which can be mounted on the 4 K stages of both experiments. This manipulator is described in Section 5.4.4. Since the resonator is floating on an electric potential, mounting the lens system on the 4 K shield requires sufficient insulation from the floating potential to ground. This is achieved by maintaining a distance between the two, allowing for better pumping of the resonator volume, thus improving the quality of its partial pressure. However, one drawback is the increased likelihood of compromising the resonator's Q-factor due to contamination from dust or other macroscopic particles. Therefore, the gap is shielded by a Teflon cylinder. In the following sections, the development process is outlined, and the rationale behind the final set of lens parameters is discussed and optimized.

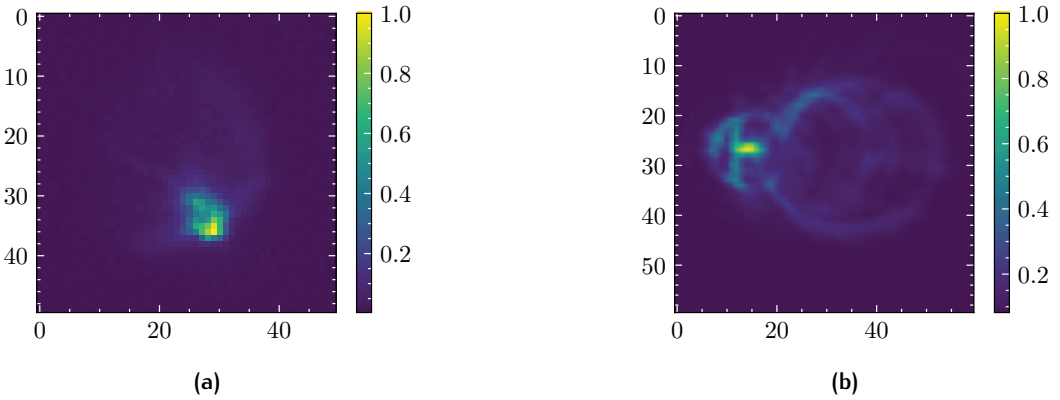

Figure 19: Projection of a single ion on the EMCCD (a) before and (b) after maintenance of the CryPTEx-SC superconducting resonator. Lack of mechanical coupling between the two parts of this optical system and limited possibilities of testing during assembly increases the likelihood of aberrations from misalignment.

5.0.2 Ultraviolet substrates

For wavelengths below 350 nm only a few substrates feature transmission efficiencies > 90%, since the photons obtain energies that excite the electronic band gaps of nearly all molecules. Most used for spherically shaped surfaces are ultraviolet grade fused silica, and diverse fluorides-, like calcium-, magnesium- or lithium fluoride, sapphire, while for thin elements barium fluoride or magnesium oxide are options as well. The crystalline substrates however, often introduce strong birefringence. Due to the similar refraction indices of the first materials mentioned, the chromatic bandwidth is limited to a small range. Investigations into the application of germanium-dioxide as glass were performed. to introduce a thick glass with higher dispersion [145], but seem very limited in use. For cryogenic operation, in particular the first two, SiO_2 and CaF_2 are well characterized and were considered for example for the CryPTex-SC optical system.

DISCLAIMER In this thesis, for modeling reasons of fused silica, the substrate C79-80 of the company Corning was used and is frequently mentioned. This is not an advertisement for this glass or company. There are many other manufacturers of this glass type.

Furthermore, as reference wavelength 313 nm was used. By moving through the nominal simulated focus, it can be shifted to 313.1 nm without introducing significant aberrations.

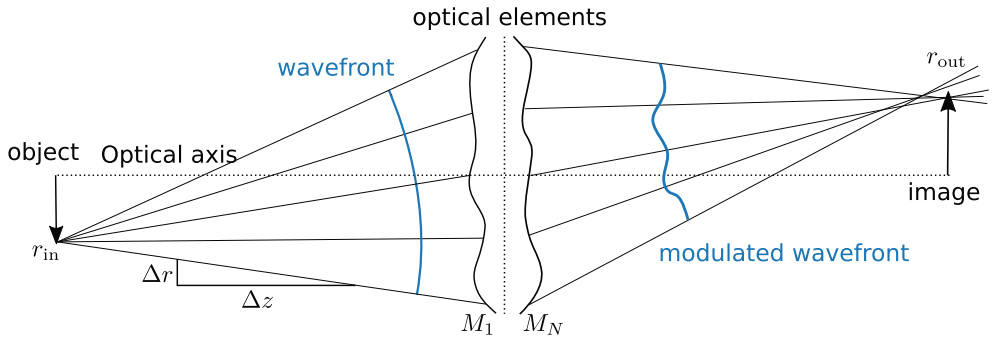

Figure 20: Illustration of both worlds, rays and wavefronts, modulated by optical elements.

All simulations and optimizations were performed with the commercially available Software Zemax Opticstudio.

5.1 IMAGING OF IONS

In optics simulations, light propagation is described by means of rays. The tangent of such a ray is always co-linear to the photon wave vector. For a pararaxial system with small angles, we can approximate $\sin(\theta) \approx \theta$, $\tan(\theta \approx \theta)$ and $\cos\theta \approx 1$. Thus, one can describe the propagation of a ray passing an optical surface by:

$$n_2 \cdot \theta' = n_1\theta + y\frac{n_1 - n_2}{R} \tag{41}$$

Here, n_1 and n_2 are the refraction indices of the initial and final medium, y is the entrance height, θ is the angle with respect to the optical axis and R the radius of curvature of the element. The equation can be rewritten in a matrix formalism, with a ray s and a surface element M_i as sketched in A.1. This is however, even in the paraxial approximation, not the full picture of a lens system, and raises different errors when a ray is propagated through many surfaces. For example, the inception point at each element is a flat plane, not a curved surface. Thus, in common algorithms, ray tracing is usually performed by applying the full Snell law and calculating each intersection point. Still, more general, all methods try to minimize a system of surfaces which is of the form

$$\begin{pmatrix} r_{\text{out}} \\ r'_{\text{out}} \end{pmatrix} = \prod_{i=N}^{1} M_i \begin{pmatrix} r_{\text{in}} \\ r'_{\text{in}} \end{pmatrix} = \begin{pmatrix} A_{\text{tot}}\, r_{\text{in}} + B_{\text{tot}}\, r'_{\text{in}} \\ C_{\text{tot}}\, r_{\text{in}} + D_{\text{tot}}\, r'_{\text{in}} \end{pmatrix} \tag{42}$$

Here, still in two dimensions, r denoted the height of a ray to the optical axis at the optical axis location z and $r' = \partial r/\partial z$. To form an image, the system needs to be optimized, that $B_{\text{tot}} = 0$. For both, spherical and free form systems, analytical solutions are well known [143] and can be transferred to off-axis elements.

A more sophisticated way of describing an optical system for physicists, is a description of the light path through the optical system between two points $r_{in} = (x_0, y_0, z_0)$ and $r_{out} = (x_1, y_1, z_1)$ by applying Fermat's law and following [146]:

$$V(x_0, y_0; x_1, y_1; z_0, z_1) = \int L(x, y, \dot{x}, \dot{y}) dz \tag{43}$$

with the Lagrangian

$$L = n\sqrt{\dot{x}^2 + \dot{y}^2 + 1} \tag{44}$$

where $\dot{x} = \partial x/\partial z$ and $\dot{y} = \partial y/\partial z$ is equivalent to the expression before. With the operators

$$\hat{p}_x = -i\frac{\lambda}{2\pi}\frac{\partial}{\partial x},\ \hat{p}_y = -i\frac{\lambda}{2\pi}\frac{\partial}{\partial y} \text{ and } \hat{H} = i\frac{\lambda}{2\pi}\frac{\partial}{\partial z} \tag{45}$$

one retrieves after some steps the Helmholtz equation describing a wave propagation through space

$$\left[\frac{\partial^2}{\partial x^2} + \frac{\partial^2}{\partial y^2} + \frac{\partial^2}{\partial z^2} + n^2\left(\frac{2\pi}{\lambda}\right)\right] U = \Delta U + n^2 \kappa_0 U \tag{46}$$

where U is denoted as the amplitude in the image space, equivalent to an electric field. For a wave passing through a pupil, the modulation in the image plane can be described by [146]

$$U(r, \theta) = \left(\frac{1}{\lambda}\right)^2 e^{-ik(p\cdot x + q\cdot y)} \int_0^{2\pi} \int_{\rho=0}^{1} e^{ik_0 \cdot NA \cdot r \cdot \rho' \cos(\theta - \phi)} \rho' d\rho' d\phi \tag{47}$$

where p_c and q_c are rays pointing from the object to the pupil center, often referred to as chief rays. For a circular aperture, one finds after evaluating the integral:

$$U(r) = \frac{NA}{r\lambda} J_1\left(2\pi r \frac{NA}{\lambda}\right) \tag{48}$$

where $J_1(x)$ is the Bessel function. The intensity distribution in the image plane is then given by [146]

$$I_{\text{PSF}} = \left(\frac{J_1(2\pi w)}{\pi w}\right)^2 \tag{49}$$

where $w = rNA/\lambda$. This intensity function is often referred to as point-spread function PSF, which can however be modulated by imperfections of the imaging system. Often used as reference to quantify energy dissipation, by integrating the intensity profile along r yields the encircled energy $E_{\text{circ}}(r) = 2\pi \int_0^r I(r)\, r dr$. In the ideal imaging condition, the well known Abbe criterion is retrieved in the first minimum of the so called Airy disk in Function 49

$$r_o = 1.22\frac{\lambda}{2NA} \tag{50}$$

For this spot, the encircled energy is $E_{\mathrm{circ}}(r_0)/E_{\mathrm{circ}}(r_{\mathrm{max}}) = 83.6\%$. By assuming a general amplitude $A(p,q)$ and pupil $P(p,q)$ function we can furthermore estimate the impact of imperfections in the imaging path

$$U(x,t) = \left(\frac{1}{\lambda}\right)^2 e \int_{p_1} \int_{q_1} A(p,q)P(p,q)e^{ik_0\left[W(x_0,y_0;p,q)\right]}\,dpdq \tag{51}$$

By Taylor expansion of the phase and normalizing the resulting intensity term, one finds

$$I_n(0) \approx 1 + k_0^2\bar{W}^2 - k_0^2\bar{W}^2 = 1 - k_0^2(\Delta W)^2 \tag{52}$$

This intensity distribution is called Strehl condition. ΔW is denoted as the root-mean-square deviation of the passing wavefront W. If the RMS wavefront error is increasing, the energy dissipates along r, resulting in a loss in contrast. At low intensities, where only (10 – 20) photons are detected, large RMS values thus can diminish the signal-to-noise ratio, that in worst case no signal can be retrieved. By applying the Maréchal criterion, the maximum wave-front error allowed is

$$\mathrm{RMS}(W) = \Delta W \leq \frac{\lambda}{14} \tag{53}$$

A description of the wave-front error can be achieved by expanding the polynomial into a power series

$$W(x_0,y_0;p_1,q_1) = \sum_{n,m,k,l} A_{nmkl}\, x_0^n\, y_0^m\, p_1^k\, q_1^l \tag{54}$$

with an order term $O = n + m + k + l$. Often, even powers are related to design errors contributed by the radial wavefront error induced by spherical surfaces, and odd numbers are referred to fabrication errors in the optical system, such as tilts and decentration [146]. The wavefront has usually non-linear properties if the reference point is far from the imaging axis. Thus, it should be evaluated at different field heights. In rotationally symmetric geometries without central obscuration, an often used set of functions are the Zernike polynomials, which are circular and orthogonal.

$$\begin{aligned} W(x_0;\rho,\phi) &= \sum_{n=0}^{m=0} C_{n,m}(x_0)R_n^m(\rho)e^{im\phi} \\ &= \sum_{n=0}^{\infty}\sum_{m=0}^{n} A_{m,n}(x_0)R_n^m(\rho)\cos(m\phi) + \sum_{n=0}^{\infty}\sum_{m=0}^{n} A'_{n,m}(x_0)R_n^m(\rho)\sin(m\phi) \end{aligned} \tag{55}$$

where $m \geq 0$, $n \geqslant |m|$, $(n - |m|) \mod 2 = 0$ and $n, m \in \mathbb{Z}$. For the radial part, the polynomials are given by

$$R_n^m(\rho) = \sum_{s=0}^{(n-m)/2} (-1)^s \frac{(n-s)!}{s!(\frac{n+m}{2}-s)!(\frac{n-m}{2}-s)!}\rho^{n-2s}\,. \tag{56}$$

Zernike polynomials are widely used to quantify the wavefront error of optics systems by fitting them to experimentally retrieved wavefronts. Other polynomials exist

if faster algorithms are required, for example in adaptive optics experiments where a kilohertz response frequency is required [147, 148]. Furthermore, abbreviations and generalization that account for example for obscuration or other pupil shapes do exist [146, 149]. By calculating the ninth Zernike term, one finds

$$Z_9 = c_9(6\rho^4 - 6\rho^2 + 1) \tag{57}$$

This term is referred to as fourth order spherical aberrations and in longitudinal direction they scale [146]

$$l(\rho) = -\frac{\sqrt{1-\rho^2}}{\rho NA^2}\frac{\partial W}{\partial \rho} = -24\sqrt{1-\rho^2 NA^2}\frac{\rho^2}{NA^2}c_9 \tag{58}$$

The behavior is shown in Figure 21a. To address spherical aberrations, one can optimize for either multiple lenses or modification of the surface shape of the current lens. Incorporating aspheric parameters into the system enables compensation for spherical aberrations up to the nth order. A prevalent representation of an aspheric lens surface profile frequently adopts the form of a superimposed Taylor expansion in z:

$$z(r) = \frac{r^2}{R\left(1+\sqrt{1-(1+\kappa)\frac{r^2}{R^2}}\right)} + \sum_{i=2}^{n} \alpha_{2i}\, r^{2i} \tag{59}$$

Within this equation, κ describes the conic constant and α_i define the radial surface deviations at given orders. The aspheric lens shape $z = a_j r^j$ can be scaled $(z, y) \rightarrow (mz, my)$ by utilizing $b_j = a_j / m^{j-1}$ with scaling factor m. In Figure 21c, the spherical lens with diameter D and center thickness $t = D/3$, was modified for $\lambda = 313\,\text{nm}$, $n = 1.48441$, aperture $f/1.25$ and a backfocal distance of $f_b = D$. In comparison to the spherical lens, the radius of curvature slightly changed, this is probably due to the second term in the fourth order spherical aberrations (Equation 57).

While spherical errors in the wavefront are compensated by optimized aspheric surfaces, other wavefront errors are introduced, due to the asymmetric profile for rays starting at of-axis objects. One example is given in Figure 22, where coma is introduced by focusing an off-axis beam. Only by introducing a second aspheric surface most mentioned aberrations can be compensated [146].

5.2 CRYOGENIC IMAGING SYSTEMS

Due to the vast number of publications on ion trap experiments, by now many concepts had been developed, most for systems at room temperature. On the lower side of the temperature, in particular for space mission, cryogenic optics with ultra-stable mounts were developed over the last decades. In this section, a variety of solutions

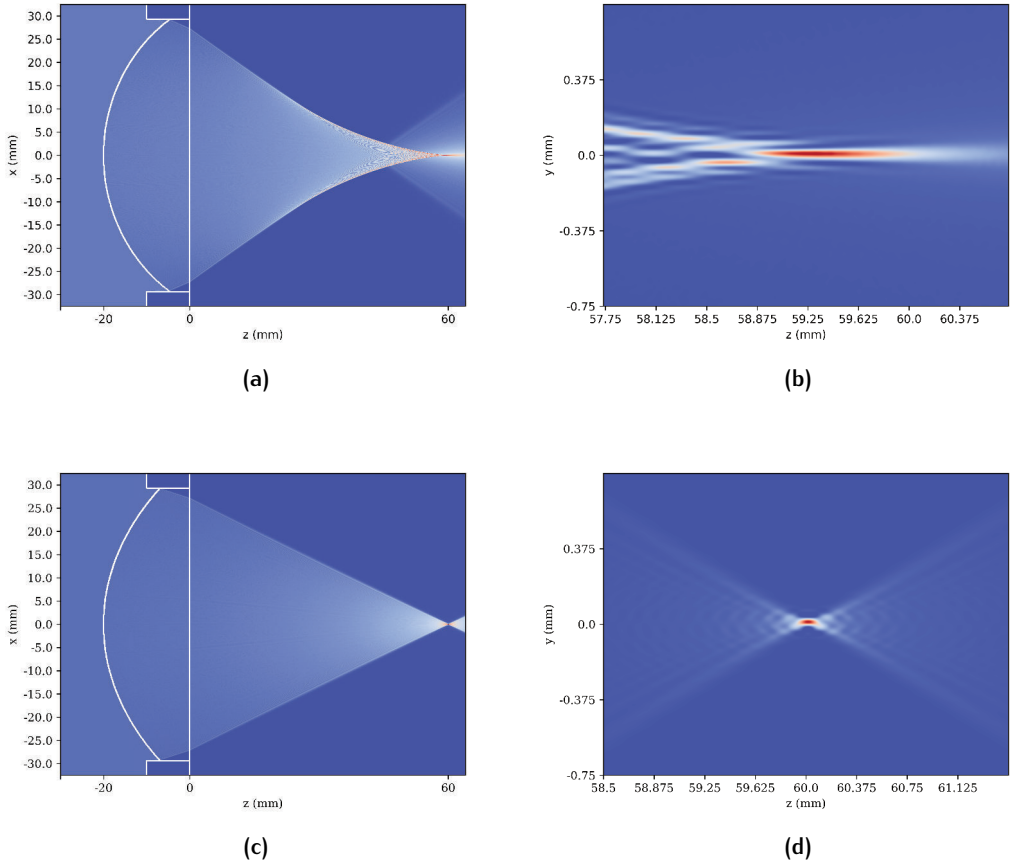

Figure 21: (a) Plano-convex lens with diffraction coefficient $n = 1.48441$, diameter $d = 60\,\text{mm}$, curvature $c = 1/35\,\text{mm}$ at wavelength $\lambda = 313\,\text{nm}$, aperture NA= 0.4 and back focal length $f = 60\,\text{mm}$. One can clearly see the induced spherical aberrations around the focus. (b) Zoom in the focus region of image (a). (c) Optimized lens with parameters from (a). The surface shape is now corresponding to 59. For that, the curvature was modified to $c = 1/35.591\,\text{mm}$ and a conic constant $\kappa = -0.31971$ was introduced as well as even aspheric coefficients up to the eighth order. (d) Focus region of the lens shown in (c). in comparison to the plano-convex lens, the light is now evenly converging into much smaller spot. Simulated with [150].

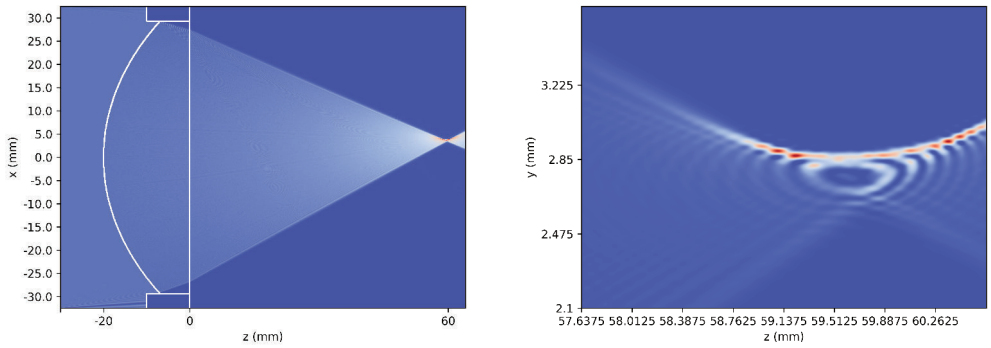

(a) (b)

Figure 22: (a)The same plano-aspheric lens as shown in Figure 21c, but with an angle of the incoming plane light wave. Simulated with [150]

Table 3: Boundaries of the cryogenic Paul trap experiment.

Primary wavelength	313 nm
Working distance	$\leq$ 60 mm
Magnification	$\approx 30x$
Object space NA	0.4
Object field of view diameter	500 µm

for cryogenic imaging objectives based on the geometry requirements of the resonator and trap chamber are presented and discussed. First, achromatic systems will be addressed. Second, monochromatic objectives are introduced. Third, the VAUQSI experiment solution is presented which purely relies on a set of lenses inside the cryogenic environment. All systems were optimized for the following conditions as shown in Table 3.

5.2.1 On the thermal expansion of materials

In the literature, the volumetric coefficient of expansion or contraction of a material as a function of temperature is given by:

$$\alpha_V = \frac{1}{V}\left(\frac{dV}{dT}\right)_p \tag{60}$$

For most materials α_V is positive, indicating that, under constant pressure, an increase in temperature leads to an increase in body volume. Since most solid materials are nearly incompressible, in first order a linear coefficient of expansion is commonly defined:

Table 4: Thermal expansion integrals of technical materials for cryogenic temperatures from 293 K and coefficient at room temperature of relevant materials. The values have to be multiplied by a factor 10^{-4}. If not marked otherwise, taken from [91]

Material	$-\Delta L/L$ 4 K	$-\Delta L/L$ 40 K	$-\Delta L/L$ 80 K	$-\Delta L/L$ 100 K	$-\Delta L/L$ 150 K	$-\Delta L/L$ 200 K	$-\Delta L/L$ 250 K	α 293 K
Al	41.4	41.2	39.0	36.0	29.4	20.1	9.6	18.5
Cu	32.6	32.3	30.2	28.3	22.1	14.9	7.1	16.65
Nb	14.3	14.1	12.9	12.1	9.3	6.3	3.0	7.1
Si	2.2	2.2	2.3	2.4	2.4	1.9	1.0	2.56
Ti	15.1	15.0	14.2	13.4	10.7	7.3	3.5	8.6
Al 2024 [151]	39.6	39.4	37.2	35.1	27.8	19.0	9.0	21.2
Al 5083 [151]	41.5	41.3	39.0	36.8	29.4	20.1	9.7	22.8
brass (65/35)	38.4	38.0	35.0	32.6	25.3	16.9	8.0	19.0
brass(70/30)	36.9	36.6	33.7	31.3	24.5	16.3	7.5	18
$Fe_{64}Ni_{36}$	4.5	4.8	4.8	4.5	3.0	2.0	0.9	1
$Fe_{58}Ni_{42}$	5.4	5.4	5.2	4.9	3.9	2.5	1.3	0.2
S.S.304/306	29.7	29.6	27.8	26.0	20.3	13.8	6.6	15.8
Ti-6Al-4V	17.3	17.1	16.2	15.4	11.8	7.8	3.6	8
sapphire($\parallel$)	7.15	7.15	7.05	6.9	6.1	4.5	2.3	5.80
sapphire($\perp$)	6.05	6.05	5.95	5.85	5.2	3.9	2.0	5.06
silica [152]	-0.51	-0.31	-0.004	0.13	0.3	0.31	0.2	0.03
CaF_2 [153]	30.8	30.7	29.6	28.4	23.3	16.2	1.3	18.5

$$\alpha = \frac{1}{L}\frac{dL}{dT} \tag{61}$$

In many common metals $\Delta L/L = \alpha(T) \cdot \Delta T$ is linearly dependent on T around 300 K and at low temperatures proportional to T^4. In Table 4 the thermal expansion integrals of important materials are listed.

By incorporating 186 mm long stainless steel spokes with a diameter of 2 mm as used in CryPTEx-SC, which mechanically connect two cylindrically shaped cryogenic stages operating at 40 K and 4 K in a radial arrangement, we can estimate a length reduction of approximately 0.55 mm when cooling from room temperature to operational conditions. At first glance, the stress on the spokes appears to increase due to this reduced length. However, it is important to note that the frames of both heat shields are constructed from copper, which experiences a shrinkage of about $-\Delta L \approx 0.61$ mm. This shrinking results in a decrease in tension on the spokes during the cooldown process. Although the changes in force for this example are relatively

small - on the order of about one newton - more sensitive components in a cryogenic setup may experience performance degradation or even damage if thermal expansion properties are not adequately accounted for.

One such sensitive element is glass. For example, consider a 66 mm diameter fused silica lens with a convex radius of 248 mm and an edge thickness of 5 mm, mounted in an aluminum barrel (Al 5083). To ensure precise alignment and keep the maximum offset from the optical axis to less than 120 arcsec, the inner barrel diameter must be toleranced to 66.05 mm [154]. Upon cooling this setup down to 4 K, the aluminum barrel will contract by approximately 0.275 mm, thereby applying a radial pressure given by $p = \Delta r \cdot \hat{E} \cdot (r_o - r_i)/(r_i) = 0.69\,\text{MPa}$ on the lens. Here

$$\hat{E} = \frac{1}{\frac{\left(1-\nu_{\text{Al}}^2\right)}{E_{\text{Al}}} + \frac{\left(1-\nu_{\text{FS}}^2\right)}{E_{\text{FS}}}} \tag{62}$$

where E_i and ν_i denote the Young's modulus and Poisson's ratios of each material, respectively. While the resulting stress is a small fraction of the fracture limit, it can induce bending of the lens on the order of ten microns, potentially leading to significant optical aberrations.

Not all materials shrink when cooled down. In particular fused-silica expands below 200 K. Other materials, like some titanium or nickel alloys do obtain a negative thermal expansion coefficient in one spacial direction, while shrinking in the other [155]. Thus, by utilizing this axis and optimizing for the required dimensions, the material can compensate the shrinking of standard materials [156]. On the other side, for thermal connections where constant pressure contacts are required, washers can improve performances.

Besides thermal expansion, of course physical quantities like stiffness, thermal and electrical conductivity, heat capacity, diffraction behavior do depend on the microscopic characteristics of each material. Furthermore, manufacturing characteristics, impurities, aging, follow-up treatments change the material behavior. An in depth discussion is given for example in [91, 157, 158].

In this thesis, the focus was pointed on fused silica as lens substrate. Fortunately, over the last decades many measurement results had been published on fused silica/quartz [152, 159, 160]. By considering not only the expansion integral from 300 K to 4 K, but also the function of each substrate and comparing it to their respective mounting materials, one in addition avoids stress peaks, which might become fatal during cooldown/warm up cycles.

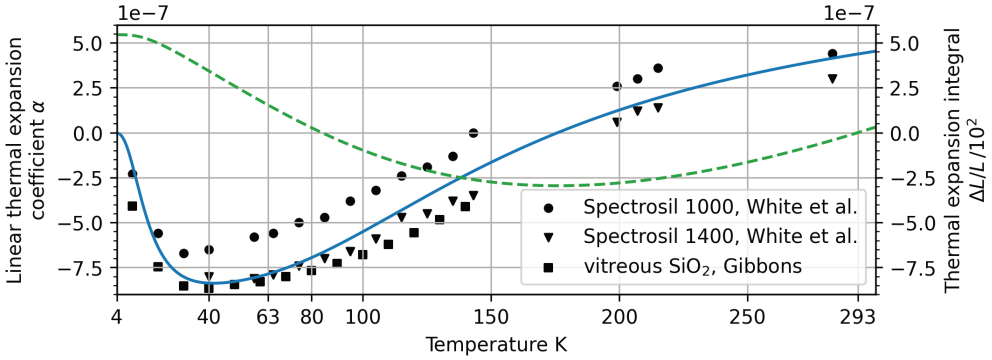

(a)

Figure 23: Fused silica linear expansion coefficients (solid line) and integrated thermal expansion (dashed line) for low temperatures. The empiric model was taken from [152]. In addition the linear thermal coefficients of similar materials are plotted [159, 160].

FUSED SILICA Fused silica does obtain a negative expansion coefficient below 160 K. Okaji et al. measured vitreous silica reference glass from 273 K down to 6 K [152]. The compiled plots from their work are shown in Figure 23.Their fitted linear temperature coefficient formula is given by:

$$\alpha\,(T)\,\mathrm{K}^{-1} = \left[a \cdot (b/T)^c \frac{\exp(b/T)}{(\exp(b/T)+1)^2} + d \cdot (e/T)^2 \frac{\exp(e/T)}{(\exp(e/T)-1)^2}\right] \cdot 10^{-6} \qquad (63)$$

with $a = -4.22$, $b = 35.5$, $c = 0.335$, $d = 1.253$ and $e = 5.35$ [152]. In addition, linear expansion coefficients of similar materials are plotted for comparison [159, 160]. One easily recognizes offsets between the materials. This is a well known feature due to the manufacturing processes of the glasses [161]. The reference glass of [152] was referred as a Type-I fused quartz, which was molten from a crystal in an electric furnace, while the glasses from [159] were synthetically manufactured fused silica. An extended discussion on thermal expansion coefficients for different types of silica and their data interpretation is given in [162]. A change in volume does have an impact on the surface shapes of each lens. Precision quality lenses are toleranced $\Delta d = \pm 0.05$ mm in diameter and the radius of curvature $\Delta r/r = \pm 0.05\%$. As a consequence, a system aiming for optimized imaging performance is required to be aligned for operation conditions at room temperature, if the thermal expansion integral is not negligible. In CryPTEx-SC, the lens objective consisted of UVFS as well as CaF_2 lenses. Let's do a thought experiment on the influence on the thermally induced error: A plano convex CaF_2 lens with 63.5 mm diameter, 13.7 mm thickness and 44 mm curvature radius is cooled down from room temperature to 4 K. Given the substrate CaF_2 which holds an integrated length change of $(L_{293\,\mathrm{K}} - L_{4\,\mathrm{K}})/L = 0.308\%$, this is a factor five larger, than the tolerated error on the surface curvature and in the order of magnitude of the thickness manufacturing error.

5.2.2 Temperature dependent refractive indices

In the case of fused silica, at 20 °C the dispersion relation is given by [163]

$$n^2 - 1 = \frac{0.6961663\lambda^2}{\lambda^2 - (0.0684043)^2} + \frac{0.4079426\lambda^2}{\lambda^2 - (0.1162414)^2} + \frac{0.8974794\lambda^2}{\lambda^2 - (9.896161)^2} \tag{64}$$

This equation is the standard for most optics design applications. For strongly abbreviating temperatures and optical systems with high numerical aperture or long light paths, an error in the design is induced, which possibly decreases the imaging quality by shifting the focus and increasing dispersion dependent aberrations. To overcome this limit and provide accurate data for cryogenic optical instruments, a variety of experiments were presented in the past, including etalons [162, 164], Fizeau interferometers and refractometers [165], reaching measurement uncertainties of $\delta n/n = 2 \times 10^{-6}$. In the presence of large temperature changes, the dispersion relation can be described by:

$$n^2 - 1 = \sum_{i=1}^{3} \frac{B_i(\lambda, T)\lambda^2}{\lambda^2 - \lambda_i^2(T)} \tag{65}$$

with the coefficients

$$B_i(T) = \sum_{j=0}^{4} B_{ij} \cdot T^j \tag{66}$$

and

$$\lambda_i(T) = \sum_{j=0}^{4} \lambda_{ij} \cdot T^j \tag{67}$$

Refractive indices for fused silica were experimentally retrieved by Leviton et al. for temperatures down to 30 K and in a wavelength range from 400 nm to 2.6 µm [165]. Outside the given range, the fitted model, however, features large gradients, in particular around 340 nm a in the refractive index of ≈ 3 % is present. As a second model, data from Matsuoka et al. [166] was compared with the first mentioned. That one only contained temperature coefficients up to T^2. However it obtained a continuous behavior over the full temperature and yield a refractive index of $n_{4\,\mathrm{K}} = 1.483055$ and $n_{40\,\mathrm{K}} = 1.48310$ for fused silica at 313 nm, compared to $n_{300\,\mathrm{K}} = 1.4844$.

5.2.3 Cryogenic lens mounts

As previously discussed, differential thermal expansion is one of the most threatening features in low temperature optics assemblies, since it mostly limits the achievable alignment strategies and can reduce the imaging quality tremendously, if the substrate geometry changes due to stress. An intuitive way to counteract stress induced by mounts on substrates is a matching thermal expansion coefficient for the lens cell material. For CaF2, copper or beryllium-copper are good candidates. On

the other hand, for fused silica substrates, iron-nickel alloys do obtain the lowest available expansion integrals. In particular systems with only two elements can be optically connected to mounting parts of the same material [167].

For matching integrals and similar thermal expansion coefficients over the full temperature cycle, conventional mounts with sharp corners or tangent/spherical contact seats and preloads applied by retaining rings are suitable if the torque is controlled. By replacing the ring with a spring element, the induced tension can be further reduced during cooldown.

5.3 REFLECTIVE SYSTEMS FOR IMAGING MULTIPLE ION SPECIES

In this section, a set of solutions for imaging at long working distances are presented with a focus on reflective systems. These are of interest, since they offer achromatic properties. In the ion trapping community, an increasing number of groups investigate on frequency standards based on multiple ions being axially aligned and interrogated in a single trap. For such arrangements, a single cooling/readout ion is insufficient since their respective coupling decreases. Thus larger values for the field-of-view are required.

For reflective surfaces, aluminum broadband coatings down to UV-wavelengths are available, covering a reflectivity of about 85% per surface. Some groups have reported to add a layer of silicon on top to prevent a degradation of the aluminum [168]. On the other hand, anti-reflective magnesium fluoride coatings cover the transmitting surfaces and only reflect about 0.6% in the UV.

Achromatic refractive systems: Schwarzschild mirrors

The simplest analytical solution for an achromatic, high NA system is an objective with two confocal, reflecting surfaces. Such a purely spherical mirror-set had been calculated and optimized for third order aberrations by Karl Schwarzschild in 1905 [169] and was utilized for soft x-ray fusion research, bio-sciences and laboratory astrophysics in the past [170,171]. In the optical regime, an application for cryogenic ion traps was reported multiple times as well [128,167,172]. In Figure 24 the required geometric parameters for a Schwarzschild microscope with primary- and secondary mirror as well as finite back-focus is shown. A working distance of $s \leq 65\,\mathrm{mm}$ is

required to be able to place the secondary mirror substrate outside the RFQ. The classic, aplanatic Schwarzschild condition for a confocal system is given by [170]:

$$\frac{R_1}{R_2} = 1.5 - \frac{R_2}{Z_O} \pm \sqrt{1.25 - \frac{R_2}{Z_O}} \tag{68}$$

with $Z_O = S - R_2$ representing the distance between focus of both mirrors and the object. Furthermore, one easily finds the mirror distance $d = R_1 - R_2$ and $Z = Z_i - R_1$ between the image plane and primary mirror. With theses parameters, one finds the optics dimensions in length and dependence on the working distance. In Table 5 the final values for a refractive imaging system with $30x$ magnification are presented. Further discussions on optimization of such a system is presented in [173]. The image is formed about $z = 780\,\text{mm}$ behind the primary mirror. Due to the secondary mirror dimensions, about 28% of the emitted light is cut off due to obscuration, excluding the mounting arm portions. The obscuration naturally decreases the modulation of the optical transfer function in the mid-frequency regime and transfers the energy in the image plane out of the central maximum onto the first and second rings of the airy disk. Furthermore obscuration induces aberrations like astigmatism. Thus, 80% of the light is encircled on a plane of 100µm on the camera. Due to the reflective surface, a constant RMS spot size of 16 µm could be achieved on a 250 µm field height, which is just at the diffraction limited spot size of 14 µm. Due to the transfer of energy into the first and second airy ring, the Strehl ratio of the PSF extracted by wave propagation through the optical system particularly drops for off-axis sources to ≈ 0.65 at Be^+ wavelength adding the necessity for enhanced alignment methods on all three axises. Furthermore, both mirrors are ideally required to be precisely pre-aligned with an interferometer and optically connected [167]. A lithium-aluminosilicate glass-ceramic substrate like Zerodur obtains a expansion integral $\Delta L/L = 7.1 \cdot 10^{-5}$ [174] from 300 K to 4 K. Thus the distance between both mirrors needs to be adjusted for cryogenic operating temperatures with a tight tolerance of a micron or a set of piezo crystals for realization of an equidistant positioning between 300 K an 4 K. To reach the nominal specifications, the peak-to valley wavefront error of both surfaces needs to be smaller than $W_{P-V} = \lambda/4 \approx 78\,\text{nm}$, thus the error budget of each surface is $W_{P-V}/\sqrt{(2)}$. To mount the secondary mirror, either multiple arms or a single piece of fused silica can be used. Both naturally introduce obscuration and modulate the incoming light wavefront.

Catadioptric systems

To simplifiy the mounting procedure of the secondary Mirror in a Schwarzschild-like configuration, it is possible to exchange the secondary mirror with a lens that has an outer transmitting and inner reflecting surface. For high NA, such a system

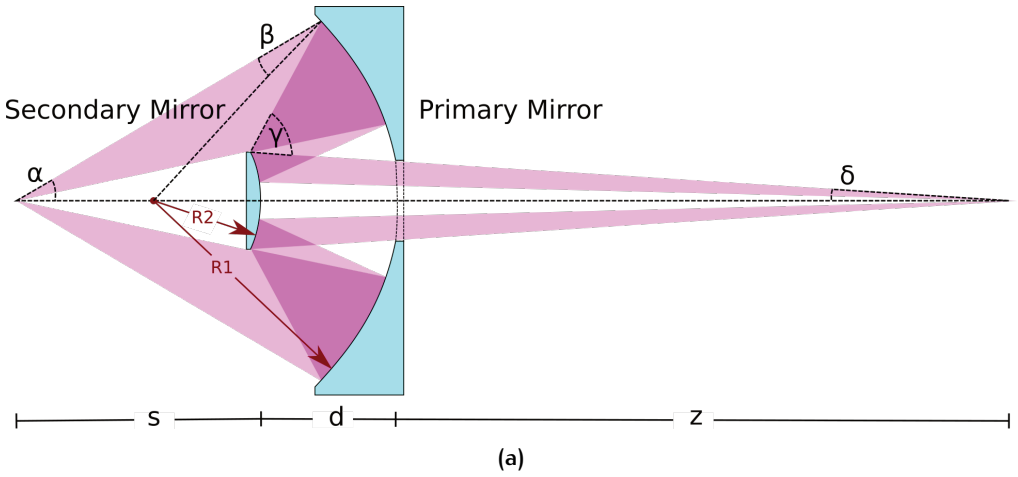

Figure 24: Schematic overview of an Schwarzschild-type reflective objective with working distance s and backfocus z. The spacing between both surfaces is given by d. If the system is called confocal, the center points of the curvatures overlap.

Table 5: Parameters for a co-radial Schwarzschild-type imaging system with NA=0.4, 65.0 mm working distance and 30x magnification at an obscuration of 27%. 126.84 mm are separating the primary mirror and object. The elements can be manufactured of UVFS or any low thermal expansion material like Zerodur. Both surfaces are spherical and the system is fully achromatic with a maximum geometric spot diameter of 47.42 µm at 250 µm field height

Element	Surface	Radius /mm	Thickness /mm	Diameter /mm
S1	1 (r)	-97.645	-61.843	102
S2	2 (r)	-35.802	841.08	25

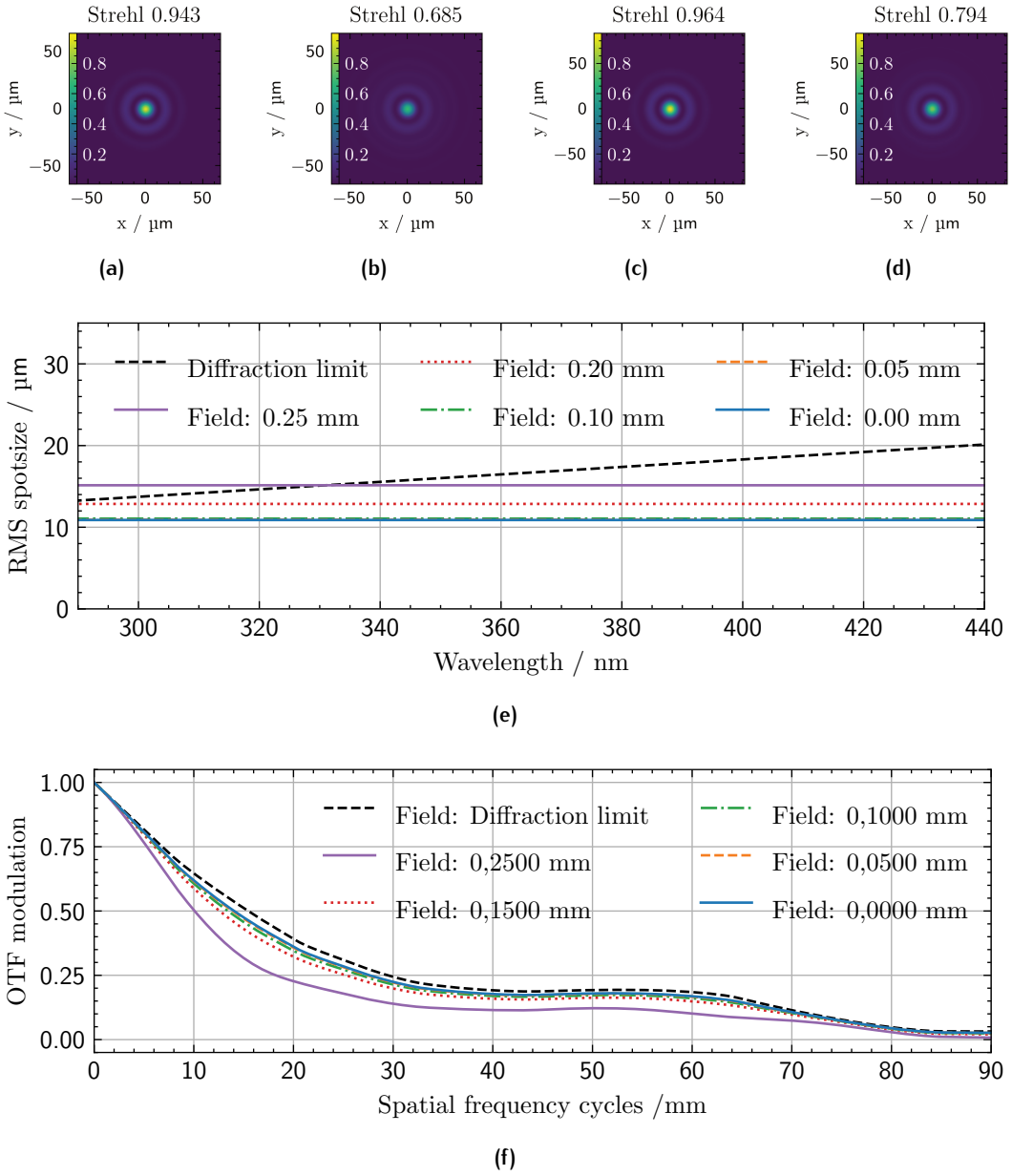

Figure 25: (a,b) simulated point spread functions for Be^+ at 313 nm wavelength on-axis (a) and at a field height of 250 µm (b). (c,d) The same for Ca^+ at 397 nm. (e) RMS spot size diagram over the wavelength range (290 – 440)nm. The blue line indicates the on-axis field. Due to the usage of only reflective elements, the spot size stays constant over the full spectrum. If the optimized wavelengths spread further, they bandwidth of the shorter wavelength decreases. (f) Modulation transfer function in the focus for Be^+ at different fields.

can only optimized for a single wavelength; however, in particular for telescopes, third order aberrations can be corrected over the full optical spectral range [175]. Additionally, by incorporating meniscus lenses of different substrates, like CaF_2 or GeO_2, as correction elements, it was shown, that achromatic deep ultraviolet systems can achieve a higher spectral bandwidth [176]. For Be^+ and Mg^+ detection, a composite system has been reported to perform at the diffraction limit [129].

One drawback of a system containing CaF_2 is its high thermal expansion integral from 300 K to 4 K, which induces changes in curvature and consequently shifts the spectral bandwidth of the system. Thus, this work focuses on a system with a single substrate material, UVFS (SiO_2). Correction for spherical and chromatic aberration can be achieved by utilizing two Mangin mirrors [177,178]. In this configuration, the light first enters a concave substrate and is then reflected back. A schematic overview of this configuration is shown in Figure 26.

In this work, the concept presented by Webb is extended to provide an optimized focus for a pair of wavelengths, 313 nm and 397 nm, corresponding to Be^+ and Ca^+ . This pair was chosen arbitrarily but resulted in a diffraction-limited spectrum between the two desired wavelengths. As the wavelength spacing increases, particularly into the deeper ultraviolet regime, the bandwidth of the lower wavelength decreases dramatically, while for higher wavelengths, it stays constant. How ever, the minimum spot size asymptotically approaches the upper bound of the diffraction limit. Furthermore, the performance also rapidly decreases in the spectrum between the design wavelengths. To compensate for this or to achieve higher NA values, one or more lenses can be added between the Mangin mirrors [176]. An example for a NA= 0.4 system is given in the Appendix A.6, for a wavelength pair 230 nm and 369.5 nm, corresponding to the cooling transition of indium and ytterbium ions, respectively.

Table 6 presents the resulting surface parameters. Due to the conical shape of the second mirror surface $R5$, the obscuration of the system is reduced, resulting in a theoretical transmission of 87.5%. Consequently, the calculated modulation transfer function, shown in Figure 27 for the full field at a wavelength of 313 nm, more closely follows the diffraction-limited cut-off behavior of $1/\lambda$ for a simple circular aperture, compared to the Schwarzschild objective. The nominal peak-to-valley error in the focus is $W_{\mathrm{PV}} = \lambda/10$. Thus, the point spread function converges to an airy disk with a Strehl ratio of 0.967 over the full 500 µm field of view.

With a footprint of about 75 mm in length and a maximum diameter of 100 mm for

Table 6: Parameters for a catadioptric imaging system with NA=0.4, $S = 61.462\,\text{mm}$ working distance and 30x magnification. All elements are made of Corning 79-80 UVFS. Only surface 9 does have a conic constant $\kappa = 0.554$. The system is optimized for two wavelengths, $\lambda_1 = 313\,\text{nm}$ and $\lambda_2 = 397\,\text{nm}$ corresponding to Be^+ , Ca^+ , while the spectrum between is projecting a diffraction limited spotsize as well, enabling imaging of Yb^+ .

Element	Surface	Radius /mm	Thickness /mm	Diameter /mm
S1	3 (R1)	-112.86	22.000	54.50
S1	4 (R2)	-55.25	21.170	66.50
S2	5 (R3)	-59.00	30.000	76.00
S2	6 (R4,r)	-102.35	-72.070	100.00
S1	9 (R5,r,c)	-25.34	596.086	18.00

the primary mirror *S*2, such a system would fit into the 4 K stage. The lens geometries were chosen such that the edge thicknesses are larger than 10 mm, allowing for the application of adhesive bonding techniques, which result in simpler mounting and alignment schemes as well as optimized thermal conduction. The beam leaving the objective is 20 mm wide and reaches the focal plane at a distance of $z = 596\,\text{mm}$ with respect to the objective. Since the numerical aperture of the back focus is extremely low, the impact of the vacuum window on chromatic aberrations can be neglected. For the desired wavelength spectrum, standard wideband anti-reflection coatings in combination with UV-enhanced aluminum reflection coatings can be applied [168, 179]. When comparing the Schwarzschild mirror to the catadioptric design set, drawbacks regarding manufacturing tolerances in the latter become apparent. Due to the shorter wavelength propagating inside the material, the reflective surfaces are more sensitive to fabrication tolerances, as the allowed error scales with the refractive index $(1/n)$, resulting in required accuracies within a few 10 nm for one surface. This increases the cost for such a system and introduces complexities in lens metrology. While spherical surfaces can be probed by interferometric measurements at that precision, the conic surface, along with the whole assembly, could be tested using a diffractive null lens element, as previously demonstrated for the EUCLID satellite mission [180].

Achromatic Systems: Monolithic mirror on 4K

By reducing the number of substrates to a single element, a change of the alignment during temperature cycles can be avoided and only the substrate itself needs to be considered in simulations or calculations. A single component catadioptric system can be utilized for light collection independent of the wavelength [168, 179, 181]. All reported systems were designed to perform in cryogenic environments and at least

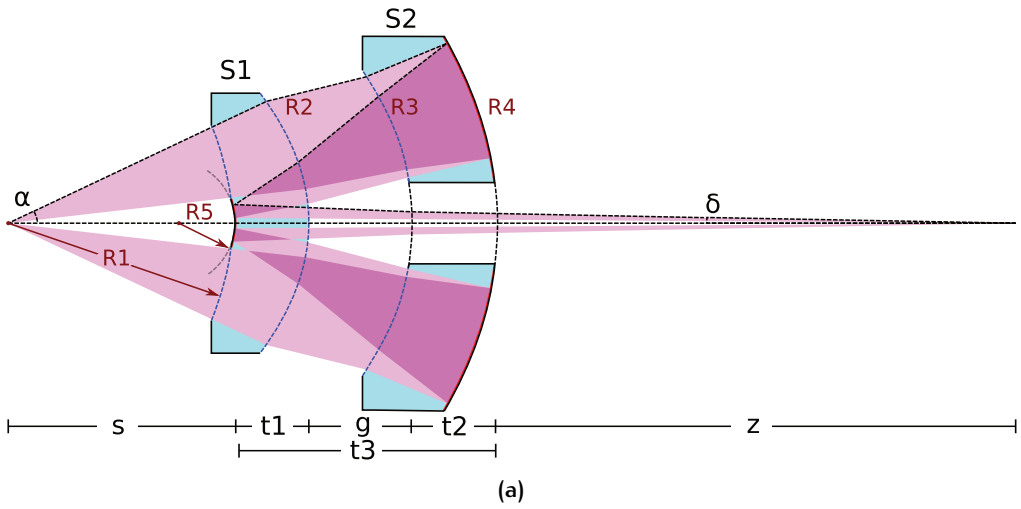

Figure 26: Schematic of a catadioptric imaging system with two Mangin mirrors.

one set was reported to keep design properties at low temperatures for wavelengths in the optical regime [168], while a second one showed astigmatic behavior after thermalization by observing Be^+ [97]. These designs obtain working distances of 2 mm, 4 mm, 20.125 mm and aim to fullfill the conditions of Burch [182] eliminating third order spherical aberrations without the need of an aspheric surface. The elements obtain a numerical aperture up to NA= 0.55 . Their geometry is given equivalently to a Schwarzschild objective for the following ratios of primary-mirror radius R_1 , secondary mirror radius R_2 and focus length $\sqrt{5}+1 : \sqrt{5}-1 : 1$ for an infinity corrected system. To achieve an achromatic design, the entry surface curvature R_0 is required to be equal the focal length $R_0 = f$ and, for an infinity corrected system, ideally the exit surface needs to be flat, while a finite focus would require a radius $R_3 = f_b$. Thus, the photons emitted from any ion close to the optical axis pass always perpendicular through the first surface of the substrate and exit with just a small deviation. This condition limits naturally the field of view. Further investigations into these types of catadioptric systems showed, that for such geometries, sweet spots exist in dependence of the numerical aperture and the wavelength [183]. Furthermore, it was pointed out, that a decentering of less than 30″ between the reflective surfaces is required to suppress astigmatism [183].

To realize a system with such requirements and including the geometric prerequisites of the trap chamber, the working distance is increased to 64.923 mm at a $NA = 0.40$. While the condition on using only spherical surfaces is sensible, since they offer more sufficient manufacturing and metrology capabilities, it will introduce large obscuration. To compensate for this, two measures were taken. First, the reflecting surfaces became conic, second, the optimized field of view was reduced to 350 µm. This allowed for a transmission increase to 92.5% by limiting the maximum

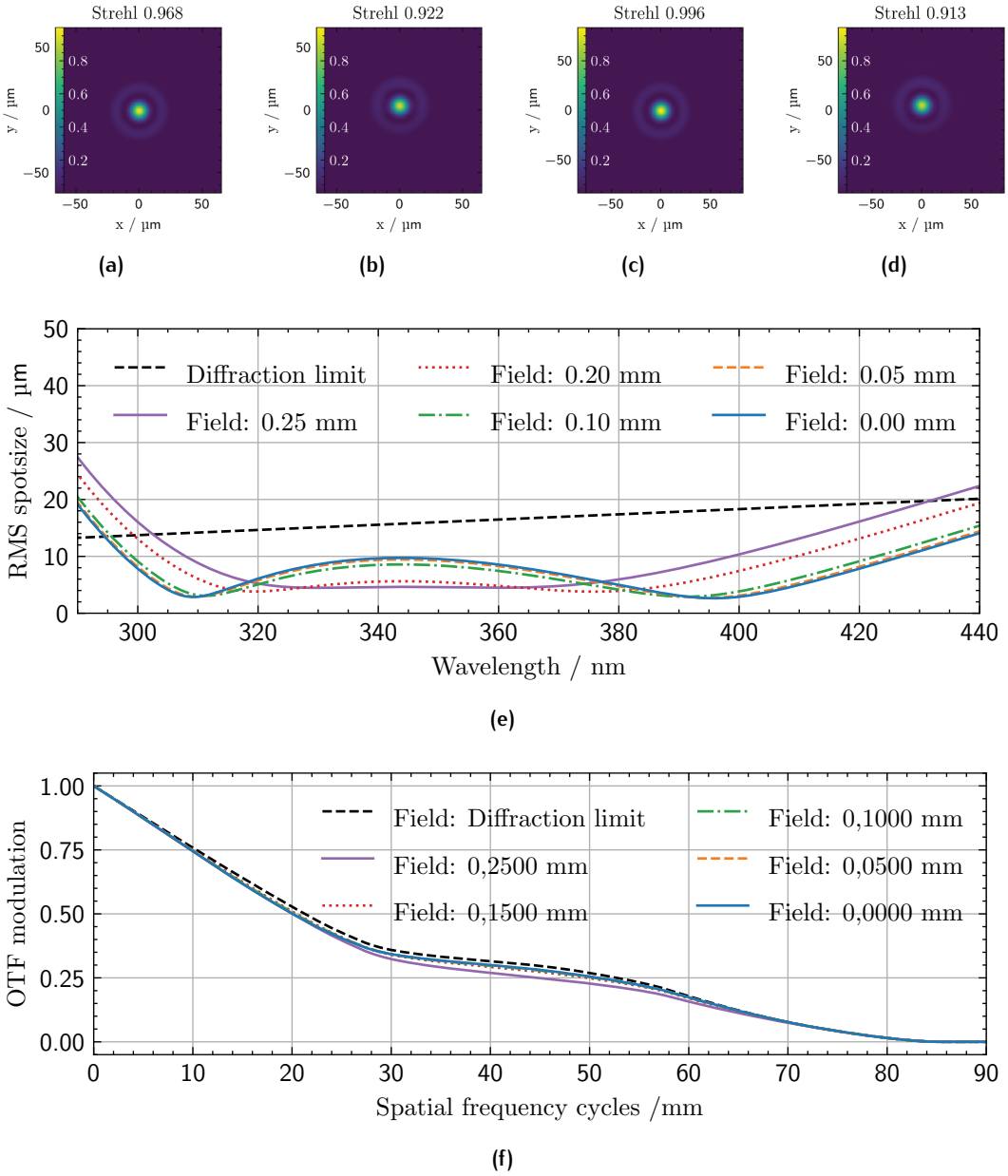

Figure 27: (a,b) simulated point spread functions for Be^+ at 313 nm wavelength on-axis (a) and at a field height of 250 µm (b). (c,d) The same for Ca^+ at 397 nm. (e) RMS spot size diagram over the wavelength range (290 – 440)nm. The blue line indicates the on-axis field. For wavelengths between one observes a slight increase due to chromatic aberrations. If the optimized wavelengths spread further, they bandwidth of the shorter wavelength decreases. (f) Modulation transfer function in the focus for Be^+ at different fields.

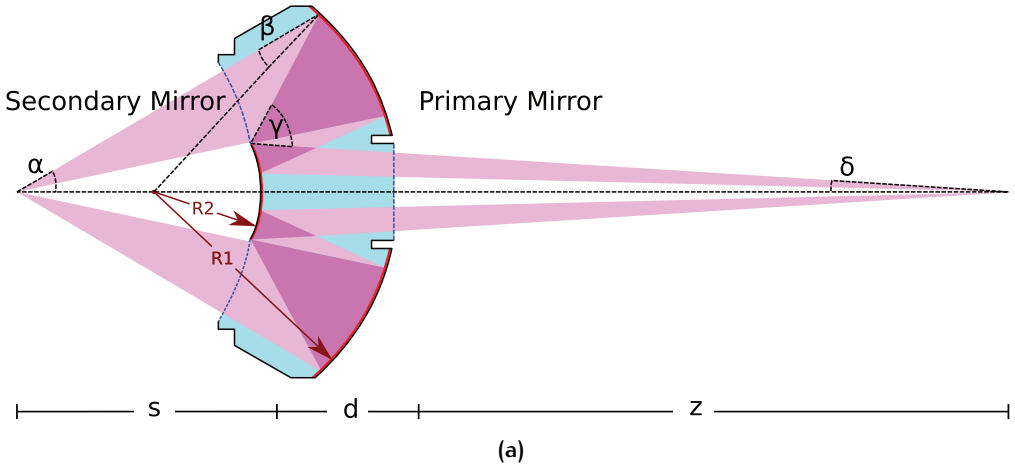

(a)

Figure 28: Schematic of a monolithic, catadioptric imaging system. Similarly to a Schwarzschild-type mirror system it has two reflective surfaces.

Table 7: Parameters for a catadioptric, monolithic imaging system with NA=0.4, $S = 64.933\,\text{mm}$ working distance and 30x magnification. All elements are made of Corning 79-80 UVFS. Both reflecting surfaces do obtain an conic constant $\kappa_P = -0.139$ and $\kappa_S = -0.587$. Due to the entrance- and exit surface geometries, the spot size asymptotically decreasing until reaching the minimum around $\lambda = 300\,\text{nm}$.

Element	Surface	Radius /mm	Thickness /mm	Diameter /mm
S1	3 (T1)	-64,537	42.00	70.00
S1	4 (R1,r,c)	-64.248	-40.00	92.00
S1	5 (R2,r,c)	-12.00	38.50	15.00
S1	6 (T2,r,c)	∞	38.546	15.00

surface diameter of the secondary mirror to 15 mm. Consequently, the central distance between entrance and first reflecting surface was increased to allow for radii which can be manufactured. While conic surfaces usually introduce difficulties and limit the tolerances, an $NA = 0.99$ system with conic secondary mirror was previously presented, showing a diffraction limited performance [184].

5.3.1 Monochromatic single lens on 4K

Following previous design studies [97], a single substrate with two aspheric surfaces was scaled up to the required working distance of 60 mm. In Table A.5 , the lens parameters for the original dimensions and design tolerances are shown. This lens is optimized for light collection of Be^+ at a numerical aperture of $NA = 0.45$, a working distance of 20 mm and a back-focus ratio of about $1:5$ resulting in a paraxial magnification $M \approx 3.8$. One finds a diffraction limited 250 µm field-of-view, which allows for loose mounting tolerances in radial direction. At the PTB, this optical ele-

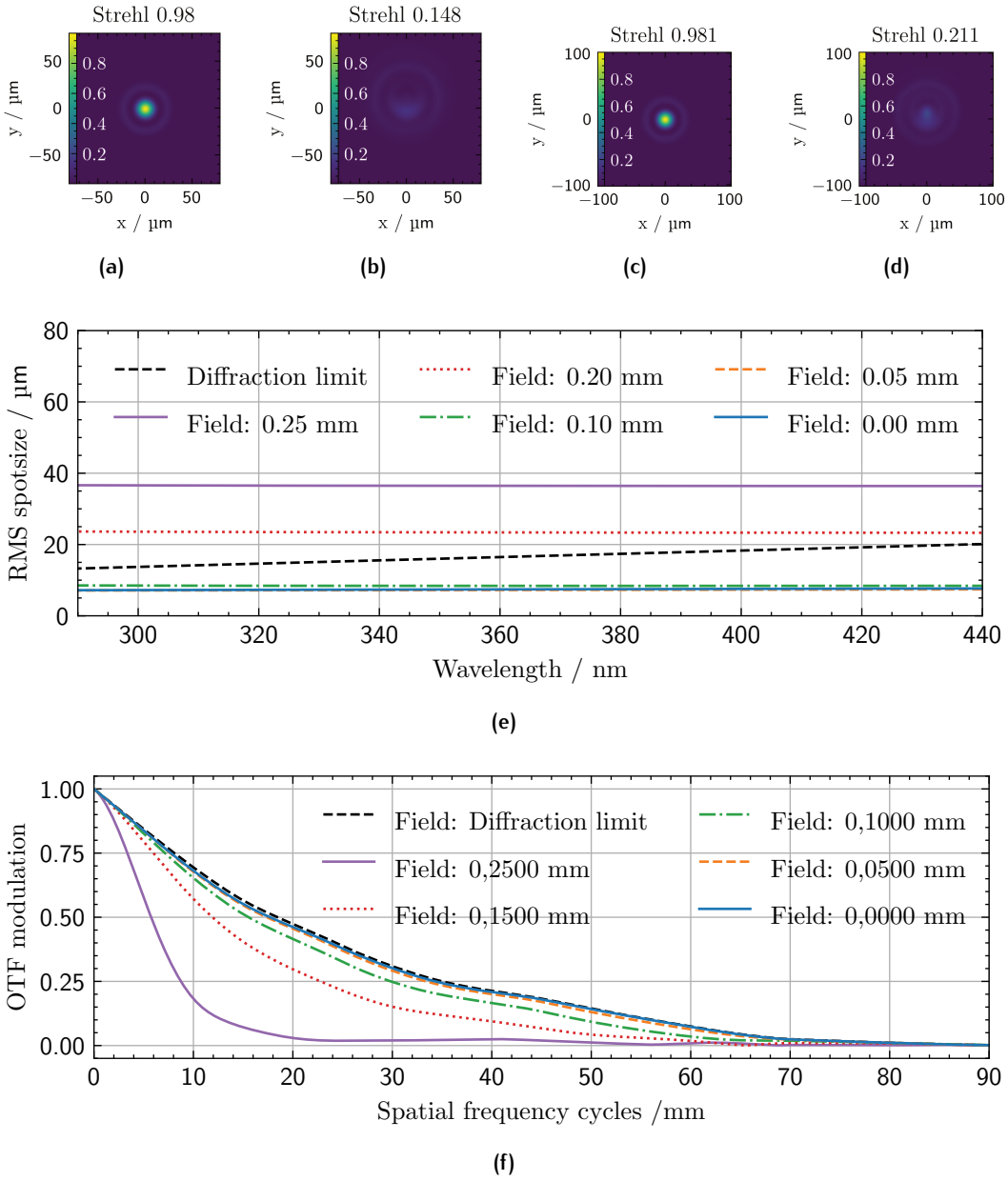

Figure 29: (a) simulated point spread functions for Be^+ at 313 nm wavelength (a) on-axis and (b) at a field height of 250 µm . (c,d) The same for Ca^+ at 397 nm. (e) RMS spot size diagram over the wavelength range (290 – 440)nm. The blue line indicates the on-axis field. Due to the usage of only reflective elements, the spot size stays constant over the full spectrum. If the optimized wavelengths spread further, they bandwidth of the shorter wavelength decreases. (f) Modulation transfer function in the focus for Be^+ at different fields.

ment is just mounted to a z-axis piezo stage to compensate for a focus shift due to the thermalization at 4 K [97]. With the given tolerance parameters, the average on-axis RMS spot radius for 10^4 Monte Carlo samples with an assumed normal distribution for each of the given tolerance parameters is $r = 5.15\,\mu m$ compared to an airy radius of 1.6 μm. Now, the lens parameters are scaled up to a working distance of 60 mm and the aperture is reduced to NA= 0.4 resulting in a nominal RMS spot size of 1.68 μm. Since only the Airy-radius is increased to 1.83 μm due to the reduces aperture, the average RMS spot simulations are comparable and end up at 8.4 μm for the same tolerances. This is expected, since the substrate now does obtain a thickness of 32.4 mm increasing the offset from the optical axis for equal decentering angles of the two surfaces. While this lens seems to perform exceptionally well and offers

Table 8: This is a list of surfaces and aspheric parameters (a_i) for the upscaled PTB-type bi-aspheric lens which was designed by [97]. Due to the experiment restrictions, the numerical aperture was reduced to NA= 0.4 resulting in a smaller diameter of the lens. Due to the otherwise equal scales, the magnification is the same at $M = 3.84$. Since the ratios of the front- and backfocus are well balanced, equal tolerances comared to the PTB dimensions result in an average RMS spot size of 8.4 μm after Monte Carlo tolerancing simulations with normal distributed variables.

Element	Surface	Radius /mm	Thickness /mm	Diameter /mm
S1	2 (T1,a)	80.533	32.40	62
S1	3 (T2,a)	-39.851	284.68	66

Parameter	T1	T2
κ	-6.49573920	-0.59350853
a_4	-2.8299629E-7	7.246296E-7
a_6	9,7189300E-13	6.59753E-11

a diverse set of mounting capabilities due to the 10 mm edge thickness, one drawback is the long backfocus. With a total beam path of 376.88 mm from the trap center, the image plane lies 70 mm behind the trap chamber reentrance window. At a distance of 157 mm, between the heat-shields of the cryogenic stages, a beam diameter of 46 mm needs to pass through, while at the entrance window a aperture of at least 19 mm is required. Such openings to room temperature would increase the heat load of the cryogenic stage immensely. Thus this system was retracted. By decreasing the backfocal length, higher aspheric order need to be added to the system. For instance, at a backfocus of 150 mm the tenth order was added to compensate for higher order coma. While the tolerancing spot sizes intuitively kept ranging around 6 μm, due to the increasing backfocal NA, the diffraction limited spotsize was decreased. Thus, the imaging resolution became worse over the full field of view.

5.3.2 Considerations for cryogenic designs

While all of these systems are performing exceptionally well in simulations, one needs to consider environmental impact on the 4 K stage by the rather large viewports required to transfer the light to room temperature. For glasses, the emissivity is about 0.9 [91]. Thus, the surface area would irradiate at a much higher temperature compared to the heat shield. A system with direct line of sight from room temperature to the 4 K stage does ideally obtain an intermediate focus. For the VAUQSI experiment, the focus aperture is reduced to 3 mm in diameter. Thus, similar to the existing CryPTEx-SC setup [73] a single bi-aspheric lens was thermalized on the 40 K stage to refocus the light in a distance of about 30 mm behind the vacuum window. In addition, the 4 K lenses close to the resonator are optimized to focus

5.4 THE 4K STAGE

Mounted on the top 4 K shield, a seven lens stack as depicted in Figure 30 is located. This assembly is divided into two main sections. The first section, closest to the radio-frequency quadrupole (RFQ), features a titanium cell housing a collector lens and a compensator. In the second section, within a titanium tube, the light is then refocused onto a plane 157 mm from the trap axis. The sixth element does obtain the strongest power at the last surface and serves as secondary compensation lens and mounted in an aluminum cell. All of these six lenses are stabilized at four Kelvin. Due to the nearly 1:1 imaging results a 1.3 magnification at an image space numerical aperture of 0.3 at the intermediate focus. In Figure 31, a schematic of the 4 K lenses is shown.

Optimization process

With the given boundaries of geometry and object size divided into seven points on the height axis, in contrast to the single lens in Section 5.3.1, the initial design study for a potential system involved flattening the entry surface to limit the system size. While a concave entry surface could have minimized wavefront distortion by decreasing the refraction angle gradient along the radial direction of the surface, it would have necessitated larger lens diameters or increased bending radii of the second surface and all following lenses. Additionally, a smaller gap between the resonator and lens would have reduced the pumping cross-section. To prevent obscuration due to the lens cell mounts, for the whole system, the substrate radius was increased by 2 mm with respect to the free aperture depending on the marginal ray circle. In addition, various penalties, such as minimal edge thickness and minimal

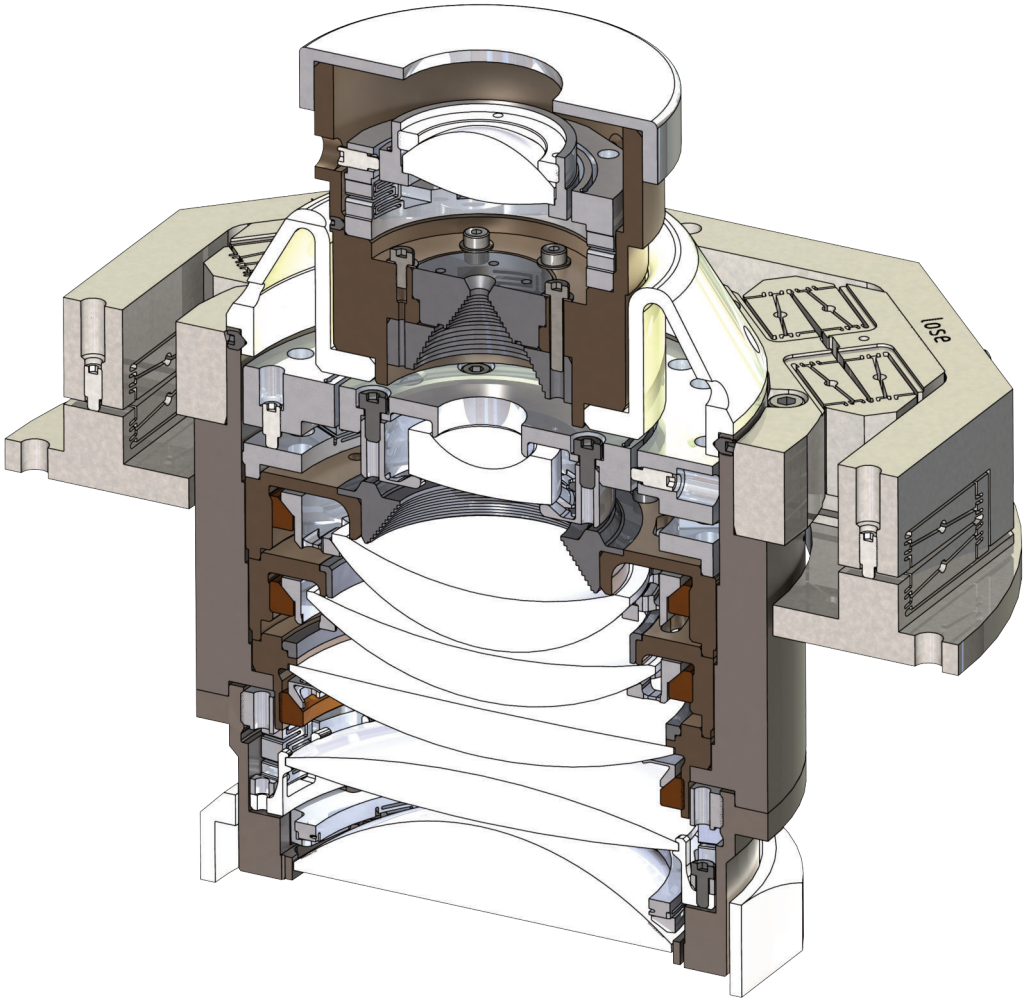

Figure 30: Sliced contour rendering of the cryogenic lens including manipulator, which is mounted on the 4 K heat shield.

and maximal center thickness, were introduced to the merit function. Furthermore, equally weighted, the RMS spot radius and wavefront were added. Thus, the function to minimize was:

$$M = \min\left[\sum_{k} P_k^{\mathrm{GEO}} + \sum_{i}^{\mathrm{Field}}\left(P_i^{\mathrm{WFT}} + \sum_{j}^{\mathrm{Angle}\,\theta}\sum_{l}^{\mathrm{Angle}\,\phi} P_{i,j,l}^{\mathrm{RMS}}\right)\right]$$

where $P^{\mathrm{GEO}}k$ denotes the geometric restrictions subsequently added for each lens, $P_{i,j,l}^{\mathrm{RMS}}$ is the parameter minimizing deviations from the ideal RMS spot size, and P_i^{WFT} minimizes the wavefront error for each field. In addition to the field heights, multiple start angles referenced to the optical axis were sampled. Subsequently, the merit function was minimized, and if the full system imaging performance did not converge and form an image with a Strehl ≈ 1 for each field height, another lens was added. While for most microscope objectives, four lenses are sufficient to project a close-to-perfect image at a given NA, these systems do feature an infinity-corrected focus. To form an intermediate focus at a 1:1 ratio, the number of lenses must increase. For this use case, eight spherical lenses, including some very thin ones, formed a sufficient image. However, since the ratio of a lens diameter to its thickness should not exceed 10:1, this system was retracted, and instead, the first lens was modified to become an aspheric with a_6 and a_8 coefficients. With that modified surface, the number of elements decreased to six.

To decrease the sensitivity to introduced imaging aberrations, another condition was implemented into the merit function: The refraction angle of each probed ray

$$\theta_{i,j,l,p} = \min(\arcsin\left(\frac{n_{i,j,l,p}}{n_{i,j,l,p-1}}\sin\left(\theta_{i,j,l,p-1}\right)\right))$$

at each surface p was minimized. This condition is similar to the lens bending technique, where a lens with large power is divided into many elements with minimal power. This resulted in ray propagation close to that of the final system, shown in Figure 31.

Lastly, fabrication tolerances were introduced into the merit function. While up to this point, the optimization for the best nominal performance (with reduced alignment sensitivity) was the focus, the system was now tuned to provide the average performance of a set of assemblies by performing a sensitivity analysis at each step. Thus, the results, as shown later in Figure 36, represent the most likely performance of the lens stack at given tolerances. This process was iteratively modified. Furthermore, single lenses with concentric surfaces were modified to allow for surface metrology on the lenses during fabrication. As a result, the power of the last lens increased again. Since S6 features an optimal aspect ratio, tolerances were tightened for that lens.

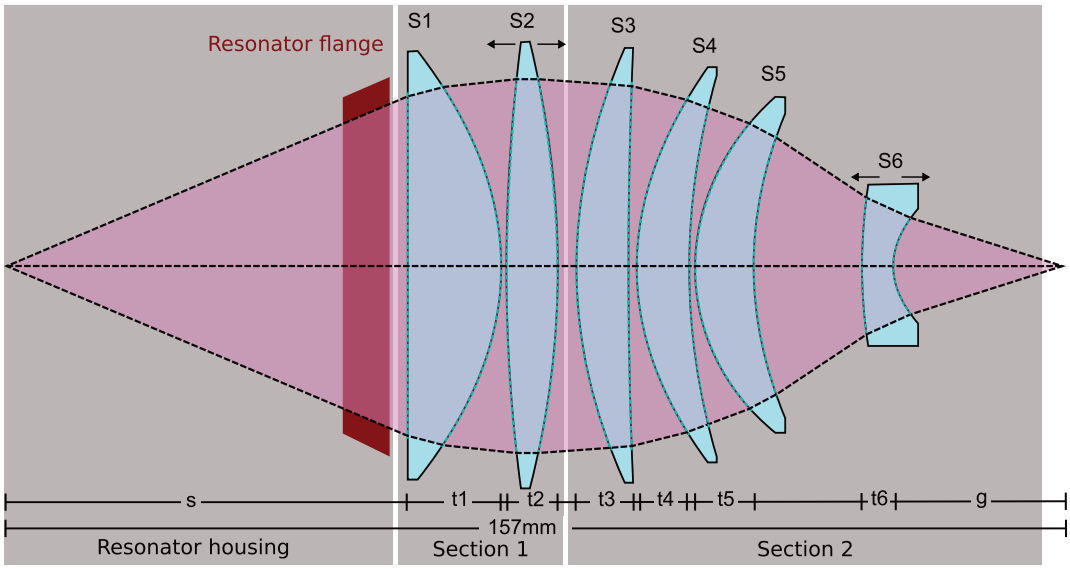

Figure 31: Schematic for the VAUQSI cryogenic lens system on 4 K. In red the minimal distance to the beryllium ions is denoted: The niobium grid on top of the resonator. S1 is the plano-aspheric lens, S2 an S6 two adjustable lenses. The due to the optomechanical design around the lenses, the system is divided in two stages.

5.4.1 First section

Collector lens

Located approximately 60 mm from the trap axis, the first lens features a plano surface with 63.5 mm diameter, shown in Figure 32. Its outgoing surface has an aspheric geometry, designed to compensate for spherical aberrations and decrease the number of elements to fit the stack within the 4 K stage. This lens, crafted by the company Aspheric on, is mounted within a titanium tube and centered by six flexure arms, each spanning 30° at an inner radius of 32 mm. Three arms, evenly distributed radially, allow the adjustment of the aspheric lens using 7 mm long, fine threaded M3x0.25 pins. At the edge of each arm element, a cylindrical volume acting as a contact for the lens was inserted. The diameter of this part is 1.6 mm. This concludes in press fit applying Hertzian contact stress since each arm needs to be pushed out by 0.5 mm to fit the lens in. To mitigate potential malfunctions from burns during the wire erosion process forming the arms, the pin threads are reduced at a length of 2 mm to a diameter of 2 mm at the ends to ensure a contact between pins and arms. Furthermore, an aluminum ring with six flexible elements, each measuring 13 mm in length and 3 mm in width, axially secures the lens by applying a defined preload. Each element is connected to the ring via two bridges, each 0.5 mm thick and 5.1 mm long. Six M2.5 screws, mounted from beneath the titanium cell, ensure the precise

positioning and secure fixation of the ring. Between ring and lens, a Teflon foil was placed to prevent scratches.

First compensator lens

Following the plano-aspheric lens with an air gap of 0.75 mm on the optical axis, a 66 mm diameter bi-convex lens with a central thickness of 7.55 mm is clamped by twenty two aluminum arms of 2 mm width, 6 mm length and 0.75 mm strength connected to a 77 mm diameter ring. Facing the aspheric surface, the curvature radius was set to 238 mm, while the second surface obtains 138 mm. The ring is screwed onto a flexure feathered mounted system containing twelve wire eroded spring elements. To compensate for thermal expansion and shifts of the refraction index or optimize the refocus in general, the lens can be adjusted in a range −0.5 mm to 1.0 mm along the optical axis by six M3x0.25 pins. According to FEM simulations[1], twenty two fingers apply a locale force of 2 MPa on the substrate, which leads to a deformation of $\Delta S(\rho,\phi)/S(\rho,\phi) = 10^{-5}$ at the edges and $< 10^{-6}$ in the beam path. A 80 mm × 0.5 mm thread, which is loosely matched to the titanium counterpart, ensures a secure preload of the springs. Due to the differential expansion integrals of titanium and aluminum, the thread was cleaned and polished multiple time before being coated with Apiezon N vacuum grease to prevent cold welding. Figure 33 shows the assembly

5.4.2 The second section

The previously described section is mounted by eight M3 screws to a 96 mm diameter titanium barrel containing three lens cells crafted from a Iron-Nickel alloy, Alloy 36. A fourth lens is mounted within a aluminum housing, which can again be manipulated along the optical axis and in addition radially.

The iron-nickel alloy cells

To reduce the impact of length changes in the second stage, the lens cells were crafted with a material obtaining a low expansion integral, an alloy containing 64% iron and 36% nickel. This alloy is commonly known as Invar or Alloy 36. While similar alloys additionally substituted by cobalt (Super Invar) do obtain an even lower thermal expansion coefficient, most of them undergo a maternistic restructuring transformation at low temperatures and loose their low expansion properties [185]. Within the cell closest to the resonator, a 64.5 mm diameter meniscus lens is mounted by an aluminum flexure spring, which is pushed onto the lens by a threaded brass ring. This

1 Solidworks Simulation Premium

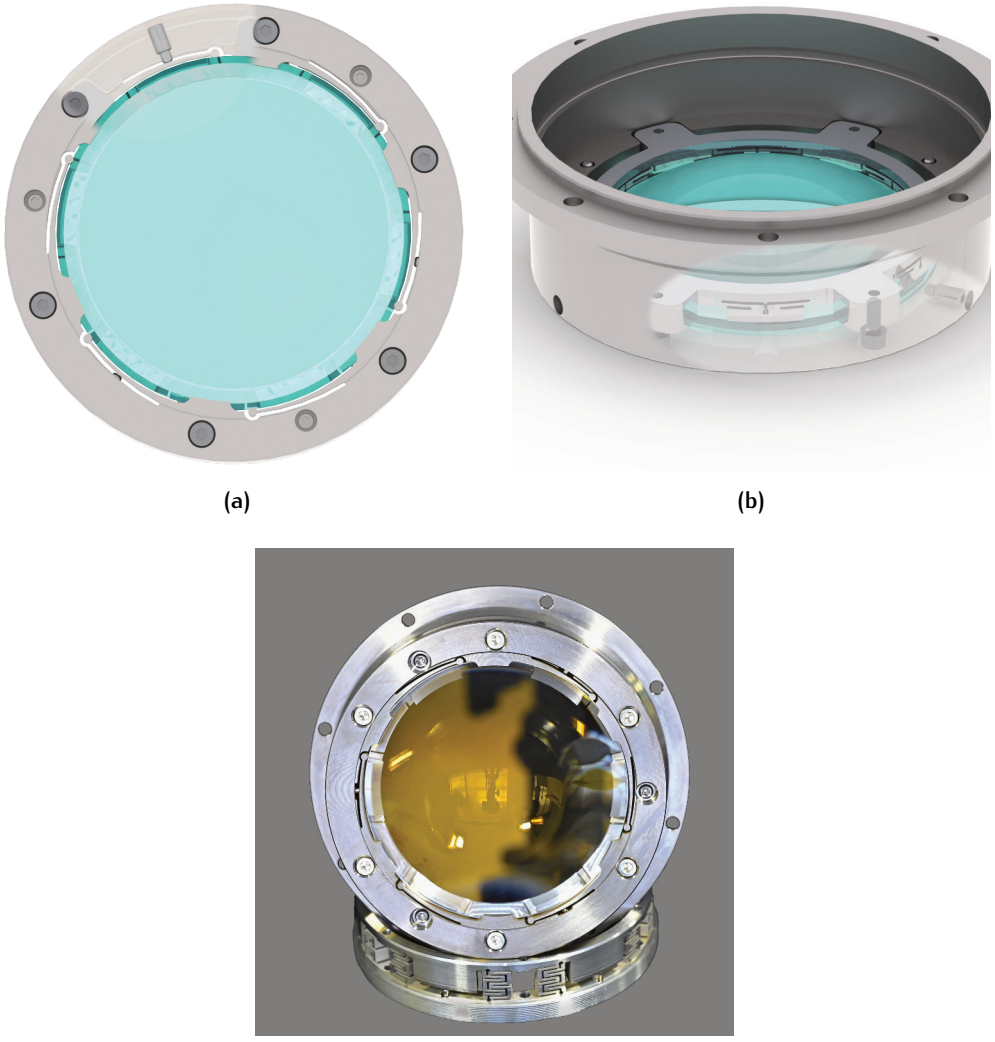

Figure 32: (a-b) Rendering of plano aspheric lens mounted in the titanium cell. Centering is achieved by six wire eroded arms, on which three can be fine adjusted by 7 mm long M3x0.25 pins. Along the optical axis, the lens is pre-loaded on six feathered points. (c) Image of the assembled lens.

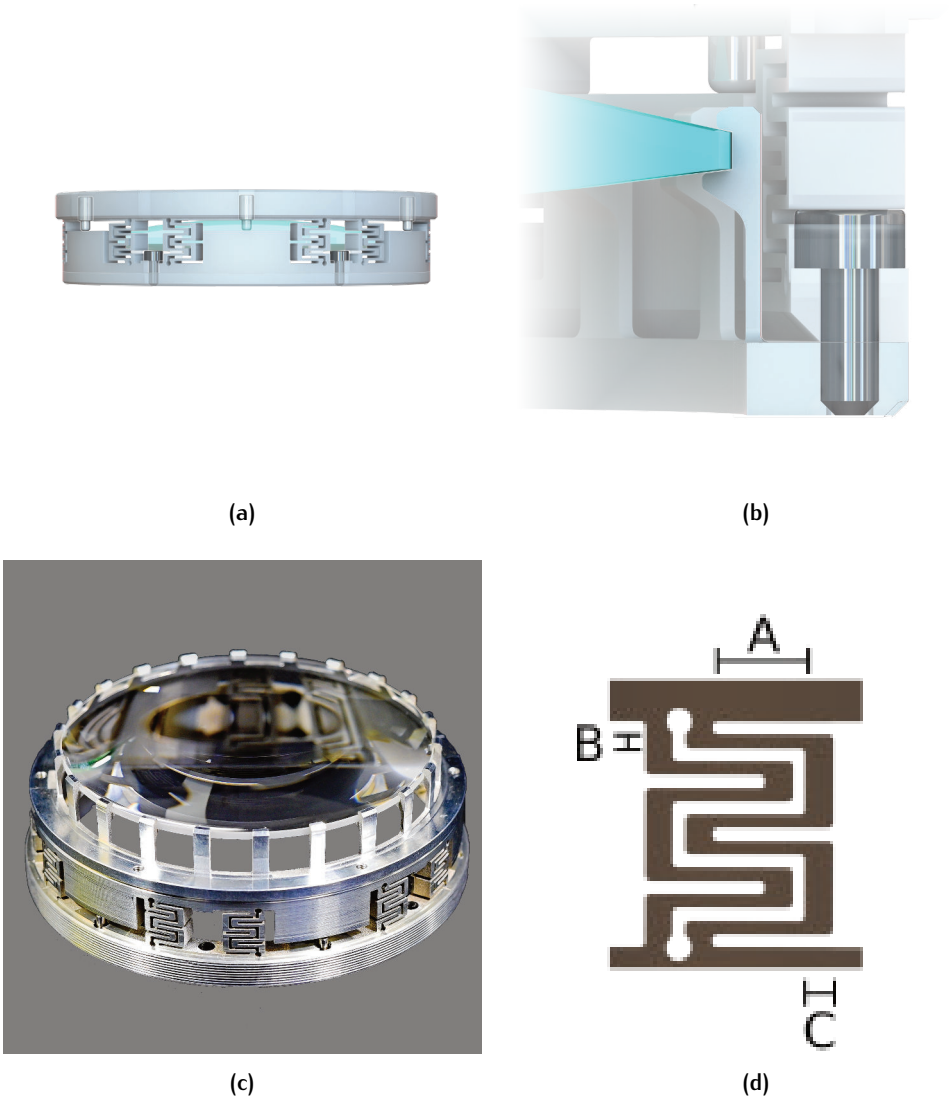

(a) (b)

(c) (d)

Figure 33: (a-b) Rendering of the compensator lens mounted in the adjustable aluminum cell. The lens is centered by twenty two arms scaling 2 mm in width, 6 mm in length and 0.75 mm in strength. The outer part of the ring was designed to lengthen up to 0.5 mm or shrink 2.0 mm by adjusting in total six fine threaded pins. (c) Image of the pre-loaded lens before assembly on the outer ring. (d) profile of the EDM machined springs. The values are $A = 5\,\text{mm}$, $B = 1\,\text{mm}$, $C = 2\,\text{mm}$.

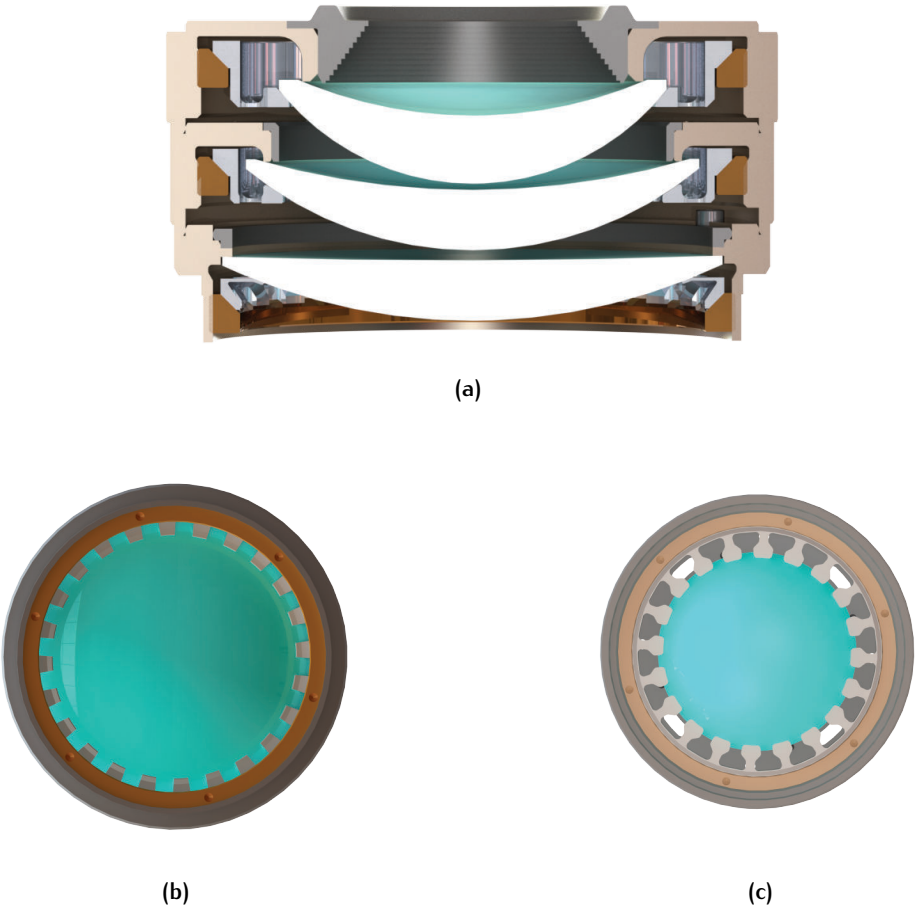

(a)

(b)

(c)

Figure 34: (a) Rendering showing the stacked lenses inside the Invar cells.(b) Top view of the lowest lying lens. (c) View on the top lens. The element between both was similarly mounted as shown in (c). In surrounding the flexible aluminum arms, a brass ring is applies a preload.

ensures a good first order centering, and allows to apply enough preload to safely secure the lens at the defined position. Since the spring is separated into twenty four sheets of 0.4 mm strength, 3 mm width, the total spring force of the lenses is reduced. To ensure maximum flexibility on the arms, the ring was cut out in between each element increasing the length to 4 mm. This is in particular important, since the contact between lens and cell is only at the very outer edge, which results in a easily applicable torque on the lens. Due their higher curvature, the next two lenses with a diameter of 58.5 mm and 50 mm, respectively, are clamped on the outer edge of a mounting ring. This is advantageous, since the ring height and radius can be tolerated well within 10 µm. All lenses are securely mounted and preloaded by brass rings. A view on this lens system is given in Figure 34. An top of the lens stack, an anodized aluminum aperture was placed to reduce straylight.

Second compensator lens

Closest to the intermediate focus, a 24 mm wide, 7.8 mm thick lens completes the ensemble on the 4 K stage. This lens is housed in an aluminum frame similar to the first compensation lens. Additionally to the axial manipulator, three fine threaded pins are actuating the substrate in radial direction. This measurement was taken, since this lens obtains the surface with the highest curvature. Thus, it is together with the aspheric lens the most sensitive element in the system. The radial stroke is in the order of a few hundred micron.

Surface	Radius	Thickness	Material	Clear Radius	Mech Radius
Trap center	-	59.596	Vacuum	-	
Standard	∞	13.750	Corning 7980	28.575	31.75
Aspheric*	-43.556	0.750	Vacuum	28.575	31.75
Standard	238.0	7.550	Corning 7980	29.7	33.00
Standard	-138.0	2.932	Vacuum	29.7	33.00
Standard	76.335	7.750	Corning 7980	29.025	32.25
Standard	955.725	1.145	Vacuum	29.025	32.25
Standard	46.0	7.750	Corning 7980	29.25	29.25
Standard	101.32	0.806	Vacuum	26.325	29.25
Standard	31.93	8.75	Corning 7980	25	25
Standard	57.5	15.996	Vacuum	22.5	25
Standard	75.636	4.5	Corning 7980	12	12
Standard	11.34	25.24	Vacuum	7.6	12

Table 9: List of surfaces and parameters at the 4K stage. Each lens element is separated into two surfaces with curvature radius and thickness/distance to the next element. All polished areas on the surfaces are given by the clear surface parameter, while the mechanical radius is the size of the lens.The aspheric parameters are: $\kappa = -0.771$,$\alpha_6 = 3.96683694 \cdot 10^{-7}$, $\alpha_8 = 4.346151736 \cdot 10^{-11}$.

5.4.3 The 40K Stage

On the 40 K stage, a single, bi-aspheric lens is thermalized. The lens is located 20 mm behind the intermediate focus and refocuses the light in a distance of roughly 40 mm behind the vacuum window. To align the lens in a reproducible manner with respect to the 4K stage, it is mechanically connected to the 4 K lens tube by a PEEK-frame with 21 mm height and 40 mm diameter, shown in Figure 35. The wall strength is 2.5 mm and the total distance between the two stages is about 50 mm, reducing the temperature gradient slope. Twelve ventilation holes of 4 mm are equiradially dis-

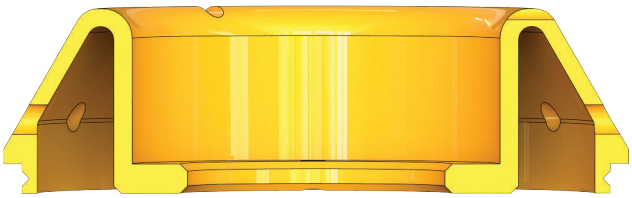

(a)

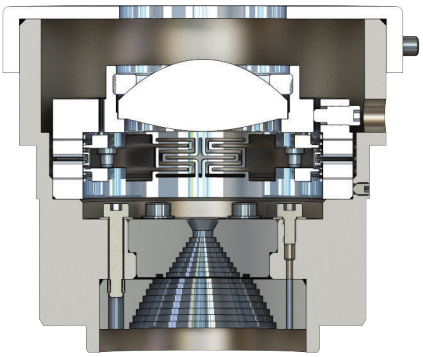

(b)

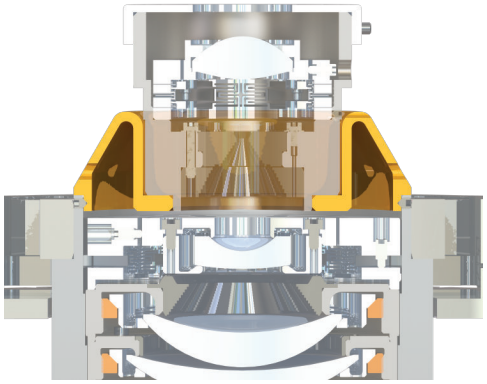

(c)

Figure 35: (a-b) Rendering of the compensator lens mounted in the adjustable aluminum cell. The lens is centered by twenty two arms scaling 2 mm in width, 6 mm in length and 0.75 mm in strength. The outer part of the ring was designed to lengthen up to 0.5 mm or shrink 2.0 mm by adjusting in total six fine threaded pins. (c) Image of the pre-loaded lens before assembly on the outer ring.

tributed along the holder to ensure a quick pumping of both stages. An Invar barrel is mounted on level with the 4 K titanium tube. This arrangement compensates the length change during cool-down from room- to working temperatures. In Figure 35 an illustration of the FEM simulation results are presented. These show a total deviation from a zero expansion of less than 10 μm which is dominated by the radial pressure of the Invar barrel on the PEEK holder.

For straylight reduction, two segmented, anodized aluminum apertures, stepwise converging in a cone shape, are mounted on the Invar barrel. The minimal opening in the lens stack focal plane through which light is passing has 3 mm size, shielding the 4 K stage efficiently from thermal radiation entering from room temperature.

In between the Invar barrel and the vacuum window, laser stray light, reflected from both the polished vacuum chamber and copper shields, is reflected by an outer stainless steel barrel, and absorbed by an inner polyoxymethylene-tube loosely sitting on the barrel at 40 K.
In Table 4, the materials utilized in this experiment, including their expansion integrals, are listed. To minimize the need for compensation along the optical axis, an iron-nickel alloy traded by the name of Alloy36 or Invar was implemented. The change in axial separation could be decreased from 41.5 μm to 4 μm for an element spacing of 10 mm, which is well within the element tolerances.

5.4.4 The 4K three axis manipulator

To align the cryogenic optical setup with respect to the trap center in once, it is mounted to a stainless steel multi-axis manipulator consisting of two monolithic elements. With a 160 mm outer radius element is mounted onto the 4 K heat shield, substituting the regular flange of CryPTEx-SC. Four flexure elements equally radially spaced by 90° allow for a ±0.75 mm axial stroke. Four fine threaded pins located in the center of each flexure spring allow for a precise height alignment and tilt compensation.

At this stage, the manipulator should be considered as first prototype. While it is possible to reach an optimal focus calibration after a few thermal cycles, the option should be considered to upgrade the it with piezo driven actuators to reach a sufficient precision. Such actuators reach sub micrometer precision, which is required considering the 1.8 μm depth-of-focus.

5.4.5 Optical performance at the intermediate focus

In Figure 36, the optical properties for the previously presented lens stack are shown, clearly, the Huygens point spread function is fulfilling the imaging condition up to a field height of 150 mm until it reaches a minimal Strehl ratio of 0.5 at maximum field height. Considerably, the optimization procedure was not tuned to return the best results, but considering fabrication tolerances of the lenses resulting in the average performance for about 2000 samples. Furthermore, the induced aberrations are of a form, where they can be compensated in the laboratory environment.

DISCUSSION ON THE THERMAL INFLUENCE OF THE LENS SYSTEM Within the simulation, the refractive index was adapted to 4 K. The results shown, are already including the thermal expansion of the cells around the substrates. For room temperature values, Table 10 shows the corrected distances. For the first- and second compensation lenses, the length changes were the largest, featuring 48 µm and 55 µm, since they feature the adjustable aluminum cells. Including the dispersion drift, the backfocus shifted by −114 µm, which is a large shift, considering the working distance of the bi-aspheric lens to be 20 mm. Thus, measures need to be taken into account for aligning the elements to each other. The refocusing performance decreased, as shown in Figure 37 on the reduced contrast in the mid frequency cycles. Similar results were produced in the other direction by optimizing with material characteristics at room temperature, which were then scaled down to cryogenic temperatures.

5.4.6 The room-temperature system

In a distance of 295 mm to the trap center, a 10 mm thick, 25 mm diameter fused silica re-entrance window is located. Closely behind, at a distance of about 30 mm, the second intermediate focus is located, projected by the bi-aspheric lens. Contrary to the intermediate focus within the cryogenic stage, the accessible lens sets at room temperature can be manually moved at all times. Furthermore, the numerical aperture in the second focus is now decreased to $NA \approx 0.05$ and allows for further guidance through standard, commercially available lenses[2] with diameters between 25.4 mm and 30 mm. In Figure 38, a top view of the complete assembly is shown. In Table 11 and Table 12, the parameters for all remaining lenses are referenced.

The whole system is divided into several stages. First, the entering light cone is infinity-corrected by the lenses I1 – I6. This measure was taken to allow for a flexi-

2 OptoSigma

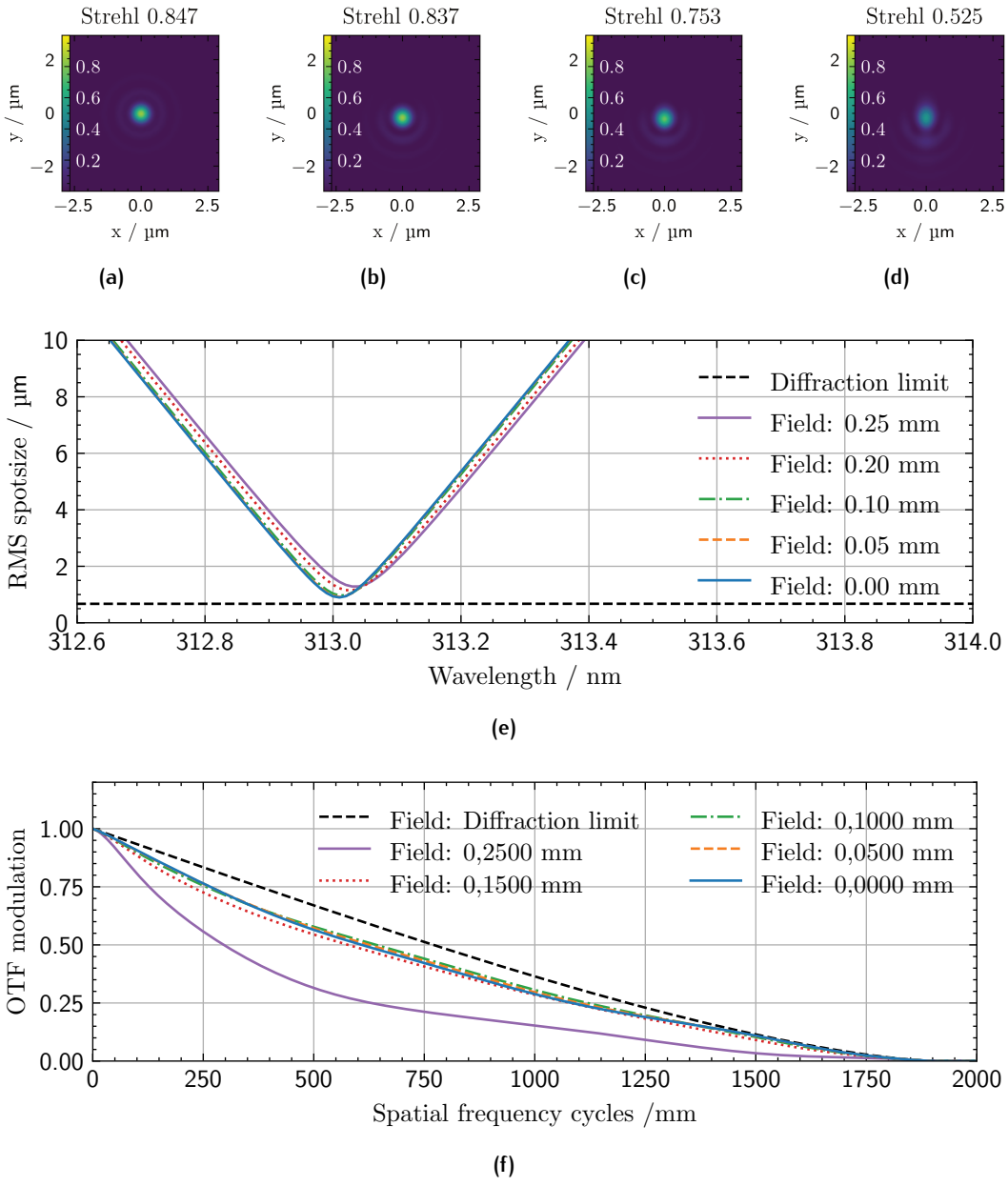

Figure 36: Simulation results for the VAUQSI 4 K stack at this temperature. (a-d) Point spread functions for Be^+ at 313 nm wavelength (a) on-axis and at a field height of (b) 125 µm, (c) 175 µm, (d) 250 µm (e) RMS spot size diagram around the cooling wavelength. (f) Modulation transfer function in the focus for Be^+ at different fields.

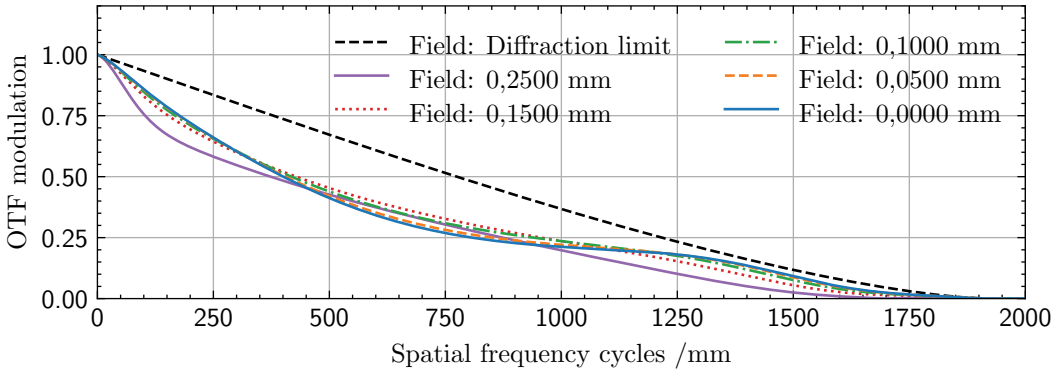

Figure 37: Simulation result of the lens stack at 4 K, thermalized at 293 K. Lens cell distances and thermal refraction index were changed to the given temperature.

ble attachment of additional detectors, such as a fast-gating CCD[3], which features a 55 µm pixel diameter. Since the second set of lenses F1 – F3 focuses light at a magnification of about $M = 30$ to reach the resolution limit of the EMCCD[4], which is given by the modified Abbe condition

$$d_{\mathrm{px}} = M \cdot \frac{1.22\lambda}{2NA},$$

and yields about $M \approx 27$ for a pixel diameter of 13 µm, a larger magnification is beneficial for the fast camera. At a magnification $M = 30$, ions with a minimal spacing of 3.6 µm would still be resolvable, but being separated by only one pixel.

As denoted in Table 12, the lens assembly for the refocus is symmetric in distance around the bi-concave lens F3. While a single lens would have been sufficient to refocus incoming light on the optical axis, off-axis aberrations like coma would have distorted the image of a large Coulomb crystal. With this assembly, over the full field-of-view, no further aberrations are added, since it was optimized for refocusing an infinity-corrected beam.

Infinity corrected beam path

Between the lens units, two 50.8 mm mirrors (M2,M3) are positioned in an angle of 45° to the propagating beam to allow for a compact design, the mirrors are mounted within standard commercial available holders[5]. For guidance to another detector the mounts can be removed though a lid flanged onto the top plate of the inhousing.

3 Amsterdam Scientific tpx3cam
4 ANDOR iXon Ultra 888
5 mks Newport HVM-2t/u

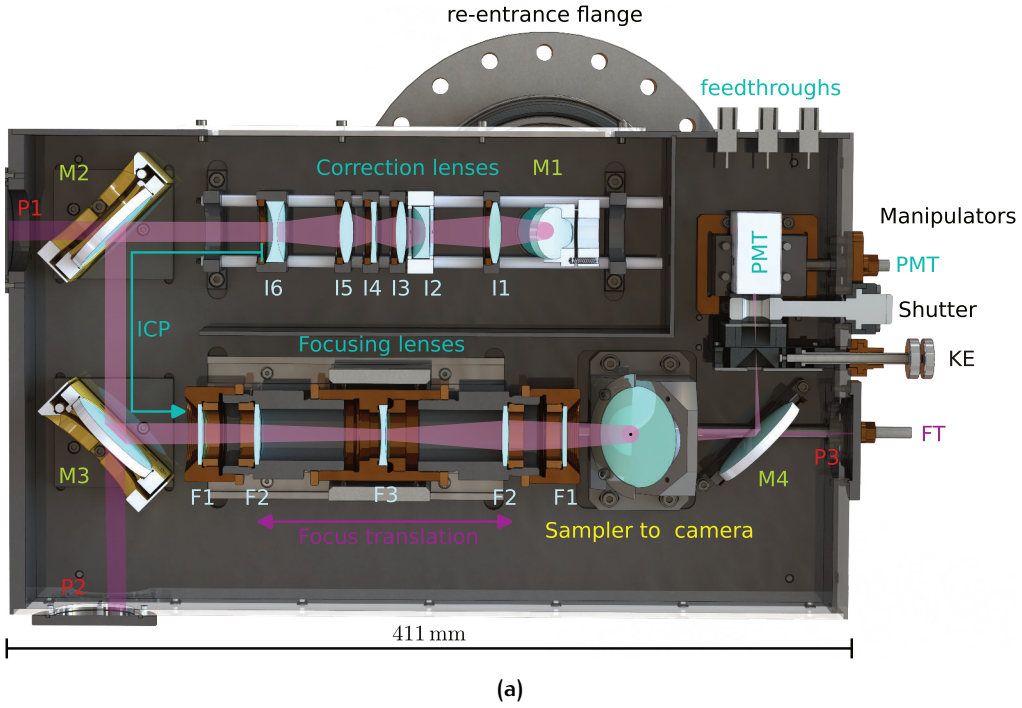

(a)

Figure 38: The imaging system lab unit consists of two subsystems. After passing mirror M1, the beam is infinity corrected through the lenses I_i and crosses two alignment mirrors (M2, M3) along the infinity-corrected path (ICP). The second subsystem, consisting of symmetrically spaced lenses F_i, focuses the beam at a magnification of $M \approx 32$ through a beam sampler to a camera and a PMT, respectively. To filter out stray light or enhance single-ion contrast, a spatial filter consisting of a total of four knife edges (KE) is positioned at the focus. For alignment, maintenance, or attachment of multiple detectors, three ports have been implemented (P1, P2, P3). A translation wheel for shifting the focusing lenses is denoted with (FT).

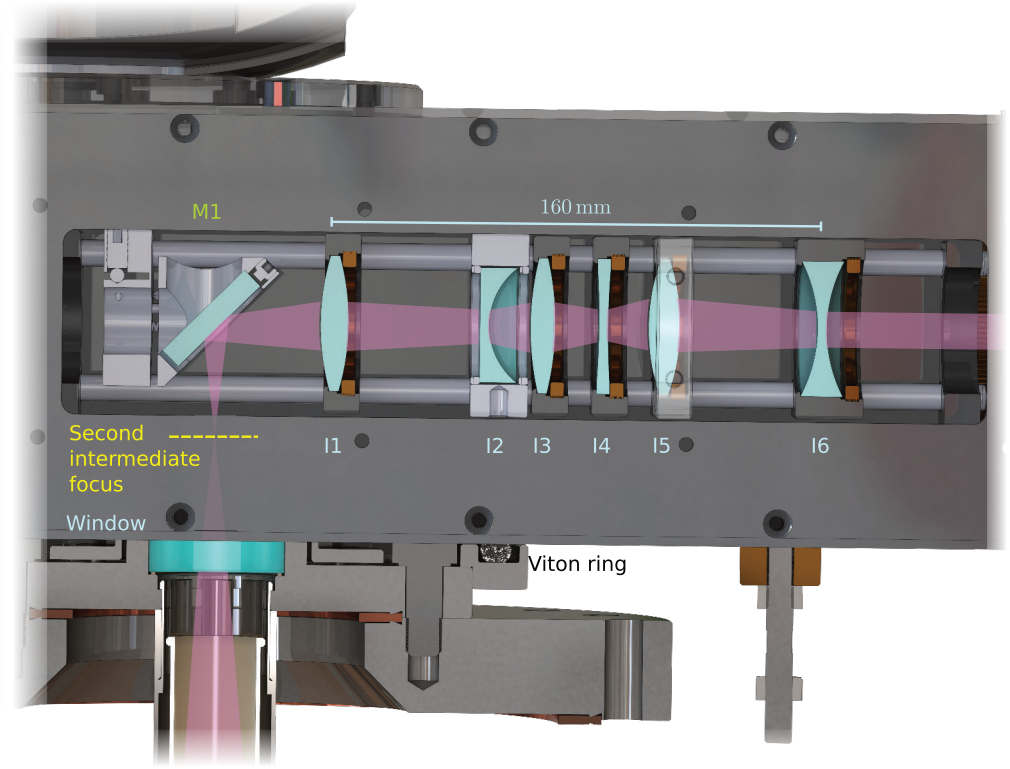

(a)

Figure 39: Laboratory unit sideview with vacuum window. An adjustable mirror couples the beam into an lens assembly, which is mounted within four rods. Retainer rings preload the lenses in the cells. Alignment and optimization on the stack can be performed by opening a lid on the side.

Since they are adjustable from top, four removable knobs are placed in the lid to allow tilting with one or more Allan keys.

Refocusing on Detectors

After passing the final lens, the beam is split by a beamsampler, mounted at a 45° angle to the beam axis. A fraction of the photons is projected onto the attached EM-CCD chip, located at a distance of approximately 85 mm from the last lens. The second beam passes through and is reflected by a fourth mirror, M4, onto a PMT. While the PMT is positioned slightly behind the focus, a knife-edge filter is placed directly in the image plane, aiming to reduce stray light. Furthermore, for single-ion readout in a string, the aperture can be further reduced and adjusted to the right focus.

Between the knife-edge filter and the PMT, a rotatable beam block is mounted to prevent the PMT from overexposure during maintenance or alignment work.

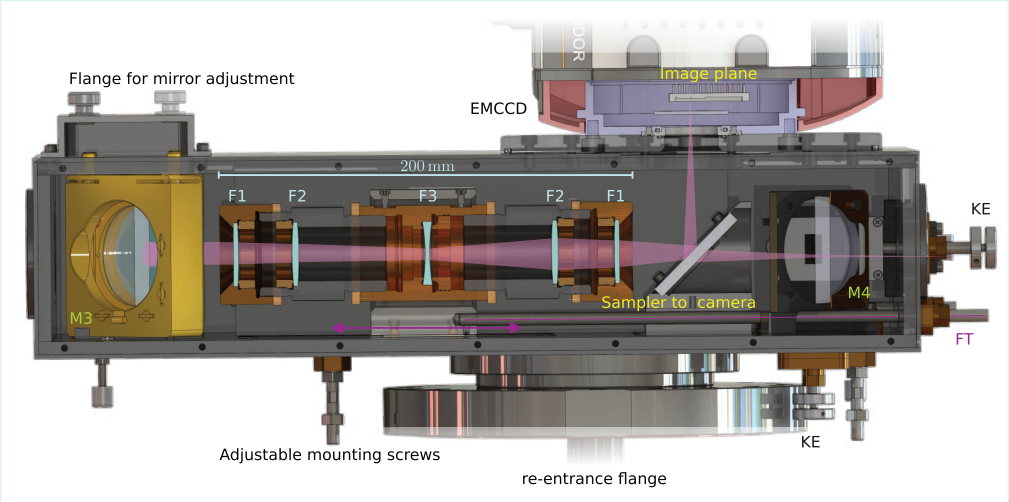

(a)

Figure 40: Laboratory unit sideview on the refocusing lens assembly, which is positioned inside a tubus.

5.4.7 Detection in the image plane

Due to the compensating lenses, the imaging condition is fulfilled again for the full field-of-view, which is shown in 41. In Section 2.1.1 the dipole emission of Be^+ was highlighted. At the design numerical aperture of $NA = 0.4$ at a saturation of $s = 1$, the number of photons collected by on the first lens element is 397 for one readout cylce over 200 µs. All lens surfaces are coated to minimize the reflections at 313 nm to 0.2% per surface. For the course of the 38 surfaces, the transmission is reduced to 92.5%. In addition, similar to the CryPTEx-SC experiment, the superconducting resonator flange obscures 10% of the emitted light. At the given wavelength, both detectors feature a quantum detection efficiency of about 32%. Thus, a total of 26% or of the photons emitted under this numerical aperture are detected. Thus, at $s = 0.2$ on average 20 photons per readout can be detected. In Figure 42, a raytracing simulation on a detector with similar pixel size to the EMCCD was performed, neglecting all noise terms of the detector. In total 10^3 photons per source were traced. For three equally distanced ions with 5 µm spacing, a signal discrimination is achieved. To enhance contrast, only pixel counts larger than 10 are shown. The maximum count number for one pixel was ≈ 420 and 85% of the photons are accumulated on a 4x4 pixel array.

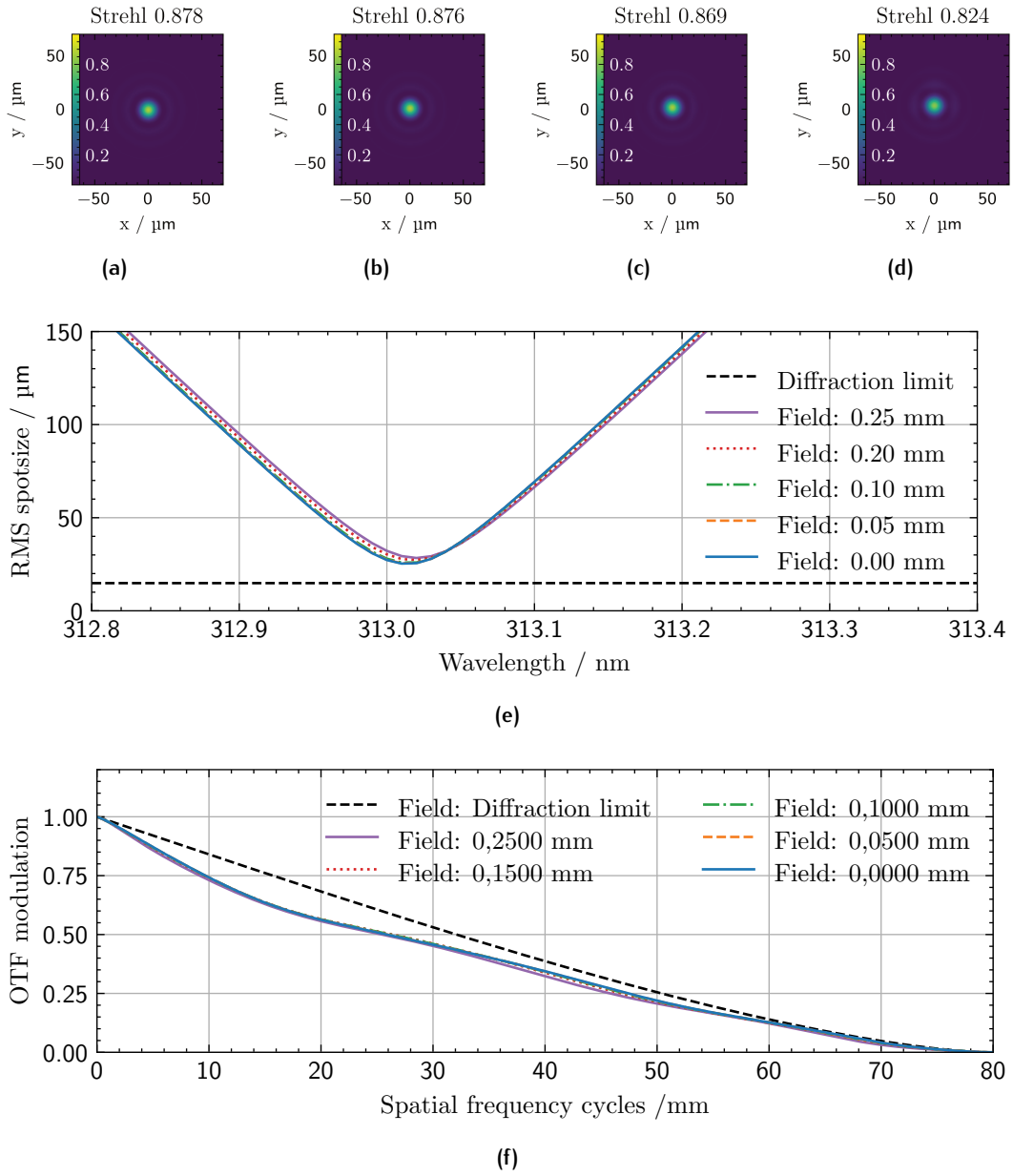

Figure 41: Simulation results for the whole VAUQSI imaging system in the EMCCD image plane (a-d) Point spread functions for Be^+ at 313 nm wavelength (a) on-axis and at a field height of (b) 125 µm, (c) 175 µm, (d) 250 µm (e) RMS spot size diagram around the cooling wavelength. (f) Modulation transfer function in the focus for Be^+ at different fields.

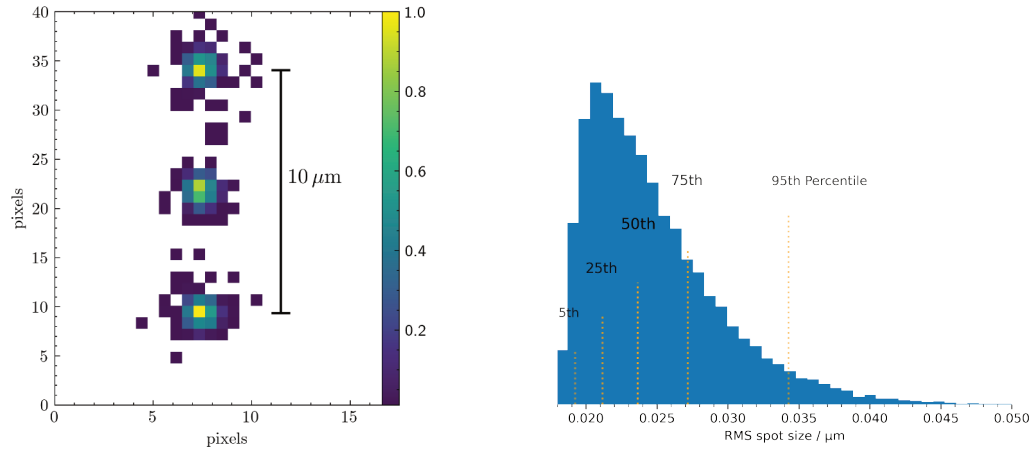

Figure 42: (a) Simulation of an image on the EMCCD detecting 10^3 photons per ion for a pixel size of 13 μm . Three equally spaced ions with a total distance of 10 μm in object space were used as light source. The maximum pixel count number was 420 (b) Monte Carlo results, based on the toleranced lenses and lens elements for the root mean squared spot size in the image plane. 26 μm correspond to two pixels.

6 CONCLUSION AND OUTLOOK

In this thesis, a the superconducting properties of a quadrupole resonator utilized as an ion trap were presented. The main characteristic, besides an increased resonance quality factor, is the Meissner state of the Niobium. By utilizing the Zeeman levels of the Be^+ $S_{1/2}$ ground state, which is sensitive to magnetic field fluctuations, first the DC characteristics of the stored magnetic field were validated and characterized, resulting in a mean half-life of about 300 years for the magnetic field strength. These measurements were performed by inducing microwaves to drive the $|S_{1/2}, F = 1, m_F\rangle$ to $|S_{1/2}, F = 2, m_F\rangle$ transition with Rabi and Ramsey schemes. Furthermore, the residual magnetic field noise was measured, by applying Ramsey schemes on the given transition and increasing the waiting time between initial and readout pulse, leading to a residual RMS field noise of 3.5(2)pT.

Due to the low noise in the magnetic field, the maximum retrievable Ramsey time was about 400 ms. Further investigations into the magnetic field homogeneity required for a reduction of the induced microwave power by about 90 dB, which allowed to resolve the $|S_{1/2}, F = 1, m_F = 1\rangle$ to $|S_{1/2}, F = 2, m_F = 2\rangle$ transitions for two stored Be^+ ions individually. With a spacial separation of 26 μm, their transition lines were shifted by 70 Hz, corresponding to a field gradient of 1 nT/(10 μm) at that time. By tuning the magnetic field coils, the gradient can be minimized.

Due to the unique trap design, no comparable values for a superconducting trap exist. Other setups involve either self referencing magnetic field coils [97] obtaining values around 200pT, or traps with attached permanent magnets and additional field noise suppressing coils. Here the retrieved values are similar [109]. While other atomic systems feature transitions insensitive to magnetic field fluctuations [186] or apply dedicated techniques to recover the phase [187], and thus exceed the measured decoherence time, this result was achieved with simplest techniques: A superconductor surrounding an ion, trapped in a radio-frequency field, and a transition sensitive to magnetic field noise, which was solely and alone driven by a microwave antenna connected to a digital frequency generator.

More sufficient techniques such as dynamic decoupling can, however be implemented into the CryPTEx-SC setup. Since the experiment aims for quantum logic spectroscopy

of highly charged ions, they are not required at this stage. One main limit of the resonator is a high operating temperature, limiting the stored radio-frequency power and thus the radial secular frequency of Be^+ to about 700 kHz. On the cryogenic system side, this was challenged for the VAUQSI experiment by improving the floating ground platform to allow for a larger pressure on the connecting sapphires. Furthermore, the OFHC copper on the lower 4 K lid was replaced by 5N high purity copper to increase the thermal conductivity between the platform and the subsequent cryogenic supply parts.

For the superconducting cavity, formation of niobium hydrides might cause a heating due to existing flux pins, which dissipate heat if exposed to (stong) AC fields. To circumvent this chemical reaction, the niobium can be baked out at 900 °C, before being doped with nitrogen, to prevent hydride forming.

In the last Chapter, multiple concepts for imaging systems for Be^+ at an NA=0.4 and working distance of 60 mm were presented. Both values are limited by the resonator geometry. Starting with a classical co-radial, purely reflective Schwarzschild objective (SO), catadioptric systems were introduced, involving two Mangin mirrors and a single substrate with two reflective surfaces. While the Schwarzschild objective is well established, it is the most demanding system regarding alignment of separated lens elements and might require either passive length compensation with, e.g., negative thermal expansion materials or an active piezo tracking. By reducing the number of substrates to a single one (CS), a rigid mount of the reflecting surfaces is guaranteed. Furthermore, the entrance surface radius is required to be close or equal to the working distance. On the negative side, the fabrication tolerances are tighter than for a purely reflecting objective, since the introduced wavefront error scales with the refractive index. For well-balanced, small systems, at extreme numerical apertures, the imaging condition was still fulfilled. This might be related to the small obscuration in that device due to an introduced conic constant. Aberrations such as astigmatism rise with increased obscuring factors [146]. Still, for such a system, excellent centration of the two reflective surfaces is required.

Both systems were purely achromatic. The Schwarzschild mirror obscures ≈ 20% while the CS does only 7.5%. Yet the diffraction-limited field of view is larger for the SO.

By splitting up the single substrate into two, the achromatic behavior is weakened, and the incoming photons are now effectively refracted. The system presented was

optimized for two wavelengths and furthermore showed a high bandwidth at close to perfect imaging condition. While the fabrication tolerances are still demanding, no additional obscuration is added by a mounting frame, leading to a transmission of 87.5%. In addition, the substrates can be mounted in various routines such that the induced stress is minimized, while the lens is still sufficiently thermalized. While the SO features a backfocus diameter of about 25 mm, the two-element lens has a focus diameter of 18 mm and the CS only 15 mm. This requires a comparably large re-entrance diameter, which induces an increased thermal radiation load.

On the example of a single aspheric lens, it was shown that a 1:1 focus requires much stricter tolerances than currently achievable. Thus, a multi-lens imaging system was designed, splitting up the lens power into six, where one features an aspheric surface. By performing multiple optimization steps, a robust system was presented, refocusing the light in a plane between the 4 K and 40 K stages. Since the lenses are thin, flexible mounting rings fabricated from EDM processes were constructed. Surrounding them, cells were designed to compensate stress induced by material dependent differential thermal expansion integrals, deforming or breaking the lenses. Furthermore adjustable compensation elements were introduced, which take fabrication tolerances into account. For an aspheric lens element, a radial shift can be performed to account for decentering during fabrication. To ensure a secure, reproducible alignment, the refocusing lens at 40 K was mechanically connected to first lenses by a PEEK mount.

Outside the vacuum, an extendable detection unit was presented, which contains two lens sets, first infinity correcting and finally focusing the emitted photons on a camera and a PMT. The magnification in the image plane is x32. For a usual Be^+ state readout, the number of photons were determined to be ≈ 20, compared to ≈ 15 for the existing system at CryPTEx-SC.

6.1 OUTLOOK

The cryogenic lens system was recently test-assembled **??** and needs to be aligned. Each lens is required to be centered, and the subsequent spacing between each element needs to be determined to model a compensator adjustment and align the 40 K lens along the optical axis. After that, the manipulator has to be aligned on the 4 K stage to account for the depth of focus. An autostigmatic microscope mounted on a precision-grade linear stage can probe these features [188]. Here, a collimated beam emitted, for example, by a helium-neon laser enters a non-polarizing beam splitter.

One arm is then focused by a (diffraction-limited) lens and referenced to an optical axis by observing the back reflections on a camera. This can be determined, for example, by a curved mirror.

By first overlapping the foci, a reference position is defined. After that, the plano-aspheric lens is positioned between the microscope and the mirror. Since it is anti-reflection coated for wavelengths around 313 nm, reflections occur on each surface, such that the microscope focus (MF) is positioned first onto the plane axis, and second such that the aspheric surface focal spot overlaps with the MF. By rotating the lens cell around the optical axis, it can be centered. Subsequently, the lenses are added to the system, and the procedure resets. After all six lenses are assembled, the so-called cat-eye reflections ideally align on the optical axis, leaving only the distances between the lenses as a degree of freedom. Since the contrast is maximized for the MF passing through a surface, with knowledge of the absolute MF position, these distances can be determined. Lastly, the whole microscope focal length can be measured by overlapping the microscope, lens stack, and reference mirror together.

A much simpler approach is the calculation of the required focal lengths at one defined distance to the lens system under probe. With that, a diffractive mask can be fabricated and directly put in front of a Fizeau interferometer [180]. At specified areas on that mask, not only the distance to a lens can be imprinted but also other characteristics, such as the wavefront error for the first aspheric lens.

By applying low coherence interferometry, the surface distances of the whole lens stack can be characterized [189], but a centering measurement requires a second device as stated above.

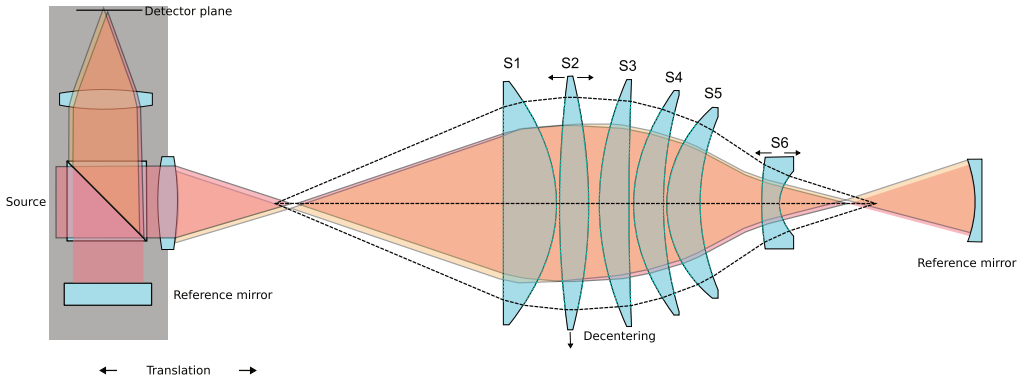

(a)

Figure 43: Sketch of the measurement principle involving a modified version of an autostigmatic microscope.

A APPENDIX

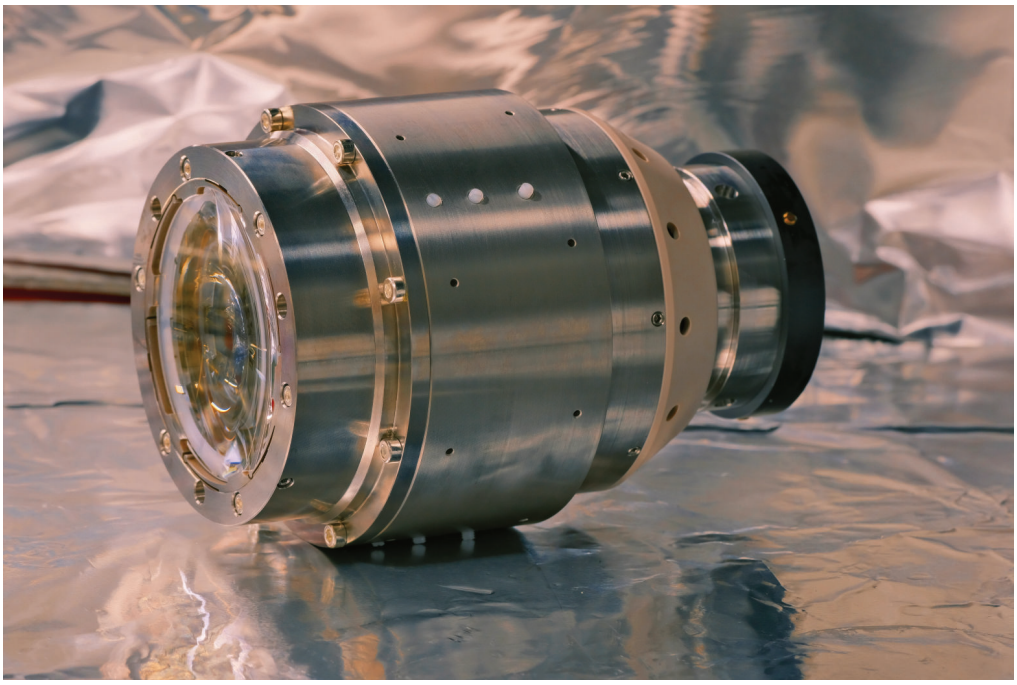

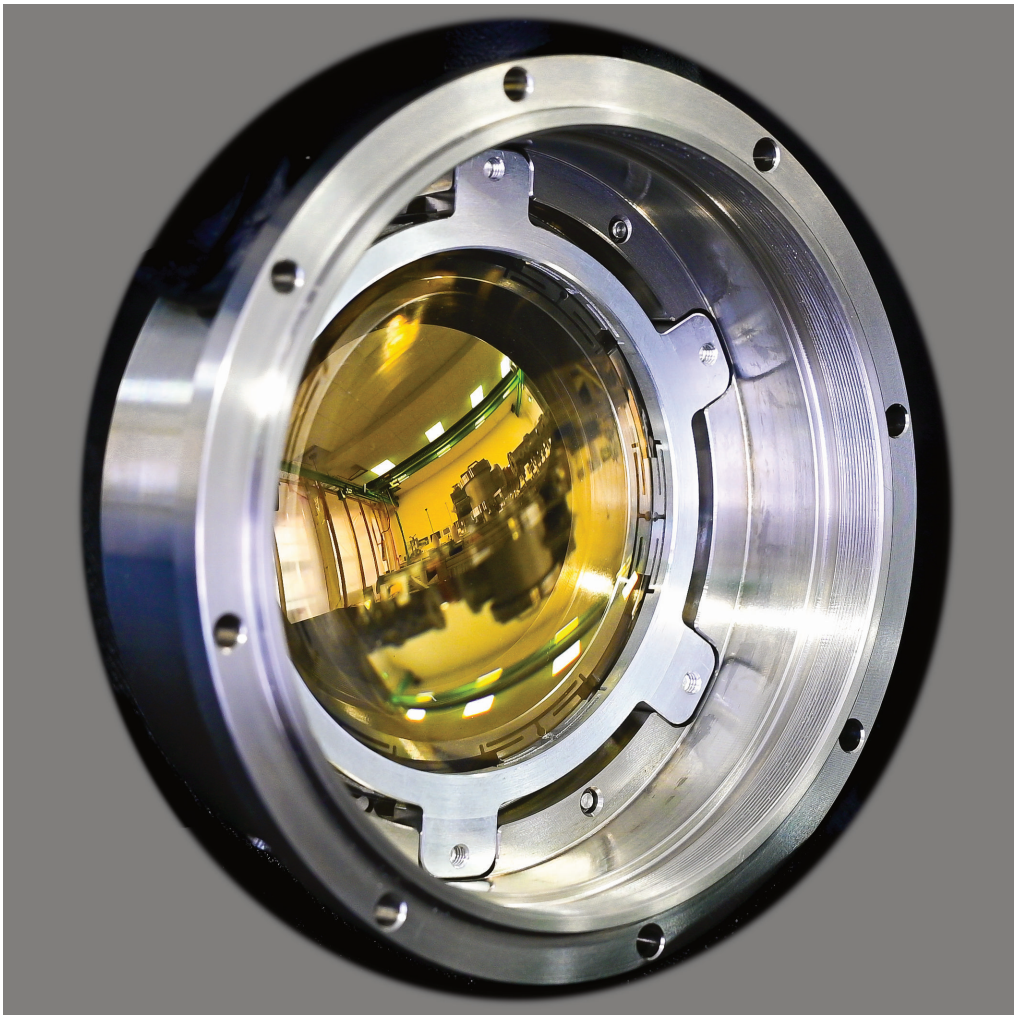

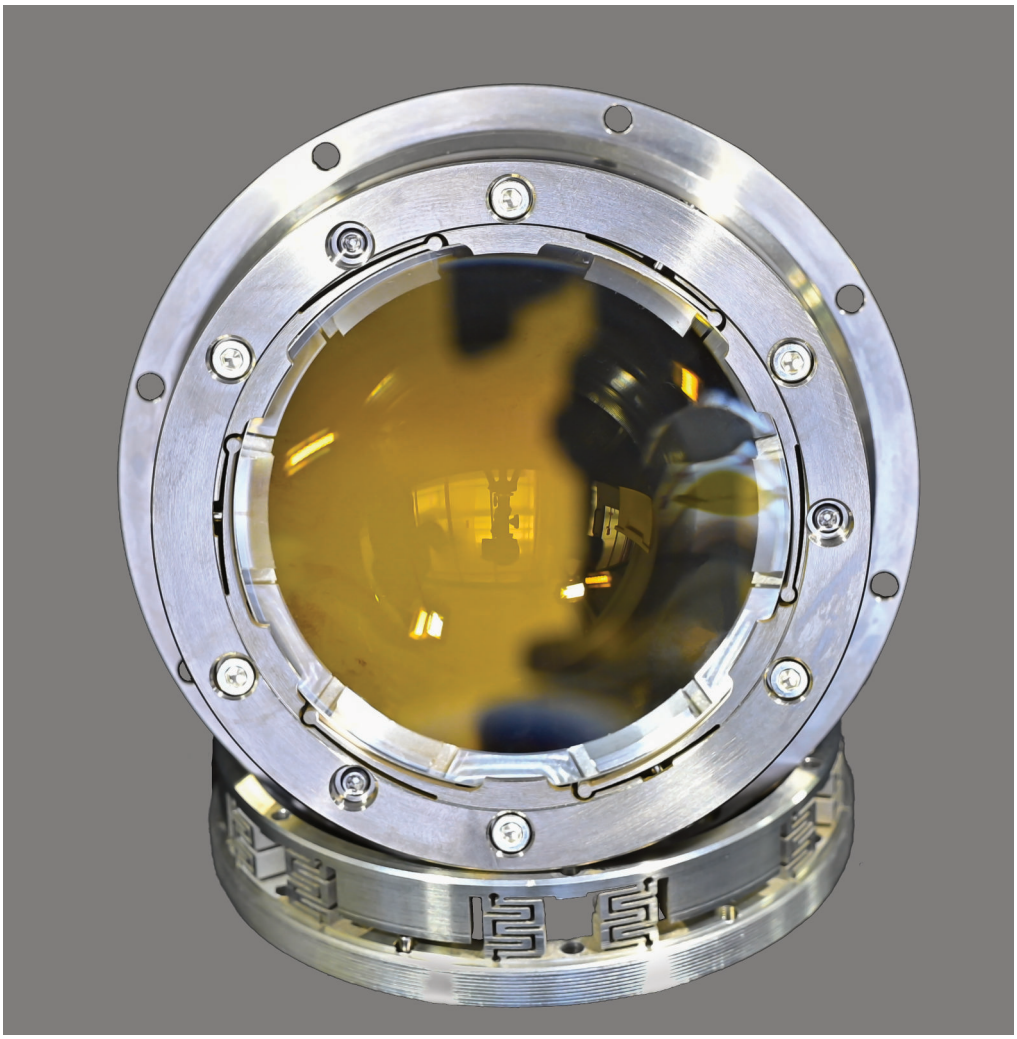

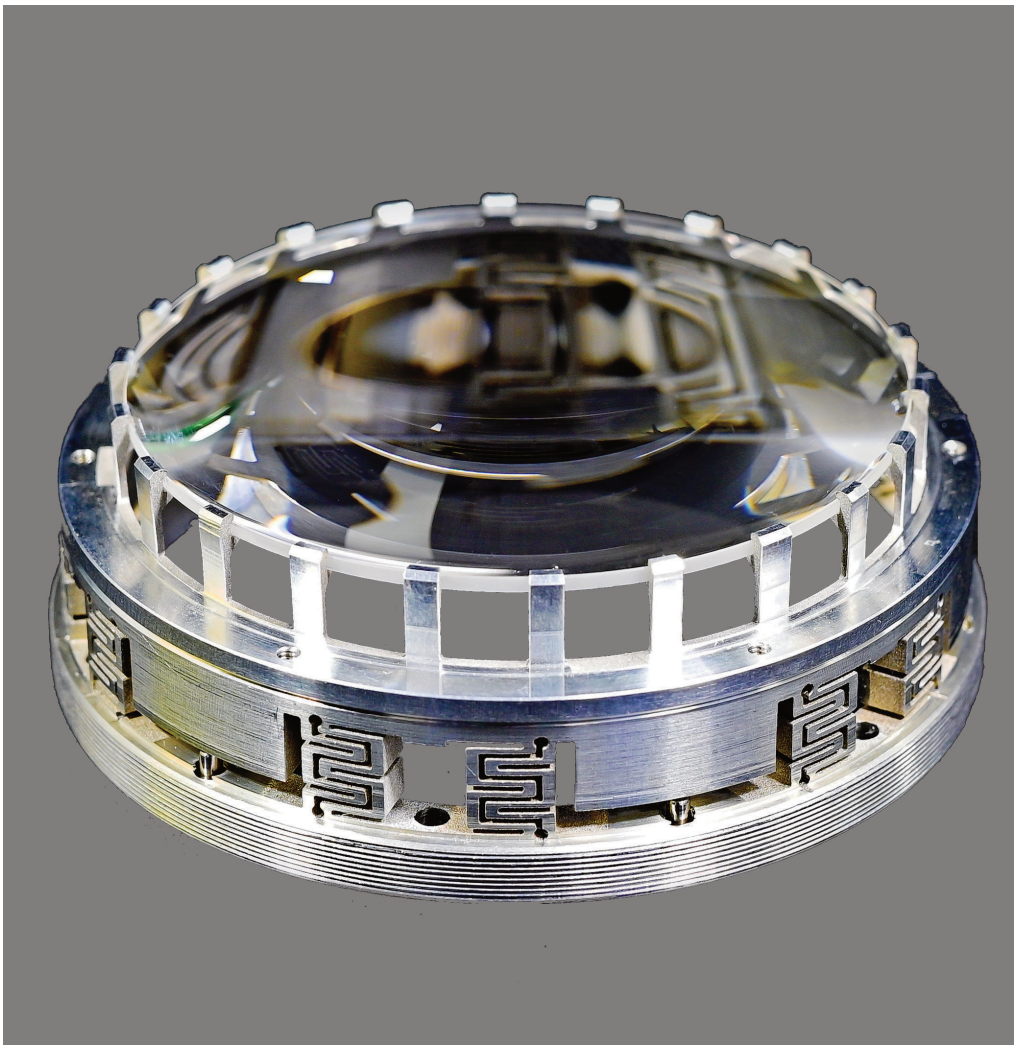

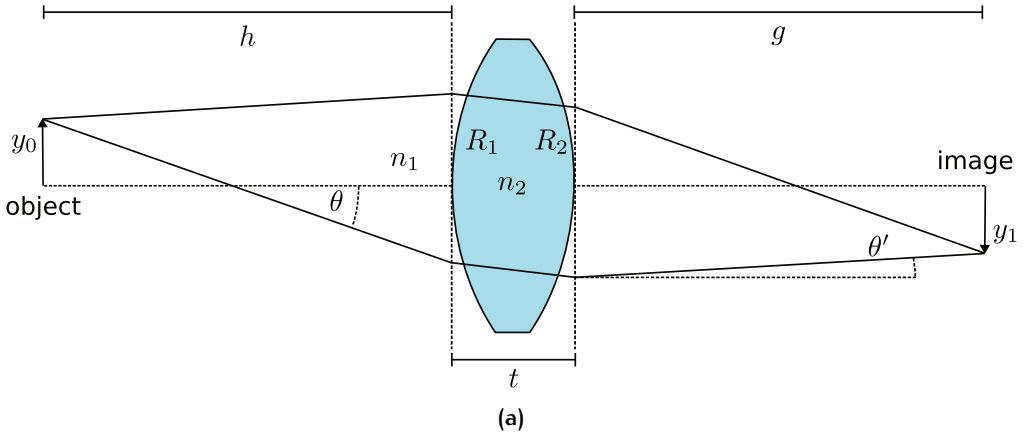

Figure 44: Illustration of the ABCD-matrix formalism.

A.1 ABCD FORMALISM

In this section, the simplest form of a matrix formalism for a single, thick lens with two spherical surfaces is described. The vector of a ray is given by a field height and an angle to the optical axis

$$s = \begin{pmatrix} y \\ \theta \end{pmatrix} \tag{69}$$

For propagation through a surface, the following matrix holds

$$M = \begin{pmatrix} 1 & 0 \\ \frac{n_1 - n_2}{R_1 n_2} & \frac{n_1}{n_2} \end{pmatrix} \tag{70}$$

where n_1, n_2 are the corresponding refractive indices as shown in Figure 44. Propagation at a length d inside a medium is given by

$$M = \begin{pmatrix} 1 & d \\ 0 & 1 \end{pmatrix} \tag{71}$$

That way, an imaging condition for a single lens element is given by:

$$\begin{pmatrix} y_0 \\ \theta \end{pmatrix} \cdot \begin{pmatrix} 1 & g \\ 0 & 1 \end{pmatrix} \cdot \begin{pmatrix} 1 & 0 \\ \frac{n_2 - n_1}{R_2 n_1} & \frac{n_2}{n_1} \end{pmatrix} \cdot \begin{pmatrix} 1 & t \\ 0 & 1 \end{pmatrix} \cdot \begin{pmatrix} 1 & 0 \\ \frac{n_1 - n_2}{R_1 n_2} & \frac{n_1}{n_2} \end{pmatrix} \cdot \begin{pmatrix} 1 & h \\ 0 & 1 \end{pmatrix} = \begin{pmatrix} y_1 \\ \theta' \end{pmatrix} \tag{72}$$

A.2 CaF_2 THERMAL EXPANSION PROPERTIES FROM ROOM TEMPERATURE TO 4K

Similar to UV fused silica (UVFS), literature research on CaF_2 has led to multiple sources for the linear thermal expansion coefficient over the full temperature range [153,190,191]. To describe the data, polynomial fits were used, which only accurately represent the data in a specific region, e.g., 25 – 300K [192]. The fit function given by Equation 63 from [152], which implements a Debye-like model combined with an Einstein model, addresses this limitation. It was purely qualitatively used for thermal related finite-element simulations.

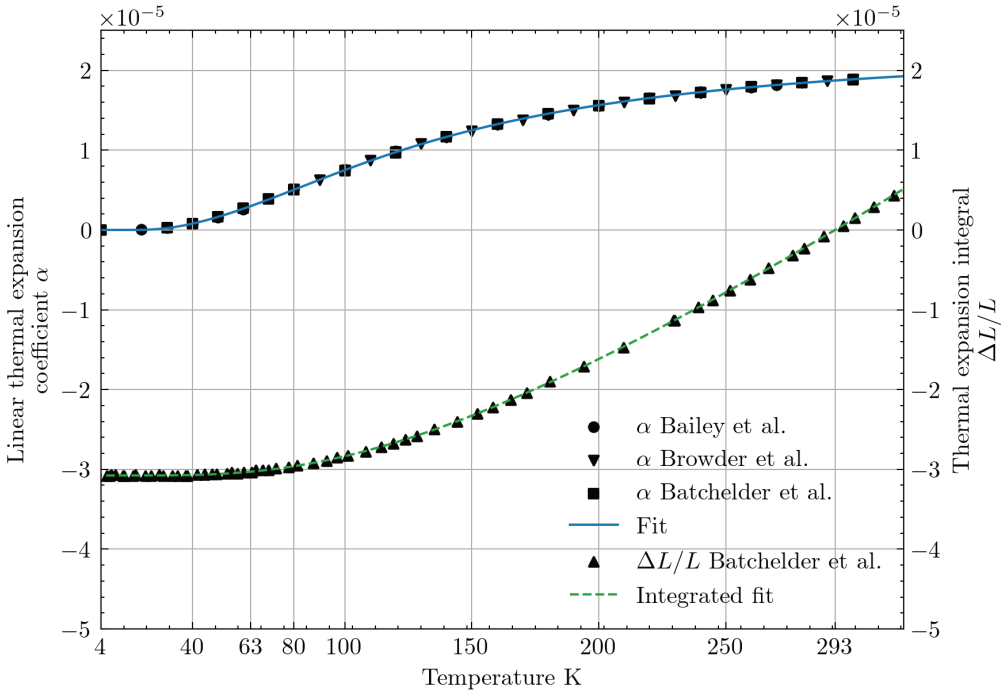

Figure 45: The linear expansion coefficients of calcium fluoride (solid line) and the integrated thermal expansion (dashed line) are presented for low temperatures. The empirical model shown in Equation 63 is taken from [152]. Additionally, the linear thermal expansion coefficients from different sources are plotted [153, 190, 191]. The fitted model, with parameters $a = -3.07 \times 10^{-3}$, $b = 69.418$, $c = 253.175$, $d = -0.0675$, and $e = 4.276$, was used for qualitative investigations in cryogenic mounts with finite element methods. In contrast to standardized polynomial models, this model does not overfit at lower temperatures.

A.3 PARAMETERS OF THE 4K LENS STACK AT ROOM TEMPERATURE

Surface	Radius	Thickness	Material	Clear Radius	Mech Radius
Trap center	-	59.596	Vacuum	-	
Standard	∞	13.750	Corning 7980	28.575	31.75
Aspheric*	-43.556	0.770	Vacuum	28.575	31.75
Standard	238.0	7.550	Corning 7980	29.7	33.00
Standard	-138.0	2.973	Vacuum	29.7	33.00
Standard	76.335	7.750	Corning 7980	29.025	32.25
Standard	955.725	1.150	Vacuum	29.025	32.25
Standard	46.0	7.75	Corning 7980	29.25	29.25
Standard	101.32	0.810	Vacuum	26.325	29.25
Standard	31.93	8.75	Corning 7980	25	25
Standard	57.5	16.051	Vacuum	22.5	25
Standard	75.636	4.5	Corning 7980	12	12
Standard	11.34	25.089	Vacuum	7.6	12

Table 10: List of surfaces and parameters at the 4K stage for room temperature. Each lens element is separated into two surfaces with curvature radius and thickness/distance to the next element. All polished areas on the surfaces are given by the clear surface parameter, while the mechanical radius is the size of the lens.

A.4 PARAMETERS OF THE ROOM TEMPERATURE PROJECTION SYSTEM

A.4.1 Afocal correction lens

Surface	Radius	Thickness	Material	Clear Radius	Mech Radius
Trap center	-	60.0	Vacuum	-	
Standard	55.2	6.2	synth. f-silica	10	15
Standard	-55.2	33.943	Air	10	15
Standard	∞	7.55	synth. f-silica	10	12.7
Standard	-16.1	3.0	Air	10	12.7
Standard	64.4	5.5	synth. f-silica	10	15
Standard	-64.4	62.610	Air	10	15
Standard	-184.0	7.75	synth. f-silica	10	15
Standard	184.0	0.8	Air	10	15
Standard	46.0	-7.0	synth. f-silica	10	15
Standard	-46.0	-23.318	Air	10	15
Standard	32.2	-2	synth. f-silica	10	15
Standard	-32.2	25.04	Air	10	15

Table 11: List of surfaces and parameters for the correction elements at room temperature in the laboratory environment. Each lens element is separated into two surfaces with curvature radius and thickness/distance to the next element. All polished areas on the surfaces are given by the clear surface parameter, while the mechanical radius is the size of the lens. These elements produce afocal projections to allow for more flexibility for refocusing (simultaneously) on detectors with different pixel sizes. All lenses in this table are commercially available and were additionally anti-reflection coated for increased transmission at 313 nm.

A.4.2 EMCCD/PMT focusing optics

Surface	Radius	Thickness	Material	Clear Radius	Mech Radius
Standard	∞	6.2	synth. f-silica	12.5	15.00
Standard	276	33.943	Air	12.5	15.00
Standard	-184	7.55	synth. f-silica	12.5	15.00
Standard	184	3.0	Air	12.5	15.00
Standard	64.4	5.5	synth. f-silica	12.5	15.00
Standard	-64.4	62.610	Air	12.5	15.00
Standard	-184.0	7.75	synth. f-silica	12.5	15.00
Standard	184.0	0.8	Air	12.5	15.00
Standard	46.0	-7.0	synth. f-silica	12.5	15.00
Standard	-46.0	-23.318	Air	12.5	15.00
Standard	32.2	-2	synth. f-silica	12.5	15.00
Standard	-32.2	25.04	Air	12.5	15.00

Table 12: List of surfaces and parameters for the focusing system in the laboratory environment. Each lens element is separated into two surfaces with curvature radius and thickness/distance to the next element. All polished areas on the surfaces are given by the clear surface parameter, while the mechanical radius is the size of the lens. This system projects an incoming infinitely focused beam onto the detectors with a absolute Magnification of M≈ 32. All lenses in this table are commercially available and were additionally anti-reflection coated for increased transmission at 313 nm.

A.5 BI-ASPHERIC LENS OF THE PTB HIGHLY CHARGED ION GROUP

In the following, the design parameters of the Highly Charged Ion Group at the Physikalisch Technische Bundesanstalt Braunschweig (PTB) are presented. For the cryogenic lens design described in this thesis, this lens was utilized to refocus the light from the intermediate image plane between 4 K and 40 K to the laboratory environment. While the centration tolerancing was 2 arcmin, the other parameters are related to the "high-precision finish" on the company website of Asphericon.

Surface	Radius	Thickness	Material	Clear Radius	Mech Radius
Trap center	-	20.0	Vacuum	-	
Standard	26.844407	10.8	Corning 7980	11.2	12.7
Standard	13.283734	95	Vacuum	12.7	12.7
Detector	-	-		-	-

Parameter	Surface 1	Surface 2
κ	-6.49573920	-0.59350853
a_4	-7.6408988618E-6	-1.95647839E-5
a_6	2.3617E-10	-1.6031978811E-8
Detector	-	-

Table 13: This is a list of surfaces and aspheric parameters (a_i) for the PTB-type bi-aspheric lens which was designed by [97] and is mounted on the 40K stage of the CryPTEx-SC experiment as well as used in the imaging system presented in this thesis. All polished areas on the surfaces are represented by the clear surface parameter, while the mechanical radius indicates the lens size. The lens was manufactured by Asphericon and is used for imaging ($^9Be^+$) with a numerical aperture (NA) of 0.45 in cryogenic environments.

A.5.1 Design of a bi-aspheric lens for efficient Ca^+ imaging for the University of Birmingham highly charged ion group

The PTB lens has a design wavelength of 313 nm. At the University of Birmingham, a similar cryogenic experiment to CryPTEx-SC for quantum logic spectroscopy on highly charged californium ions was established, using $^{40}Ca^+$ as the logic ion at 397 nm. With this lens, the working distance is increased to 21 mm, the numerical aperture (NA) is decreased to 0.42, and the back focal length is decreased to 78 mm. Consequently, the following lenses must compensate for the higher transmitted numerical aperture due to the decreased working distance. Furthermore, the diffraction-limited field of view at the maximum NA is reduced to a specific value. For the $^{40}Ca^+$ cooling wavelength, the aforementioned lens was modified, focusing on maintaining the focal length and back focal length at 20 mm and 95 mm, respectively. The diffraction-limited field of view is similar to that of the PTB design at 300 µm, allowing for alignment errors due to manufacturing tolerances of the lens mount along the optical axis. This was achieved by appropriately weighting the desired minimal RMS spot sizes to ensure an even field could be realized. The lens parameters are provided in Table 14.

Surface	Radius	Thickness	Material	Clear Radius	Mech Radius
Trap center	-	20.0	Vacuum	-	
Standard	24.9041	10.8	Corning 7980	11.2	12.7
Standard	13.0816	95	Vacuum	12.7	12.7
Detector	-	-		-	-

Parameter	Surface 1	Surface 2
κ	-7.70325	-0.507708
a_4	-2.01676E-6	2.22385E-5
a_6	-1.98396E-8	4.3297E-8
Detector	-	-

Table 14: List of surfaces and aspheric parameters a_i of the bi-aspheric lens designed by [97], modified for collection photons with wavelength 397 nm corresponding to Ca^+ . All polished areas on the surfaces are given by the clear surface parameter, while the mechanical radius is the lens size.This lens does achieve a NA= 0.45 at a field-of-view of 300 µm.

A.5.2 Design of a bi-aspheric lens for efficient Be^+ imaging at longer backfocus for a conventional trap

Due to the different vacuum chamber dimensions of CryPTEx-SC and the PTB design [90], it is beneficial to increase the back focus of the aspheric lens. The total path length of the light in Table from trap center to intermediate focus is 125.8 mm, which is within the 4 K stage. Thus, the back-focus was elongated in a re-design to allow for inserting an re-entrance window outside the heat shields. As a result, the magnification is slightly increased to $M \approx 5$.

Surface	Radius	Thickness	Material	Clear Radius	Mech Radius
Trap center	-	20.0	Vacuum	-	
Standard	32.505	14.8	Corning 7980	12.7	15.5
Standard	-15.021	160	Vacuum	15.5	15.5
Detector	-	-		-	-

Parameter	Surface 1	Surface 2
κ	-11.948183	-0.64577631
a_4	- 3.6623E-6	3.961858E-6
a_6	-1.021317E-9	5.9787104E-10
Detector	-	-

Table 15: List of surfaces and aspheric parameters a_i of the PTB type bi-aspheric lens [97] modified for a longer back-focus . All polished areas on the surfaces are given by the clear surface parameter, while the mechanical radius is the lens size.This lens does achieve a NA= 0.5 at a diffraction limited field-of-view of 300 µm. Due to the longer back-focus, the magnification factor is increased to $M \approx 5$.

A.6 CATADIOPTRIC LENS FOR IN^+ /YB^+ MIXED CRYSTALS

For testing and illustration purposes in the deeper ultraviolet regime, a catadioptric imaging system for mixed crystals containing In^+ and Yb^+ was optimized at a working distance of 62.469 mm. The transmission efficiency after the obscuration of the secondary mirror is 85%. Details of the system are given in Table 16. The optimized field of view is 500 µm.

Table 16: Parameters for a three element, catadioptric imaging system with NA= 0.4, S = 62.469 mm working distance and 30x magnification. All elements are specified as Corning 79-80 UVFS. Only surface 9 does have a conic constant $\kappa = 0.184$. The system is optimized for two wavelengths, $\lambda_1 = 230$ nm and $\lambda_2 = 369$ nm corresponding to the cooling transitions of In^+ , Yb^+ , while higher wavelength spectrum projects a diffraction limited spotsize for imaging of Ca^+ as well. The elements S2 and S3 do require pinholes of 22 mm to let the beam reflected from Surface 9 pass through.

Element	Surface	Radius /mm	Thickness /mm	Diameter /mm
S1	3 (R1)	-87.431	10.585	55.2
S1	4 (R2)	-77.264	8.126	67.0
S2	5 (R3)	-79.520	6.000	72.0
S2	6 (R4)	-72.089	32.797	80.0
S3	7 (R5)	-66.790	15.000	81.0
S3	8 (R6,r)	-96.631	32.797	100.0
S1	9 (R5,r,c)	-29.301	723.685	22.0

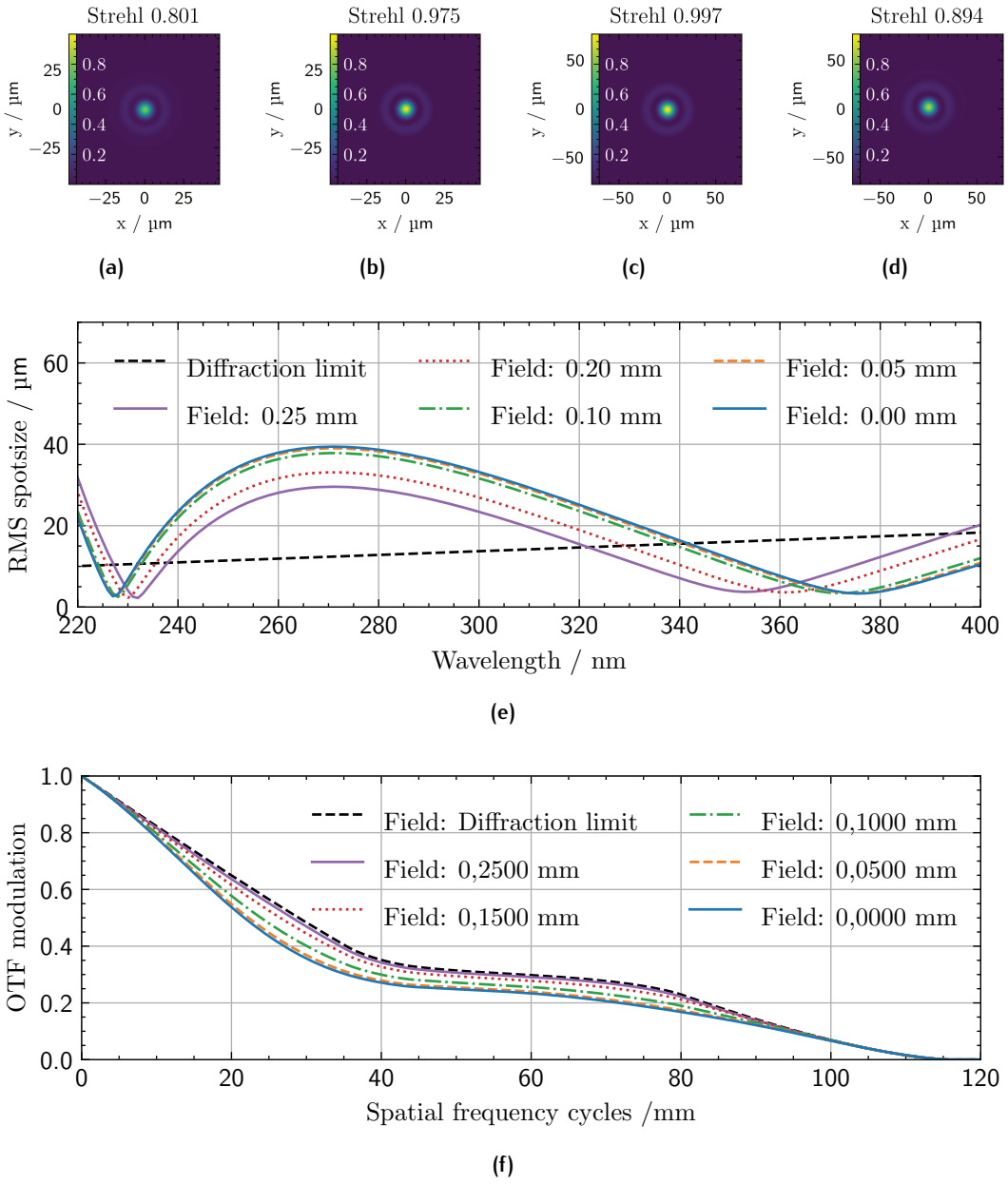

Figure 46: (a,b) simulated point spread functions for In^+ at 230 nm wavelength on-axis (a) and at a field height of 250 µm (b). (c,d) The same for Yb^+ at 369.5 nm. By integrating the point spread function (PSF) of (a-d), 90% of the light emitted by a point source is covered on a diameter of 48 µm for In^+ and 80 µm for Yb^+ over the full field of view. (e) RMS spot size diagram over the wavelength range (220 – 400)nm. The blue line indicates the on-axis field. The system consists of three elements and two reflective surfaces.(f) Modulation transfer function in the focus for In^+ at different heights fields.

G | LIST OF PUBLICATIONS

Elwin A. Dijck, Christian Warnecke, Malte Wehrheim, Ruben B. Henninger, Julia Eff, Kostas Georgiou, Andrea Graf, Stepan Kokh, Lakshmi P. Kozhiparambil Sajith, Christopher Mayo, Vera M. Schäfer, Claudia Volk, Piet O. Schmidt, Thomas Pfeifer, José R. Crespo López-Urrutia; Sympathetically cooled highly charged ions in a radio-frequency trap with superconducting magnetic shielding. Rev. Sci. Instrum. 1 August 2023; 94 (8): 083203.
https://doi.org/10.1063/5.0160537

J. Stark, C. Warnecke, S. Bogen, S. Chen, E. A. Dijck, S. Kühn, M. K. Rosner, A. Graf, J. Nauta, J.-H. Oelmann, L. Schmöger, M. Schwarz, D. Liebert, L. J. Spieß, S. A. King, T. Leopold, P. Micke, P. O. Schmidt, T. Pfeifer, J. R. Crespo López-Urrutia; An ultralow-noise superconducting radio-frequency ion trap for frequency metrology with highly charged ions. Rev. Sci. Instrum. 1 August 2021; 92 (8): 083203.
https://doi.org/10.1063/5.0046569

M. A. Blessenohl, S. Dobrodey, C. Warnecke, M. K. Rosner, L. Graham, S. Paul, T. M. Baumann, Z. Hockenbery, R. Hubele, T. Pfeifer, F. Ames, J. Dilling, J. R. Crespo López-Urrutia; An electron beam ion trap and source for re-acceleration of rare-isotope ion beams at TRIUMF. Rev. Sci. Instrum. 1 May 2018; 89 (5): 052401.
https://doi.org/10.1063/1.5021045

BIBLIOGRAPHY

[1] J. M. Enoch, "Archeological optics: the very first known mirrors and lenses," *Journal of Modern Optics*, vol. 54, pp. 1221–1239, June 2007.

[2] K. Iizuka, *Engineering Optics*. Springer New York, 2008.

[3] M. Zghal, H.-E. Bouali, Z. Ben Lakhdar, and H. Hamam, "The first steps for learning optics: Ibn sahl's, al-haytham's and young's works on refraction as typical examples," in *Tenth International Topical Meeting on Education and Training in Optics and Photonics* (M. Nantel, ed.), vol. 9665, p. 966509, SPIE, Aug. 2015.

[4] S. Dupré, "Galileo's telescope and celestial light," *Journal for the History of Astronomy*, vol. 34, pp. 369–399, Nov. 2003.

[5] J. D. Jackson, "Electrodynamics," Sept. 2007.

[6] D. Clowe, M. Bradač, A. H. Gonzalez, M. Markevitch, S. W. Randall, C. Jones, and D. Zaritsky, "A direct empirical proof of the existence of dark matter," *The Astrophysical Journal*, vol. 648, p. L109–L113, Aug. 2006.

[7] W. Tucker, P. Blanco, S. Rappoport, L. David, D. Fabricant, E. E. Falco, W. Forman, A. Dressler, and M. Ramella, "1e 0657−56: A contender for the hottest known cluster of galaxies," *The Astrophysical Journal*, vol. 496, p. L5–L8, Mar. 1998.

[8] S. W. Randall, M. Markevitch, D. Clowe, A. H. Gonzalez, and M. Bradač, "Constraints on the self-interaction cross section of dark matter from numerical simulations of the merging galaxy cluster 1e 0657−56," *The Astrophysical Journal*, vol. 679, pp. 1173–1180, June 2008.

[9] D. Paraficz, J.-P. Kneib, J. Richard, A. Morandi, M. Limousin, E. Jullo, and J. Martinez, "The bullet cluster at its best: weighing stars, gas, and dark matter," *Astronomy & Astrophysics*, vol. 594, p. A121, Oct. 2016.

[10] J. R. Brownstein and J. W. Moffat, "The bullet cluster 1*e*0657 − 558 evidence shows modified gravity in the absence of dark matter," *Monthly Notices of the Royal Astronomical Society*, vol. 382, pp. 29–47, Nov. 2007.

[11] D. Antypas and the SNOWMASS community, "New horizons: Scalar and vector ultralight dark matter,"

[12] D. Budker, P. W. Graham, H. Ramani, F. Schmidt-Kaler, C. Smorra, and S. Ulmer, "Millicharged dark matter detection with ion traps," *PRX Quantum*, vol. 3, Feb. 2022.

[13] M. Safronova, D. Budker, D. DeMille, D. F. J. Kimball, A. Derevianko, and C. W. Clark, "Search for new physics with atoms and molecules," *Reviews of Modern Physics*, vol. 90, June 2018.

[14] V. A. Dzuba, V. V. Flambaum, and S. Schiller, "Testing physics beyond the standard model through additional clock transitions in neutral ytterbium," *Physical Review A*, vol. 98, Aug. 2018.

[15] Y. Hochberg, Y. F. Kahn, R. K. Leane, S. Rajendran, K. Van Tilburg, T.-T. Yu, and K. M. Zurek, "New approaches to dark matter detection," *Nature Reviews Physics*, vol. 4, pp. 637–641, Sept. 2022.

[16] A. Aeppli, K. Kim, W. Warfield, M. S. Safronova, and J. Ye, "Clock with 8×10^{-19} systematic uncertainty," *Physical Review Letters*, vol. 133, jul 2024.

[17] J.-P. Uzan, "Varying Constants, Gravitation and Cosmology," *Living Reviews in Relativity*, vol. 14, Mar. 2011.

[18] S. G. Karshenboim, "Search for a possible variation of the fine structure constant," *General Relativity and Gravitation*, vol. 38, pp. 159–182, Jan. 2006.

[19] M. Kozlov, M. Safronova, J. C. López-Urrutia, and P. Schmidt, "Highly-charged ions: Optical clocks and applications in fundamental physics," *Reviews of Modern Physics*, vol. 90, dec 2018.

[20] M. Filzinger, S. Dörscher, R. Lange, J. Klose, M. Steinel, E. Benkler, E. Peik, C. Lisdat, and N. Huntemann, "Improved limits on the coupling of ultralight bosonic dark matter to photons from optical atomic clock comparisons," *Physical Review Letters*, vol. 130, June 2023.

[21] V. V. Flambaum and V. A. Dzuba, "Search for variation of the fundamental constants in atomic, molecular, and nuclear spectra," *Canadian Journal of Physics*, vol. 87, pp. 25–33, Jan. 2009.

[22] A. Arvanitaki, J. Huang, and K. Van Tilburg, "Searching for dilaton dark matter with atomic clocks," *Physical Review D*, vol. 91, Jan. 2015.

[23] P. Touboul *et al.*, "MICROSCOPE mission: Final results of the test of the equivalence principle," *Physical Review Letters*, vol. 129, Sept. 2022.

[24] K. Beloy *et al.*, "Frequency ratio measurements at 18-digit accuracy using an optical clock network," *Nature*, vol. 591, pp. 564–569, Mar. 2021.

[25] W. Quint, *Fundamental Physics in Particle Traps*. Springer Berlin Heidelberg, 2014.

[26] J. C. Berengut, V. A. Dzuba, V. V. Flambaum, and A. Ong, "Highly charged ions with e1, m1, and e2 transitions within laser range," *Physical Review A*, vol. 86, Aug. 2012.

[27] D. Wineland, C. Monroe, W. Itano, D. Leibfried, B. King, and D. Meekhof, "Experimental issues in coherent quantum-state manipulation of trapped atomic ions," *Journal of Research of the National Institute of Standards and Technology*, vol. 103, p. 259, May 1998.

[28] J. D. Gillaspy, "Highly charged ions," *Journal of Physics B: Atomic, Molecular and Optical Physics*, vol. 34, p. R93–R130, Sept. 2001.

[29] S. Schiller, "Hydrogenlike highly charged ions for tests of the time independence of fundamental constants," *Physical Review Letters*, vol. 98, Apr. 2007.

[30] J. C. Berengut, V. A. Dzuba, and V. V. Flambaum, "Enhanced laboratory sensitivity to variation of the fine-structure constant using highly charged ions," *Physical Review Letters*, vol. 105, Sept. 2010.

[31] J. C. Berengut, V. A. Dzuba, V. V. Flambaum, and A. Ong, "Electron-hole transitions in multiply charged ions for precision laser spectroscopy and searching for variations in α," *Physical Review Letters*, vol. 106, May 2011.

[32] J. C. Berengut, V. A. Dzuba, V. V. Flambaum, and A. Ong, "Optical transitions in highly charged californium ions with high sensitivity to variation of the fine-structure constant," *Physical Review Letters*, vol. 109, Aug. 2012.

[33] S. G. Porsev, U. I. Safronova, M. S. Safronova, P. O. Schmidt, A. I. Bondarev, M. G. Kozlov, I. I. Tupitsyn, and C. Cheung, "Optical clocks based on the cf15+ and cf17+ ions," *Physical Review A*, vol. 102, July 2020.

[34] Barontini *et al.*, "Qsnet, a network of clock for measuring the stability of fundamental constants," in *Quantum Technology: Driving Commercialisation of an Enabling Science II* (K. Bongs, M. J. Padgett, A. Fedrizzi, and A. Politi, eds.), p. 19, SPIE, Oct. 2021.

[35] J. Nauta, A. Borodin, H. B. Ledwa, J. Stark, M. Schwarz, L. Schmöger, P. Micke, J. R. C. López-Urrutia, and T. Pfeifer, "Towards precision measurements on highly charged ions using a high harmonic generation frequency comb," *Nuclear Instruments and Methods in Physics Research Section B: Beam Interactions with Materials and Atoms*, vol. 408, pp. 285–288, oct 2017.

[36] Y.-M. Yu, B. K. Sahoo, and B.-B. Suo, "Highly charged ion (hci) clocks: Frontier candidates for testing variation of fine-structure constant," *Frontiers in Physics*, vol. 11, Feb. 2023.

[37] C. Lyu, C. H. Keitel, and Z. Harman, "Ultrastable and ultra-accurate clock transitions in open-shell highly charged ions," *Communications Physics*, vol. 8, Jan. 2025.

[38] J. C. Berengut, C. Delaunay, A. Geddes, and Y. Soreq, "Generalized king linearity and new physics searches with isotope shifts," *Physical Review Research*, vol. 2, Dec. 2020.

[39] J. C. Berengut and C. Delaunay, "Precision isotope-shift spectroscopy for new physics searches and nuclear insights," *Nature Reviews Physics*, Jan. 2025.

[40] A. Wilzewski, L. I. Huber, M. Door, J. Richter, A. Mariotti, L. J. Spieß, M. Wehrheim, S. Chen, S. A. King, P. Micke, M. Filzinger, M. R. Steinel, N. Huntemann, E. Benkler, P. O. Schmidt, J. Flannery, R. Matt, M. Stadler, R. Oswald, F. Schmid, D. Kienzler, J. Home, D. P. L. A. Craik, S. Eliseev, P. Filianin, J. Herkenhoff, K. Kromer, K. Blaum, V. A. Yerokhin, I. A. Valuev, N. S. Oreshkina, C. Lyu, S. Banerjee, C. H. Keitel, Z. Harman, J. C. Berengut, A. Viatkina, J. Gilles, A. Surzhykov, M. K. Rosner, J. R. C. López-Urrutia, and E. Fuchs, "Nonlinear calcium king plot constrains new bosons and nuclear properties," 2024.

[41] K. Ono, Y. Saito, T. Ishiyama, T. Higomoto, T. Takano, Y. Takasu, Y. Yamamoto, M. Tanaka, and Y. Takahashi, "Observation of nonlinearity of generalized king plot in the search for new boson," *Physical Review X*, vol. 12, May 2022.

[42] M. K. Rosner, "Electronic energy level determination in the 4f-subshell in highly charged lead and the 5d-subshell in highly charged bismuth by atomic structure calculation-assisted optical spectroscopy," 2024.

[43] J. Schweppe, A. Belkacem, L. Blumenfeld, N. Claytor, B. Feinberg, H. Gould, V. E. Kostroun, L. Levy, S. Misawa, J. R. Mowat, and M. H. Prior, "Measurement of the lamb shift in lithiumlike uranium u89+," *Physical Review Letters*, vol. 66, pp. 1434–1437, Mar. 1991.

[44] H. F. Beyer, G. Menzel, D. Liesen, A. Gallus, F. Bosch, R. Deslattes, P. Indelicato, T. Stöhlker, O. Klepper, R. Moshammer, F. Nolden, H. Eickhoff, B. Franzke, and M. Steck, "Measurement of the ground-state lambshift of hydrogenlike uranium at the electron cooler of the esr," *Zeitschrift für Physik D Atoms, Molecules and Clusters*, vol. 35, pp. 169–175, Sept. 1995.

[45] E. S. Marmar, J. E. Rice, K. Kallne, J. Kallne, and R. E. LaVilla, "Precision measurement of the 1slamb shift in hydrogenlike argon," *Physical Review A*, vol. 33, pp. 774–777, Jan. 1986.

[46] E. D. Donets, V. I. Ilyushchenko, and V. A. Alpert, "Ultrahigh vacuum electron beam soruce of highly stripped ions.," *Premiere Conference Internationale sur les Sources d'Ions, 18–20 Juin 1969*, June 1970.

[47] M. A. Blessenohl, S. Dobrodey, C. Warnecke, M. K. Rosner, L. Graham, S. Paul, T. M. Baumann, Z. Hockenbery, R. Hubele, T. Pfeifer, F. Ames, J. Dilling, and J. R. Crespo López-Urrutia, "An electron beam ion trap and source for reacceleration of rare-isotope ion beams at triumf," *Review of Scientific Instruments*, vol. 89, May 2018.

[48] M. A. Levine, R. E. Marrs, J. R. Henderson, D. A. Knapp, and M. B. Schneider, "The electron beam ion trap: A new instrument for atomic physics measurements," *Physica Scripta*, vol. T22, pp. 157–163, Jan. 1988.

[49] P. Beiersdorfer, E. Behar, K. Boyce, G. Brown, H. Chen, K. Gendreau, A. Graf, M.-F. Gu, C. Harris, S. Kahn, R. Kelley, J. Lepson, M. May, P. Neill, E. Pinnington, F. Porter, A. Smith, C. Stahle, A. Szymkowiak, A. Tillotson, D. Thorn, E. Träbert, and B. Wargelin, "Overview of the livermore electron beam ion trap project," *Nuclear Instruments and Methods in Physics Research Section B: Beam Interactions with Materials and Atoms*, vol. 205, pp. 173–177, May 2003.

[50] I. Draganić, J. R. C. López-Urrutia, R. DuBois, S. Fritzsche, V. M. Shabaev, R. S. Orts, I. I. Tupitsyn, Y. Zou, and J. Ullrich, "High Precision Wavelength Measurements of QED-Sensitive Forbidden Transitions in Highly Charged Argon Ions," *Physical Review Letters*, vol. 91, Oct. 2003.

[51] R. S. Orts, Z. Harman, J. R. C. López-Urrutia, A. N. Artemyev, H. Bruhns, A. J. G. Martínez, U. D. Jentschura, C. H. Keitel, A. Lapierre, V. Mironov, V. M. Shabaev, H. Tawara, I. I. Tupitsyn, J. Ullrich, and A. V. Volotka, "Exploring relativistic many-body recoil effects in highly charged ions," *Physical Review Letters*, vol. 97, Sept. 2006.

[52] V. Mäckel, R. Klawitter, G. Brenner, J. R. Crespo López-Urrutia, and J. Ullrich, "Laser Spectroscopy on Forbidden Transitions in Trapped Highly Charged Ar^{13+} Ions," *Physical Review Letters*, vol. 107, Sept. 2011.

[53] R. Jertz, G. Bollen, H. J. Kluge, L. Schweikhard, H. Stolzenberg, I. Bergström, C. Carlberg, and R. Schuch, "Highly-charged ions in a penning trap: mass measurements, etc.," *Zeitschrift für Physik D Atoms, Molecules and Clusters*, vol. 21, p. S179–S180, Mar. 1991.

[54] T. Beier, L. Dahl, H.-J. Kluge, C. Kozhuharov, and W. Quint, "Trapping ions of hydrogen-like uranium: The hitrap project at gsi," *Nuclear Instruments and Methods in Physics Research Section B: Beam Interactions with Materials and Atoms*, vol. 235, pp. 473–478, July 2005.

[55] J. Repp, C. Böhm, J. R. Crespo López-Urrutia, A. Dörr, S. Eliseev, S. George, M. Goncharov, Y. N. Novikov, C. Roux, S. Sturm, S. Ulmer, and K. Blaum, "Pentatrap: a novel cryogenic multi-penning-trap experiment for high-precision mass measurements on highly charged ions," *Applied Physics B*, vol. 107, pp. 983–996, Jan. 2012.

[56] A. A. Kwiatkowski, J. Dilling, S. Malbrunot-Ettenauer, and M. P. Reiter, "15 years of precision mass measurements at titan," *The European Physical Journal A*, vol. 60, Apr. 2024.

[57] M. Schwarz, J. R. C. López-Urrutia, F. R. Brunner, T. Ballance, M. Drewsen, P. O. Schmidt, and J. Ullrich, "A cryogenic Paul Trap for Highly Charged Ions and Molecular Ions," *Journal of Physics: Conference Series*, vol. 388, p. 122005, nov 2012.

[58] L. Schmöger, M. Schwarz, T. M. Baumann, O. O. Versolato, B. Piest, T. Pfeifer, J. Ullrich, P. O. Schmidt, and J. R. C. López-Urrutia, "Deceleration, precooling, and multi-pass stopping of highly charged ions in Be+ Coulomb crystals," *Review of Scientific Instruments*, vol. 86, p. 103111, oct 2015.

[59] L. Schmöger, O. O. Versolato, M. Schwarz, M. Kohnen, A. Windberger, B. Piest, S. Feuchtenbeiner, J. Pedregosa-Gutierrez, T. Leopold, P. Micke, A. K. Hansen, T. M. Baumann, M. Drewsen, J. Ullrich, P. O. Schmidt, and J. R. C. López-Urrutia, "Coulomb crystallization of highly charged ions," *Science*, vol. 347, pp. 1233–1236, Mar. 2015.

[60] D. Wineland, P. Ekstrom, and H. Dehmelt, "Monoelectron oscillator," *Physical Review Letters*, vol. 31, pp. 1279–1282, Nov. 1973.

[61] W. Paul and H. Steinwedel, "Notizen: Ein neues Massenspektrometer ohne Magnetfeld," *Zeitschrift fuer Naturforschung A*, vol. 8, jan 1953.

[62] W. Paul and M. Raether, "Das elektrische Massenfilter," *Zeitschrift fuer Physik*, vol. 140, pp. 262–273, may 1955.

[63] W. Paul, H. P. Reinhard, and U. von Zahn, "Das elektrische Massenfilter als Massenspektrometer und Isotopentrenner," *Zeitschrift fuer Physik*, vol. 152, pp. 143–182, apr 1958.

[64] Y. B. Zel'dovich, "Cooling with the aid of high-frequency energy," *ZhETF Pisma Redaktsiiu*, vol. 19, pp. 74–75, 1974.

[65] D. J. Wineland and W. M. Itano, "Laser cooling of atoms," *Physical Review A*, vol. 20, pp. 1521–1540, Oct. 1979.

[66] J. J. Bollinger, J. D. Prestage, W. M. Itano, and D. J. Wineland, "Laser-cooled-atomic frequency standard," *Physical Review Letters*, vol. 54, pp. 1000–1003, Mar. 1985.

[67] F. Diedrich, J. C. Bergquist, W. M. Itano, and D. J. Wineland, "Laser cooling to the zero-point energy of motion," *Physical Review Letters*, vol. 62, pp. 403–406, Jan. 1989.

[68] C. Monroe, D. M. Meekhof, B. E. King, S. R. Jefferts, W. M. Itano, D. J. Wineland, and P. Gould, "Resolved-sideband raman cooling of a bound atom to the 3d zero-point energy," *Physical Review Letters*, vol. 75, pp. 4011–4014, Nov. 1995.

[69] P. O. Schmidt, T. Rosenband, C. Langer, W. M. Itano, J. C. Bergquist, and D. J. Wineland, "Spectroscopy using quantum logic," *Science*, vol. 309, pp. 749–752, July 2005.

[70] P. Micke, T. Leopold, S. A. King, E. Benkler, L. J. Spieß, L. Schmöger, M. Schwarz, J. R. Crespo López-Urrutia, and P. O. Schmidt, "Coherent laser spectroscopy of highly charged ions using quantum logic," *Nature*, vol. 578, pp. 60–65, Jan. 2020.

[71] S. A. King, L. J. Spieß, P. Micke, A. Wilzewski, T. Leopold, E. Benkler, R. Lange, N. Huntemann, A. Surzhykov, V. A. Yerokhin, J. R. Crespo López-Urrutia, and P. O. Schmidt, "An optical atomic clock based on a highly charged ion," *Nature*, vol. 611, pp. 43–47, Nov. 2022.

[72] J. Stark, *An Ultralow-Noise Superconducting Radio-Frequency Ion Trap for Frequency Metrology with Highly Charged Ions*. PhD thesis, 2020.

[73] E. A. Dijck, C. Warnecke, M. Wehrheim, R. B. Henninger, J. Eff, K. Georgiou, A. Graf, S. Kokh, L. P. Kozhiparambil Sajith, C. Mayo, V. M. Schäfer, C. Volk, P. O. Schmidt, T. Pfeifer, and J. R. Crespo López-Urrutia, "Sympathetically cooled highly charged ions in a radio-frequency trap with superconducting magnetic shielding," *Review of Scientific Instruments*, vol. 94, Aug. 2023.

[74] A. Kramida, Yu. Ralchenko, J. Reader, and and NIST ASD Team, "NIST Atomic Spectra Database (ver. 5.12). National Institute of Standards and Technology, Gaithersburg, MD.," 2024.

[75] N. Shiga, W. M. Itano, and J. J. Bollinger, "Diamagnetic correction to the $^{9}be^{+}$ ground-state hyperfine constant," *Physical Review A*, vol. 84, July 2011.

[76] J. D. Jackson, *Classical Electrodynamics*. Wiley, Apr. 1999.

[77] D. Leibfried, R. Blatt, C. Monroe, and D. Wineland, "Quantum dynamics of single trapped ions," *Reviews of Modern Physics*, vol. 75, pp. 281–324, Mar. 2003.

[78] L. Schmöger, "Kalte hochgeladene Ionen für Frequenzmetrologie," 2017.

[79] J. B. Wübbena, S. Amairi, O. Mandel, and P. O. Schmidt, "Sympathetic cooling of mixed-species two-ion crystals for precision spectroscopy," *Physical Review A*, vol. 85, Apr. 2012.

[80] R. C. Thompson, "Ion coulomb crystals," *Contemporary Physics*, vol. 56, pp. 63–79, Jan. 2015.

[81] S. Stenholm, "The semiclassical theory of laser cooling," *Reviews of Modern Physics*, vol. 58, pp. 699–739, July 1986.

[82] N. F. Ramsey, "A molecular beam resonance method with separated oscillating fields," *Physical Review*, vol. 78, pp. 695–699, June 1950.

[83] E. L. Hahn, "Spin echoes," *Physical Review*, vol. 80, pp. 580–594, Nov. 1950.

[84] J. Stark, C. Warnecke, S. Bogen, S. Chen, E. A. Dijck, S. Kühn, M. K. Rosner, A. Graf, J. Nauta, J.-H. Oelmann, L. Schmöger, M. Schwarz, D. Liebert, L. J. Spieß, S. A. King, T. Leopold, P. Micke, P. O. Schmidt, T. Pfeifer, and J. R. Crespo López-Urrutia, "An ultralow-noise superconducting radio-frequency ion trap for frequency metrology with highly charged ions," *Review of Scientific Instruments*, vol. 92, Aug. 2021.

[85] P. Micke, S. Kühn, L. Buchauer, J. R. Harries, T. M. Bücking, K. Blaum, A. Cieluch, A. Egl, D. Hollain, S. Kraemer, T. Pfeifer, P. O. Schmidt, R. X. Schüssler, C. Schweiger, T. Stöhlker, S. Sturm, R. N. Wolf, S. Bernitt, and J. R. C. López-Urrutia, "The Heidelberg compact electron beam ion traps," *Review of Scientific Instruments*, vol. 89, p. 063109, jun 2018.

[86] M. K. Rosner, "Production and preparation of highly charged ions for re-trapping in ultra-cold environments," Master's thesis, Ruprecht-Karls-Universität Heidelberg, 2019.

[87] C. Schweiger, C. M. König, J. R. Crespo López-Urrutia, M. Door, H. Dorrer, C. E. Düllmann, S. Eliseev, P. Filianin, W. Huang, K. Kromer, P. Micke,

M. Müller, D. Renisch, A. Rischka, R. X. Schüssler, and K. Blaum, "Production of highly charged ions of rare species by laser-induced desorption inside an electron beam ion trap," *Review of Scientific Instruments*, vol. 90, Dec. 2019.

[88] P. Mandal, G. Sikler, and M. Mukherjee, "Simulation study and analysis of a compact einzel lens-deflector for low energy ion beam," *Journal of Instrumentation*, vol. 6, p. P02004–P02004, Feb. 2011.

[89] M. Schwarz, O. O. Versolato, A. Windberger, F. R. Brunner, T. Ballance, S. N. Eberle, J. Ullrich, P. O. Schmidt, A. K. Hansen, A. D. Gingell, M. Drewsen, and J. R. C. López-Urrutia, "Cryogenic linear Paul trap for cold highly charged ion experiments," *Review of Scientific Instruments*, vol. 83, p. 083115, aug 2012.

[90] P. Micke, J. Stark, S. A. King, T. Leopold, T. Pfeifer, L. Schmöger, M. Schwarz, L. J. Spieß, P. O. Schmidt, and J. R. C. López-Urrutia, "Closed-cycle, low-vibration 4 K cryostat for ion traps and other applications," *Review of Scientific Instruments*, vol. 90, p. 065104, jun 2019.

[91] J. Ekin, *Experimental Techniques for Low-Temperature Measurements: Cryostat Design, Material Properties and Superconductor Critical-Current Testing*. Oxford University PressOxford, Oct. 2006.

[92] S. M. Wasim and N. H. Zebouni, "Thermal conductivity of superconducting niobium," *Physical Review*, vol. 187, pp. 539–548, Nov. 1969.

[93] S. Kokh, "Ground state cooling of a single beryllium ion in a superconducting paul trap," Master's thesis, Ruprecht-Karls-Universität, Heidelberg, 2024.

[94] P. Kulik, G. Kasprowicz, and M. Gąska, "Driver module for quantum computer experiments: Kasli," in *Photonics Applications in Astronomy, Communications, Industry, and High-Energy Physics Experiments 2018* (R. S. Romaniuk and M. Linczuk, eds.), p. 223, SPIE, Oct. 2018.

[95] Ion Storage Group, "ARTIQ (Advanced Real-Time Infrastructure for Quantum Physics)," 2017.

[96] G. Kasprowicz, T. Harty, S. Bourdeauducq, R. Jördens, D. Allcock, D. Nadlinger, J. W. Britton, A. Sotirova, and D. Nowicka, "Urukul – open-source frequency synthesizer module for quantum physics," *International Journal of Electronics and Telecommunications*, pp. 123–128, Dec. 2021.

[97] T. Leopold, *A cryogenic ion trap system for quantum logic spectroscopy of highly charged ions.* PhD thesis, QUEST Institute for Experimental Quantum Metrology, PTB-Braunschweig, 2018.

[98] T. Leopold, S. A. King, P. Micke, A. Bautista-Salvador, J. C. Heip, C. Ospelkaus, J. R. Crespo López-Urrutia, and P. O. Schmidt, "A cryogenic radio-frequency ion trap for quantum logic spectroscopy of highly charged ions," *Review of Scientific Instruments*, vol. 90, July 2019.

[99] P. C. Holz, K. Lakhmanskiy, D. Rathje, P. Schindler, Y. Colombe, and R. Blatt, "Electric-field noise in a high-temperature superconducting surface ion trap," *Physical Review B*, vol. 104, Aug. 2021.

[100] Y. Tsuchimoto, I. Nakamura, S. Shirai, and A. Noguchi, "Superconducting surface trap chips for microwave-driven trapped ions," *EPJ Quantum Technology*, vol. 11, Sept. 2024.

[101] S. X. Wang, Y. Ge, J. Labaziewicz, E. Dauler, K. Berggren, and I. L. Chuang, "Superconducting microfabricated ion traps," *Applied Physics Letters*, vol. 97, Dec. 2010.

[102] W. P. D. Barna, Masaki Hori, "Superconducting paul trap for antiprotons," in *14th International conference on RF Superconductivity*, 2009.

[103] *Proceedings of the Royal Society of London. Series A - Mathematical and Physical Sciences*, vol. 149, pp. 71–88, Mar. 1935.

[104] E. A. Dijck, "Private communication.".

[105] M. Tinkham, *Introduction to superconductivity*. Dover Publications Inc., 2 ed., 2004.

[106] J. Jaroszynski, "Race against time: resistance of superconducting joints measurements," *Superconductor Science and Technology*, vol. 28, p. 010501, Dec. 2014.

[107] X. H. Li, L. Y. Ye, Z. S. Gao, D. L. Wang, L. Z. Lin, G. M. Zhang, S. T. Dai, Y. W. Ma, and L. Y. Xiao, "Close circuit test of mgb2coil with superconducting joints and a persistent current switch," *Journal of Physics: Conference Series*, vol. 234, p. 022020, June 2010.

[108] T. Monz, *Quantum information processing beyond ten ion-qubits*. PhD thesis, Faculty of Mathematics, Computer Science, and Physics of the Leopold-Franzens University of Innsbruck, 2011.

[109] T. Ruster, C. T. Schmiegelow, H. Kaufmann, C. Warschburger, F. Schmidt-Kaler, and U. G. Poschinger, "A long-lived zeeman trapped-ion qubit," *Applied Physics B*, vol. 122, Sept. 2016.

[110] T. Matsushita, *Flux Pinning of superconductors*. Springer Berlin Heidelberg, 2007.

[111] H. Padamsee, J. Knobloch, and T. Hays, *RF Superconductivity for Accelerators*. Wiley-VCH, Berlin, 2008.

[112] P. Dhakal, G. Ciovati, U. Pudasaini, S. Chetri, S. Balachandran, and P. Lee, "Surface characterization of nitrogen-doped high purity niobium coupons compared with superconducting rf cavity performance," *Physical Review Accelerators and Beams*, vol. 22, Dec. 2019.

[113] W. Alt, "An objective lens for efficient fluorescence detection of single atoms," *Optik*, vol. 113, no. 3, pp. 142–144, 2002.

[114] R. Noek, G. Vrijsen, D. Gaultney, E. Mount, T. Kim, P. Maunz, and J. Kim, "High speed, high fidelity detection of an atomic hyperfine qubit," *Opt Lett*, vol. 38, p. 4735, nov 2013.

[115] A. VanDevender, Y. Colombe, J. Amini, D. Leibfried, and D. Wineland, "Efficient fiber optic detection of trapped ion fluorescence," *Physical Review Letters*, vol. 105, July 2010.

[116] D. H. Slichter, V. B. Verma, D. Leibfried, R. P. Mirin, S. W. Nam, and D. J. Wineland, "Uv-sensitive superconducting nanowire single photon detectors for integration in an ion trap," *Optics Express*, vol. 25, p. 8705, Apr. 2017.

[117] S. Todaro, V. Verma, K. McCormick, D. Allcock, R. Mirin, D. Wineland, S. Nam, A. Wilson, D. Leibfried, and D. Slichter, "State readout of a trapped ion qubit using a trap-integrated superconducting photon detector," *Physical Review Letters*, vol. 126, Jan. 2021.

[118] B. Hampel, D. H. Slichter, D. Leibfried, R. P. Mirin, S. W. Nam, and V. B. Verma, "Trap-integrated superconducting nanowire single-photon detectors with improved rf tolerance for trapped-ion qubit state readout," *Applied Physics Letters*, vol. 122, Apr. 2023.

[119] M. K. Akhlaghi, E. Schelew, and J. F. Young, "Waveguide integrated superconducting single-photon detectors implemented as near-perfect absorbers of coherent radiation," *Nature Communications*, vol. 6, Sept. 2015.

[120] J. Chang, J. W. N. Los, J. O. Tenorio-Pearl, N. Noordzij, R. Gourgues, A. Guardiani, J. R. Zichi, S. F. Pereira, H. P. Urbach, V. Zwiller, S. N. Dorenbos, and I. Esmaeil Zadeh, "Detecting telecom single photons with 99.5−2.07+0.5% system detection efficiency and high time resolution," *APL Photonics*, vol. 6, mar 2021.

[121] K. Pyka, J. Keller, H. L. Partner, R. Nigmatullin, T. Burgermeister, D. M. Meier, K. Kuhlmann, A. Retzker, M. B. Plenio, W. H. Zurek, A. del Campo, and T. E. Mehlstäubler, "Topological defect formation and spontaneous symmetry breaking in ion Coulomb crystals," *Nature Communications*, vol. 4, aug 2013.

[122] S. Hannig, L. Pelzer, N. Scharnhorst, J. Kramer, M. Stepanova, Z. T. Xu, N. Spethmann, I. D. Leroux, T. E. Mehlstäubler, and P. O. Schmidt, "Towards a transportable aluminium ion quantum logic optical clock," *Review of Scientific Instruments*, vol. 90, May 2019.

[123] T. Nordmann, S. Wickenhagen, M. Doležal, and T. E. Mehlstäubler, "Bichromatic UV detection system for atomically-resolved imaging of ions," 2023.

[124] K. D. Nelson, X. Li, and D. S. Weiss, "Imaging single atoms in a three-dimensional array," *Nature Physics*, vol. 3, pp. 556–560, June 2007.

[125] Y. R. P. Sortais, H. Marion, C. Tuchendler, A. M. Lance, M. Lamare, P. Fournet, C. Armellin, R. Mercier, G. Messin, A. Browaeys, and P. Grangier, "Diffraction-limited optics for single-atom manipulation," *Physical Review A*, vol. 75, Jan. 2007.

[126] M. K. Tey, Z. Chen, S. A. Aljunid, B. Chng, F. Huber, G. Maslennikov, and C. Kurtsiefer, "Strong interaction between light and a single trapped atom without the need for a cavity," *Nature Physics*, vol. 4, pp. 924–927, Oct. 2008.

[127] A. L. Carter, J. O'Reilly, G. Toh, S. Saha, M. Shalaev, I. Goetting, and C. Monroe, "Ion trap with in-vacuum high numerical aperture imaging for a dual-species modular quantum computer," *Review of Scientific Instruments*, vol. 95, mar 2024.

[128] T. Dubielzig, S. Halama, H. Hahn, G. Zarantonello, M. Niemann, A. Bautista-Salvador, and C. Ospelkaus, "Ultra-low-vibration closed-cycle cryogenic surface-electrode ion trap apparatus," *Review of Scientific Instruments*, vol. 92, Apr. 2021.

[129] P. Huang and D. Leibfried, "Achromatic catadioptric microscope objective in deep ultraviolet with long working distance," No. 5524, Proc. Intl. Soc. of Photo-Optical Instrumentation, San Diego, CA, USA, 2003-10-15 00:10:00 2003.

[130] S. Thibault, "Cryogenic lens design case study: Gemini planet imager spectrograph," in *Current Developments in Lens Design and Optical Engineering XII; and Advances in Thin Film Coatings VII* (R. B. Johnson, V. N. Mahajan, and S. Thibault, eds.), vol. 8128, p. 812802, SPIE, Sept. 2011.

[131] N. Wallace, "Methods for thermally balanced mounting of refractive optical elements," master's thesis, University of Arizona, Tucson, Arizona, 2021.

[132] E. T. Kvamme, D. Trevias, R. Simonson, and L. Sokolsky, "A low stress cryogenic mount for space-borne lithium fluoride optics," in *Optomechanics 2005* (A. E. Hatheway, ed.), vol. 5877, p. 58770T, SPIE, Aug. 2005.

[133] J. L. Lizon and G. Huster, "Mounting of large lenses in infrared instruments," in *Optomechanical Technologies for Astronomy* (E. Atad-Ettedgui, J. Antebi, and D. Lemke, eds.), vol. 6273, p. 62733M, SPIE, June 2006.

[134] P. Selvaraj, "Lens mounting method to survive lunar cryogenic temperature," *CSA, December*, 2015.

[135] T. R. Froud, I. A. J. Tosh, R. L. Edeson, and G. B. Dalton, "Cryogenic mounts for large fused silica lenses," in *Optomechanical Technologies for Astronomy* (E. Atad-Ettedgui, J. Antebi, and D. Lemke, eds.), vol. 6273, p. 62732I, SPIE, June 2006.

[136] D. M. Stubbs, C. L. Hom, H. C. Holmes, J. C. Cannon-Morret, O. F. Lindstrom, J. W. Irwin, L. A. Ryder, T. T. Hix, J. A. Bonvallet, H.-K. S. Hu, I. V. Chapman, C. Lomax, E. T. Kvamme, G. S. Feller, and M. M. Haynes, "Adhesive bond cryogenic lens cell margin of safety test," in *Optomechanics 2011: Innovations and Solutions* (A. E. Hatheway, ed.), vol. 8125, p. 81250N, SPIE, Sept. 2011.

[137] C. Gal, A. Reutlinger, A. Boesz, T. Leberle, A. Mottaghibonab, P. Eckert, M. Dubowy, H. Gebler, F. Grupp, N. Geis, A. Bode, R. Katterloher, and R. Bender, "Test results of high-precision large cryogenic lens holders," in *Modern Technologies in Space- and Ground-based Telescopes and Instrumentation II* (R. Navarro, C. R. Cunningham, and E. Prieto, eds.), vol. 8450, p. 84500P, SPIE, Sept. 2012.

[138] A. Reutlinger, A. Mottaghibonab, C. Gal, A. Boesz, F. Grupp, N. Geis, A. Bode, R. Katterloher, and R. Bender, "Glue test results for high-precision large cryogenic lens holder," in *Modern Technologies in Space- and Ground-based Telescopes and Instrumentation II* (R. Navarro, C. R. Cunningham, and E. Prieto, eds.), vol. 8450, p. 845028, SPIE, Sept. 2012.

[139] P. R. Yoder, *Mounting Optics in Optical Instruments*. SPIE, Aug. 2008.

[140] D. Hanneke, J. P. Home, J. D. Jost, J. M. Amini, D. Leibfried, and D. J. Wineland, "Realization of a programmable two-qubit quantum processor," *Nature Physics*, vol. 6, pp. 13–16, nov 2009.

[141] H. Hahn, G. Zarantonello, M. Schulte, A. Bautista-Salvador, K. Hammerer, and C. Ospelkaus, "Integrated 9be+ multi-qubit gate device for the ion-trap quantum computer," *npj Quantum Information*, vol. 5, aug 2019.

[142] H. Ball, C. D. Marciniak, R. N. Wolf, A. T.-H. Hung, K. Pyka, and M. J. Biercuk, "Site-resolved imaging of beryllium ion crystals in a high-optical-access Penning trap with inbore optomechanics," *Review of Scientific Instruments*, vol. 90, p. 053103, may 2019.

[143] E. Born, Max; Wolf, *Principles of Optics*. Cambridge University Press, 1999.

[144] T. Tomaru, M. Tokunari, K. Kuroda, T. Uchiyama, A. Okutomi, M. Ohashi, H. Kirihara, N. Kimura, Y. Saito, N. Sato, T. Shintomi, T. Suzuki, T. Haruyama, S. Miyoki, K. Yamamoto, and A. Yamamoto, "Conduction effect of thermal radiation in a metal shield pipe in a cryostat for a cryogenic interferometric gravitational wave detector," *Japanese Journal of Applied Physics*, vol. 47, p. 1771, Mar. 2008.

[145] K.-H. Schuster, "Achromatisches linsensystem für ultraviolettstrahlen mit germaniumdioxid-glas," 1998.

[146] H. Gross, *Handbook of Optical Systems: Volume 1: Fundamentals of Technical Optics*. Wiley, Jan. 2005.

[147] R. A. Gonsalves, "Phase retrieval and diversity in adaptive optics," *Optical Engineering*, vol. 21, Oct. 1982.

[148] G. W. Forbes, "Robust and fast computation for the polynomials of optics," *Optics Express*, vol. 18, p. 13851, June 2010.

[149] R. Navarro, J. L. López, J. A. Díaz, and E. P. Sinusía, "Generalization of zernike polynomials for regular portions of circles and ellipses," *Optics Express*, vol. 22, p. 21263, Aug. 2014.

[150] L. M. Sanchez-Brea, A. Soria-Garcia, J. Andres-Porras, V. Pastor-Villarrubia, M. H. Elshorbagy, J. del Hoyo Muñoz, F. J. Torcal-Milla, and J. Alda, "Diffractio: an open-source library for diffraction and interference calculations," in *Optics and Photonics for Advanced Dimensional Metrology III* (P. J. de Groot, F. Guzman, and P. Picart, eds.), vol. 12997, p. 129971B, International Society for Optics and Photonics, SPIE, 2024.

[151] A. Clark, "Low temperature thermal expansion of some metallic alloys," *Cryogenics*, vol. 8, pp. 282–289, Oct. 1968.

[152] M. Okaji, N. Yamada, K. Nara, and H. Kato, "Laser interferometric dilatometer at low temperatures: application to fused silica srm 739," *Cryogenics*, vol. 35, pp. 887–891, Dec. 1995.

[153] D. N. Batchelder and R. O. Simmons, "Lattice constants and thermal expansivities of silicon and of calcium fluoride between 6° and 322°k," *The Journal of Chemical Physics*, vol. 41, pp. 2324–2329, Oct. 1964.

[154] C. L. Hopkins and J. H. Burge, "Application of geometric dimensioning and tolerancing for sharp corner and tangent contact lens seats," in *Optical System Alignment, Tolerancing, and Verification V* (J. Sasián and R. N. Youngworth, eds.), vol. 8131, p. 81310F, SPIE, Sept. 2011.

[155] J. Monroe, D. Gehring, I. Karaman, R. Arroyave, D. Brown, and B. Clausen, "Tailored thermal expansion alloys," *Acta Materialia*, vol. 102, pp. 333–341, Jan. 2016.

[156] J. A. Monroe, J. S. McAllister, D. Content, and J. Zgarba, "Negative thermal expansion allvar alloys for smaller optics," in *Optical Architectures for Displays and Sensing in Augmented, Virtual, and Mixed Reality (AR, VR, MR)* (B. C. Kress and C. Peroz, eds.), p. 37, SPIE, Feb. 2020.

[157] T. Barron, J. Collins, and G. White, "Thermal expansion of solids at low temperatures," *Advances in Physics*, vol. 29, pp. 609–730, Aug. 1980.

[158] T. H. K. Barron and G. K. White, *Heat Capacity and Thermal Expansion at Low Temperatures*. Springer US, 1999.

[159] G. K. White, "Thermal expansion of reference materials: copper, silica and silicon," *Journal of Physics D: Applied Physics*, vol. 6, pp. 2070–2078, Nov. 1973.

[160] D. Gibbons, "On the thermal expansion and grüneisen factor of vitreous silica," *Journal of Physics and Chemistry of Solids*, vol. 11, pp. 246–248, Oct. 1959.

[161] H. Wang, N. Yamada, and M. Okaji, "Precise dilatometric measurements of silica glasses.," *Netsu Bussei*, vol. 13, no. 1, pp. 17–22, 1999.

[162] P. Egan, "Shrinks when it's colder," NCSL International Workshop & Symposium, Grapevine, TX, US, 2022-08-01 04:08:00 2022.

[163] I. H. Malitson, "Interspecimen Comparison of the Refractive Index of Fused Silica*,†," *Journal of the Optical Society of America*, vol. 55, p. 1205, oct 1965.

[164] P.-E. Dupouy, M. Büchner, P. Paquier, G. Trénec, and J. Vigué, "Interferometric measurement of the temperature dependence of an index of refraction: application to fused silica," *Applied Optics*, vol. 49, p. 678, Jan. 2010.

[165] D. B. Leviton and B. J. Frey, "Cryogenic high-accuracy refraction measuring system (charms): a new facility for cryogenic infrared through far-ultraviolet refractive index measurements," in *Optical Fabrication, Metrology, and Material Advancements for Telescopes* (E. Atad-Ettedgui and P. Dierickx, eds.), vol. 5494, p. 492, SPIE, Sept. 2004.

[166] J. Matsuoka, N. Kitamura, S. Fujinaga, T. Kitaoka, and H. Yamashita, "Temperature dependence of refractive index of sio2 glass," *Journal of Non-Crystalline Solids*, vol. 135, pp. 86–89, Oct. 1991.

[167] Dubielzig, *Ultra-low vibration closed-cycle cryogenic surface-electrode ion trap apparatus*. PhD thesis, Gottfried Wilhelm Leibniz University of Hannover, 2021.

[168] S. Fujiyoshi, M. Fujiwara, C. Kim, M. Matsushita, A. M. van Oijen, and J. Schmidt, "Single-component reflecting objective for low-temperature spectroscopy in the entire visible region," *Applied Physics Letters*, vol. 91, July 2007.

[169] K. Schwarzschild, "Untersuchungen zur geometrischen optik ii," *Astronomische Mittheilungen der Koeniglichen Sternwarte zu Goettingen*, vol. 10, 1905.

[170] R. B. Hoover, D. L. Shealy, D. R. Gabardi, A. B. Walker, J. F. Lindblom, and T. W. B. Jr., "Design Of An Imaging Microscope For Soft X-Ray Applications," in *X-Ray Multilayers in Diffractometers, Monochromators, and Spectrometers* (F. E. Christensen, ed.), vol. 0984, pp. 234 – 246, International Society for Optics and Photonics, SPIE, 1988.

[171] S. D. Alaruri, "45.5x infinity corrected schwarzschild microscope objective lens design: Optical performance evaluation and tolerance analysis using zemax®," *International Journal of Measurement Technologies and Instrumentation Engineering*, vol. 7, pp. 17–37, Jan. 2018.

[172] A. Windberger, M. Schwarz, O. O. Versolato, T. Baumann, H. Bekker, L. Schmöger, A. K. Hansen, A. D. Gingell, L. Klosowski, S. Kristensen, P. O. Schmidt, J. Ullrich, M. Drewsen, and J. R. Crespo López-Urrutia, "Coulomb crystals in a cryogenic paul trap for sympathetic cooling of molecular ions and highly charged ions," in *AIP Conference Proceedings*, AIP, 2013.

[173] G. Lan and M. D. Twa, "Theory and design of schwarzschild scan objective for optical coherence tomography," *Optics Express*, vol. 27, p. 5048, Feb. 2019.

[174] R. Roberts, R. Tainsh, and G. White, "Thermal properties of zerodur at low temperatures," *Cryogenics*, vol. 22, pp. 566–568, Nov. 1982.

[175] J. L. Richter, "<title>new catadioptric telescope</title>," in *Los Alamos Conf on Optics '81* (D. H. Liebenberg, ed.), vol. 0288, pp. 33–37, SPIE, Dec. 1981.

[176] J. E. Webb, J. Bentley, P. F. Michaloski, A. R. Phillips, and T. Tienvieri, "Optical design forms for duv and vuv microlithographic processes," in *Optical Microlithography XIV* (C. J. Progler, ed.), SPIE, Sept. 2001.

[177] J. Webb and T. C. T., "Double mirror catadioptric objective lens system with three optical surface multifunction component," 2000.

[178] J. E. Webb and L. Denes, "Immersion lithography micro-objectives," in *Optical Microlithography XVII* (B. W. Smith, ed.), SPIE, May 2004.

[179] F. M. Leupold, *Bang-bang Control of a Trapped-Ion Oscillator*. PhD thesis, ETH Zurich, 2016.

[180] J.-M. Asfour, F. Weidner, C. Bodendorf, A. Bode, A. G. Poleshchuk, R. K. Nasyrov, F. Grupp, and R. Bender, "Diffractive optics for precision alignment of euclid space telescope optics (conference presentation)," in *Astronomical Optics: Design, Manufacture, and Test of Space and Ground Systems* (P. Hallibert, T. B. Hull, and D. W. Kim, eds.), p. 29, SPIE, Oct. 2017.

[181] M. Fujiwara, S. Fujiyoshi, and M. Matsushita, "Single-component reflecting objective for ultraviolet imaging and spectroscopy at cryogenic temperature," *Journal of the Optical Society of America B*, vol. 26, p. 1395, June 2009.

[182] C. R. Burch, "Reflecting microscopes," *Proceedings of the Physical Society*, vol. 59, pp. 41–46–2, Jan. 1947.

[183] M. Fujiwara, S. Fujiyoshi, and M. Matsushita, "Single-component reflecting objective for low-temperature imaging and spectroscopy of single nano objects," *Physics Procedia*, vol. 13, pp. 38–41, 2011.

[184] H. Inagawa, Y. Toratani, K. Motohashi, I. Nakamura, M. Matsushita, and S. Fujiyoshi, "Reflecting microscope system with a 0.99 numerical aperture designed for three-dimensional fluorescence imaging of individual molecules at cryogenic temperatures," *Scientific Reports*, vol. 5, Aug. 2015.

[185] K. ONA, N. SAKAGUCHI, H. OHNO, and S. UTSUNOMIYA, "The advanced super invar alloys with zero thermal expansion for space telescopes," *TRANSACTIONS OF THE JAPAN SOCIETY FOR AERONAUTICAL AND SPACE SCIENCES, AEROSPACE TECHNOLOGY JAPAN*, vol. 18, no. 3, pp. 32–37, 2020.

[186] T. Harty, D. Allcock, C. Ballance, L. Guidoni, H. Janacek, N. Linke, D. Stacey, and D. Lucas, "High-fidelity preparation, gates, memory, and readout of a trapped-ion quantum bit," *Physical Review Letters*, vol. 113, Nov. 2014.

[187] P. Wang, C.-Y. Luan, M. Qiao, M. Um, J. Zhang, Y. Wang, X. Yuan, M. Gu, J. Zhang, and K. Kim, "Single ion qubit with estimated coherence time exceeding one hour," *Nature Communications*, vol. 12, Jan. 2021.

[188] R. E. Parks, "Autostigmatic microscope and how it works," *Applied Optics*, vol. 54, p. 1436, Feb. 2015.

[189] A. Courteville, R. Wilhelm, and F. Garcia, "A novel low-coherence fibre optic interferometer for position and thickness measurements with unattained accuracy," in *Speckle06: Speckles, From Grains to Flowers* (P. Slangen and C. Cerruti, eds.), vol. 6341, p. 63411Q, SPIE, Sept. 2006.

[190] A. C. Bailey and B. Yates, "The low-temperature thermal expansion and vibrational properties of alkaline earth fluorides," *Proceedings of the Physical Society*, vol. 91, pp. 390–398, June 1967.

[191] J. S. Browder and S. S. Ballard, "Thermal expansion measurements on four optical materials from room temperature to 10 k," *Applied Optics*, vol. 11, p. 841, Apr. 1972.

[192] Y. S. Touloukian, R. K. Kirby, E. R. Taylor, and T. Y. R. Lee, "Thermophysical properties of matter - the tprc data series. volume 13. thermal expansion - nonmetallic solids," Jan. 1977.

LIST OF FIGURES

LIST OF TABLES

ACKNOWLEDGEMENTS

This is the end and I feel exhausted. An excellent time for a recap of the last eight years I spent at the Max-Planck-Institute for Nuclear Physics in the highly charged ion group of Prof. José Ramon Crespo López-Urrutia my doctoral supervisor, mein Doktorvater.

Du hast mich Ende 2016 als Bachelorstudent in Deine Arbeitsgruppe aufgenommen und warst von Beginn an immer zur Stelle, wenn Hilfe nötig war. Dort, wo es Dir möglich war hast Du mich gefördert, immer wieder gefordert und damit geprägt. Dafür bin ich Dir sehr dankbar. Möge der XUV-Kamm bald hochgeladene Ionen in Deinen Paul-Fallen anregen.

Ein großer Dank geht an Wolfgang Quint seine Bereitschaft das Zweitgutachten anzufertigen.

Liebe EBIT-Gruppe, es war mir eine Freude mit Euch zu arbeiten, von Euch zu lernen, mich mit Euch auszutauschen. Während der gesamten Zeit hat sich die Gruppe immer wieder gewandelt und trotzdem blieb im Kern das soziale Miteinander und die gegenseitige Unterstützung in den Laboren.

Insbesondere möchte ich mich bei Dir, Elwin bedanken, unvergessen bleibt die HCI in einem abgeschotteten und doch so offenen Japan und der direkt darauf folgende PTB retreat. Aber auch sonst warst Du immer da, wenn es um das Experiment ging, sei es im Gespräch, beim Schrauben oder Kampf mit dem Code oder Korrekturlesen dieser Arbeit.

Weiterhin eine große Anerkennung geht an das Team des XUV-Frequenzkamms um Jan, Tobi und Lennart. Euer Potentialminimum und drang nach Ordnung und Praktikabilität hat mir nicht zuletzt beim Zusammenbau des Linsenobjektivs wieder eine Nacht mit Schlaf beschert.
Dear Yang, Dear Lakshmi, the office is now fully converted to DESY. I'm certain we will manage the challenges waiting for us in the future. Five stars to you.

Kein Experiment kommt heute mehr ohne eine (technische) Infrastruktur aus, welcher Ich hier in ihrer Gesamtheit Anerkennung zolle. Hier steht Euer Name!

Durch die ausgezeichnete Arbeit in der Konstruktion und das immense Knowhow der Mitarbeitenden in der Feinwerkmechanik Werkstatt konnten sowohl der VAUQSI

Aufbau, als auch das hier präsentierte Linsensystem realisiert werden. Insbesondere möchte ich mich bei Bettina Mörk für Ihre große Geduld und Ihre Art, die Welt der Wissenschaft in die Welt der Konstruktion zu transferieren, bedanken. Weiterhin möchte ich insbesondere Marcel Chardon und Willi Lasarenko hervorheben, welche die Linsenzellen gefertigt und erodiert haben, und mir dabei tiefes Wissen um Ihre Maschinen vermittelt haben. Nicht zu vergessen ist auch Rainer Heldner für seine große Hilfe beim aktiven Um-modellieren einiger Bauteile und das anfertigen diverser Experiment Porträtfotos.

Um überhaupt ein Modell zu erstellen brauchte es diverse Spezialsoftware, vielen Dank an dieser Stelle an Steffi, Dominik und Sven für das schnelle Einrichten diverser Lizenzserver und an die gesamte IT für Ihre zuverlässige, einfache Art mit Problemen und Computern umzugehen.
Egal ob eine Hebevorrichtung für Wartungszwecke oder ein Gestell für eine mini-EBIT oder einfach mal "nur" eine Platte gefertigt werden musste, die Werkstatt um Christian Kaiser war immer ein treuer Begleiter im Labor. Vielen Dank dafür!

Liebe Christina, Lieber Nikolas, Liebe Drittmittelabteilung und Lieber Einkauf, Ihr habt es möglich gemacht, dass wir innerhalb weniger Monate ein Millionenvolumen aufgeteilt auf 55 Positionen bei uns am Institut stehen hatten. Danke!

Vielen Dank an Piet Schmidt und seine Arbeitsgruppen an der PTB in Braunschweig für die Unterstützung am CryPtEx-SC Experiment. Ich bin mir sicher, dass Ihr mit Eurer EBIT zufrieden sein werdet. Dear Nadir, I hope you are feeling better now and that you will continue to achieve your goals in the near future.

Hier und da gab es immer wieder ein paar "Geister" die für mich ein offenes Ohr hatten und mir oft nur durch das zuhören und aufmuntern, manchmal auch durch Ihr Handeln sehr geholfen haben. Ich hoffe, ich kann das irgendwann einmal zurückgeben.

Paul, in case you read this, while we could not spend that much time during my PhD, I want you to know that I admire you in so many ways and I want to thank you for your guidance. I hope we will spend more time on the bike/in a Café/ in the future again.

Liebe Anne, Vielen Dank für Dein Verständnis an den vielen Tagen, an denen ich mich mit meiner Doktorarbeit beschäftigt habe oder einfach körperlich oder geistig zu erschöpft war um mit Dir Zeit am der frischen Luft zu verbringen.